RF Reactive Magnetron Sputter Deposition of Silicon Sub-Oxides

ISBN: 978-90-393-4433-0

RF Reactive Magnetron Sputter Deposition of Silicon Sub-Oxides

RF Reactief Magnetron Sputterdepositie van Silicium Sub-Oxides

(met een samenvatting in het Nederlands)

Proefschrift

ter verkrijging van de graad van doctor aan de Universiteit Utrecht op gezag van de rector magnificus, prof. dr. W.H. Gispen, ingevolge het besluit van het college voor promoties in het openbaar te verdedigen op woensdag 17 januari 2007 des middags om 2.30 uur

door

Eduard Dieter van Hattum

geboren op 10 september 1976 te Soest

Promotoren: Prof. Dr. F.H.P.M. Habraken
Prof. Dr. H. Rudolph
Co-promotor: Dr. W.M. Arnold Bik

Dit proefschrift werd mogelijk gemaakt met financiële steun van Océ Technologies B.V., Venlo.

Contents

1 Introduction

1.1 General introduction 11
1.2 Goal and outline of this thesis 13
1.3 References 14

2. Experimental

2.1 Introduction 15
2.2 The deposition setup 16
2.3 Gas characterisation 18
2.3.1 Total pressure measurement 18
2.3.2 Rest Gas Analysis 18
2.3.3 Gas pressure control 18
2.4 Plasma characterisation 19
2.4.1 Power management 19
2.4.2 Langmuir Probe 19
2.4.3 Energy resolved mass spectrometry 20
2.5 Sample characterisation 20
2.5.1 Rutherford Backscattering Spectrometry 21
2.5.1.1 RBS data analysis for layers on a c-Si substrate 21
2.5.1.2 RBS data analysis for layers on a glassy carbon substrate 23
2.5.2.1 Elastic Recoil Detection 24
2.5.2.2 Data Analysis in ERD 25
2.5.3 Fourier Transform Infrared Absorption Spectroscopy 26
2.6 References 26

3. The application of *in-situ real-time* ER*D*

3.1 Introduction 27
3.2 Influence of the plasma on the ion beam 28
3.3 Interpreting the ERD signals 28
3.4 Total-film *real-time* ERD 30
3.5 Surface selective *real-time* ERD 32
3.6 Comparison of surface selective ERD and total-film ERD 33
3.7 Influence of the ion beam on the argon content of the film 34
3.8 Influence of the ion beam on the x-value of the deposited film 35
3.9 Influence of the ion beam on the layer thickness 36
3.10 Constant O_2 flow versus constant O_2 partial pressure: an application of *real-time* ERD 37
3.11 Conclusions 40
3.12 References 40

4 Characterization of the argon plasma and deposited films

4.1 Introduction 41
4.2 Langmuir probe measurements 43
4.2.1 The Langmuir probe setup 43
4.2.2 Interpretation of the Langmuir probe results 43
4.2.3 Langmuir probe: interpretation of the characteristic curve 44
4.2.4 Langmuir probe: spatial mapping of electron temperature, ion density and plasma potential 46
4.2.5 Plasma properties in front of the race-track as a function of total pressure and absorbed power 49
4.3 Mass spectrometry 52
4.3.1 Mass spectrometer configuration 52
4.3.2 Mass spectrometry: Basic ion properties 53
4.3.3 Ion bombardment of the anode: Ion energy profile at low pressure plasmas 56
4.3.3.1 Estimation of the argon ion bombardment at the deposition surface 58
4.3.4 Silicon ion yield as function of total pressure 59
4.3.5 Sputtered clusters of silicon 60
4.4 Thin film deposition: Silicon deposition rate 61
4.4.1 Silicon deposition rate as a function of absorbed power 61
4.4.2 Silicon deposition rate as a function of pressure 62
4.5 Relative extent of argon ion bombardment as function of the applied power 64
4.6 Spinodal decomposition in deposited films 65
4.7 Summary 67
4.8 References 68

5 Oxygen incorporation during deposition

5.1 Introduction 71
5.2 Material growth rate 72
5.2.1 Growth rate of silicon 72
5.2.2 Growth rate of oxygen 73
5.3 Temperature dependence in the growth rate of oxygen 76
5.4 Mass spectrometer measurements 77
5.5 Ion yield dependence on the vertical position with respect to the cathode 80
5.6 The SiO contribution to the deposited material 82
5.7 The contribution of atomic oxygen to oxygen incorporation 84
5.8 Summary of the oxygen incorporation in the growing films 84
5.9 The cathode 85
5.10 Transition region in the cathode composition 87
5.11 Conclusions 88
5.12 References 89

6 Argon incorporation in the deposited films

6.1 Introduction 91
6.2.1 Argon incorporation into silicon films as a function of power 92
6.2.2 Argon incorporation as a function of the x-value 92
6.2.3 Argon incorporation as function of height of the cathode 93
6.2.4 An overview of the argon incorporation into the substrate 96
6.3 Discussion 96
6.4 Conclusion 98
6.5 References 98

Summary 99

Samenvatting 101

List of publications 105

Dankwoord 107

Curriculum vitae 109

1

Introduction

1.1 General introduction

Silicon (Si) is used as a basic material for the fabrication of micro-electronics. Both amorphous and crystalline silicon are of great importance to the electronics industry as well as the totally oxidized state of silicon, silicon-dioxide (SiO_2). Silicon-dioxide is used as an insulator to separate conductive elements while doped silicon is used in active regions in electronic devices, like in p-n junctions. The interface between silicon and silicon-dioxide has a mixed phase where not all the atoms are in the SiO_2 matrix or the Si matrix. The minimal thickness of such an interface layer is therefore 1 or 2 monolayers of material. The material in the interface can be described as SiO_x ($0 \leq x \leq 2$).

This thesis is mainly focused on the accurate deposition of ´bulk´ layers of SiO_x. These SiO_x layers are used as precursor material for silicon crystals embedded in a silicon-dioxide matrix, which is considered an important material for the silicon based opto-electronic device technology [1]. A further application concerns its use as a charge retention layer in the direct inductive printing concept developed by Océ Technologies [2]. In many of the applications the preparation of the material has to be carried out at a relatively low temperature, for instance, because in the stage of device processing where the material is deposited, there already is a manufactured structure present which does not allow a high deposition temperature. In case of the applications of SiO_x films, a straightforward method to deposit

these at a low temperature is by using a reactive radiofrequency magnetron sputter deposition process [3]. In this process one of the constituents of the growing material, silicon in the case of SiO_x, is produced in atomic form by sputtering from a (silicon) target as a result of bombardment by energetic inert gas ions produced in the plasma, and moves in the direction of and sticks with a certain probability on the growth surface. The other constituent, in our case oxygen, originates from a gaseous component, in this thesis O_2, and can be incorporated in the growing films through various mechanisms. Therefore, reactive sputter deposition can be considered as a mixed physical and chemical process. Further, the magnetron sputtering is achieved by the use of a magnetic field near the cathode which confines the electrons in that region thereby increasing the ion density and hence the sputter ion density.

Considering SiO_x to be a random continuous network, the silicon sub-oxide network consists of a tetrahedral structure with a central Si atom, back-bonded to 4 Si and/or O atoms. Ignoring dangling bonds in the material the average number of O atoms on the corners of one tetrahedron amounts to 2x and the average number of Si atoms amounts to 4-2x. The distribution and spatial variation in the O and Si co-ordination numbers on a nanoscale have been the subject of many reports [4]. Indeed, an interesting aspect of silicon sub-oxide SiO_x is its tendency to phase separate into silicon and silicon-dioxide through spinodal decomposition [5]. Such a process does not require formation of nuclei of one of the phases, which subsequently grow, but rather the process of phase separation proceeds through many small steps in which oxygen poor regions become more oxygen poor and simultaneously oxygen rich regions become more oxygen rich and a continuous distribution of intermediate stages is possible. It is assumed that the relevant properties of the material, like its conductivity, depends on its precise nanostructure, in view of the role of percolation in the charge transport, further ascribed to variable-range hopping [6].

It appears that this phase separation can, to some extent, be realised by many events of local activation on a nanometer scale, as in nanometer-scale high-energy ion tracks [7]. The possibility that phase separation occurs as a result of local activation, has led to the hypothesis that to some degree the phase separation also occurs during the low temperature growth of SiO_x under reactive conditions like sputter deposition. The energy, involved in the process of activation, can be locally supplied to the growth surface by chemical means, i.e., from the net heat of the reactions which lead to the incorporation of silicon and oxygen atoms, and/or by physical means from the inert gas ion bombardment from the plasma and from the heat delivered by the cathode by radiation or conduction through the gas.

In the study of the relevant mechanisms in sputter deposition one of the key issues is how processes on the sputter target, initiated by the inert gas sputter plasma, relate to the film growth. Or, stated differently, the issue is how the sputter cathode communicates with the deposition surface. Inherently, the sputter cathode is the source of sputtered Si particles with non-thermal energy, which impinge on the deposition surface and contribute to film growth. The sputter cathode also acts as a source of energy, since in the sputter process a large part of the energy carried by the sputtering ions is converted into heat. Energy is transferred from the cathode to the growth anode in the form of the kinetic energy carried by the sputtered particles, eventually via heating of the gas [8,9], or through heat conduction and, especially, thermal radiation [10].

In case of reactive sputter deposition, the reactive component in the sputter gas reacts with the growth surface, but also with the cathode surface. This influences the kinds and amounts of species sputtered and hence the kinds and amounts of species impinging and reacting on the growth surface. The reactive gas of course also reacts directly with the growth surface, possibly after excitation in the plasma. The consequence is that composition and structure of the grown are determined by the relative contributions of the various distinct processes. The contribution of the various species to the growth process depends on the material being deposited, the combination of reactive gas and target composition, and on the details of the deposition system.

Differences between the sputter cathode and the deposition surface are found in the processes taking place. Processes at the cathode are silicon sputtering and oxidation while at the deposition surface oxidation and silicon particle sticking are of importance. Both processes are obviously related, although the nature of the relationship is complicated and studied extensively [11].

1.2 Goal and outline of this thesis

In this thesis investigations of the reactive magnetron sputter deposition of silicon sub-oxide (SiO_x) films is described. Details of the film growth in relation to the species arriving at the deposition surface are studied as well as the chemical composition and the structure of the deposited films. We apply various state-of-the-art, plasma, surface and thin-film characterisation techniques, and some of them were especially adapted for the present study. The idea is that understanding and control of the processes in the deposition allows the understanding and control of the as-deposited-layer nanostructure.

The thesis is organised as follows. In chapter 2 a concise overview of the applied experimental techniques for deposition, film and plasma characterisation is given. Also the difficulties and solutions of how to determine partial pressures of relevant gases in the considered pressure region are considered.
Chapter 3 presents the development and details of the experimental techniques which were especially adapted for application in the plasma deposition system. This includes the application of the high-energy ion beam technique Elastic Recoil Detection for the *in-situ* and *real-time* measurement of deposited layer composition and thickness.
Chapter 4 reports spatially-resolved Langmuir probe measurements of ion density, electric potential and electron temperature in the sputtering plasma, where a distinction is made between the sputtering cathode fall region and the plasma afterglow, from which ions impinging on the growth surface originate. Since the vast majority of the impinging ions are Ar^+ ions, the emphasis is on the measurement and discussion of the dependence of the flux and energy distribution of these ions on the adjustable plasma parameters like gas pressure and radiofrequency input power, as determined with an energy-resolving mass spectrometer. The possible role of the ion bombardment and its variation with plasma parameters on the layer nanostructure has been experimentally addressed by application of transmission Fourier transform infrared absorption spectrometry measurements in the frequency region of the Si-O-Si asymmetric stretch vibration in the grown films and is discussed within the framework of a possible ion beam induced Si/SiO_2 phase separation.

Chapter 5 deals with the silicon growth and the oxygen incorporation on the growth surface and on the sputter target erosion area, and the relation between these two relevant surfaces. A model is presented explaining the large role of the deposition system geometry on the oxygen household during this reactive magnetron sputter deposition process. Chapter 6 presents and discusses measurements of argon incorporation in the grown layers. Finally, chapter 7 contains a summary and the conclusions.

1.3 References

[1] L. Pavesi, L. Dal Negro, C. Mazzoleni, G.Franzo and F. Priolo, Nature **408** (2000), 440.

[2] Patent US 4.704.621, held by Océ Technologies, Venlo.

[3] J.A. Thornton and J.E. Greene in: Rointan F. Bunshah, editor *Handbook of deposition technologies for films and coatings*, second edition, Noyes Publications 1994, ch 5.

[4] A. Hohl, T. Wieder, P.A. van Aken, T.E. Weirich, G. Denninger, M. Vidal, Oswald, C.Deneke, J. Mayer and H. Fuess, J. Non-Cryst. Solids **320** (2003), 255.

[5] J.J. van Hapert, A.M. Vredenberg, E.E. van Faassen, N. Tomozeiu, W.M. Arnoldbik and F.H.P.M. Habraken, Phys. Rev. B **69** (2004), 245202.

[6] J.J. van Hapert, Thesis University of Utrecht, 2002, "Hopping Conduction and Chemical Structure: a study on Silicon Suboxides"

[7] W.M. Arnoldbik, N. Tomozeiu, E.D. van Hattum, R.W. Lof, A.M. Vredenberg and F.H.P.M. Habraken, Phys. Rev. B **71** (2005), 125329.

[8] S.D. Ekpe and S.K. Dew, J. Phys. D: Appl. Phys. **39** (2006), 1413.

[9] A. Palmero, H. Rudolph and F.H.P.M. Habraken, Appl. Phys. Lett. **87** (2005), 071501.

[10] S.D. Ekpe and S.K. Dew, J. Vac. Sci.Technol. A **20** (2002), 1877.

[11] S. Berg, T. Nyberg, Thin Solid Films **476** (2005), 215.

2

Experimental

2.1 Introduction

In this chapter the experimental techniques of deposition and characterization are briefly described. The relevant parts of the deposition system are: the vacuum vessel, the gas-inlet and gas-monitoring system, the movable sputter target, the substrate-holder assembly, the RF power supply. Additionally the setup includes equipment for various analysis techniques: Elastic Recoil Detection (ERD), Langmuir Probe and energy resolved mass spectrometry. Ex-situ techniques applied are Rutherford Backscattering Spectrometry (RBS) and occasionally Fourier Transform Infrared Spectrometry (FTIR).

2.2 The deposition setup

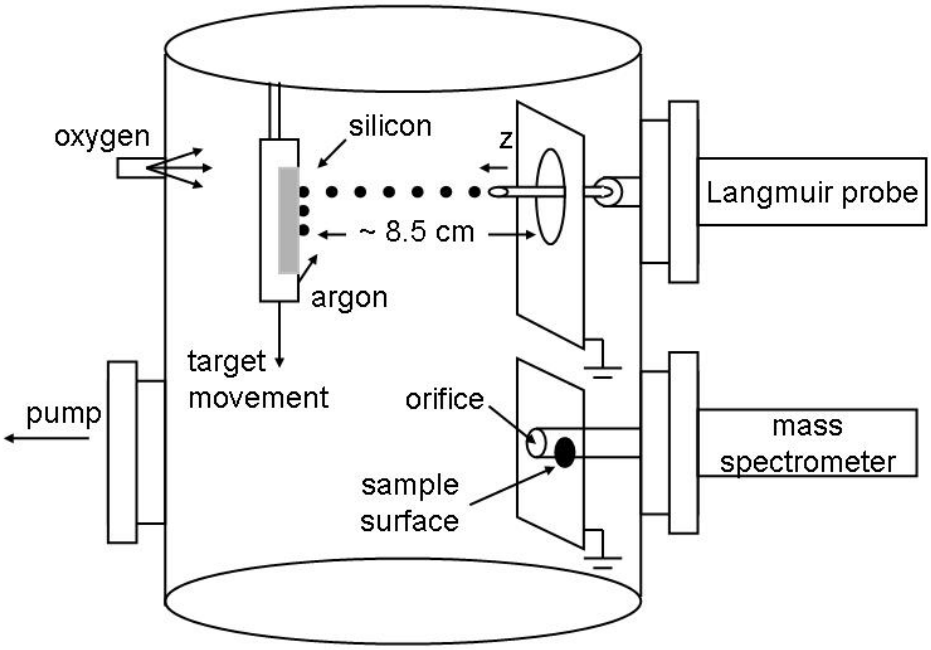

Figure 2.1 The deposition vessel with movable target and sample surface and the plasma characterization tools: the Langmuir probe and the mass spectrometer.

A schematic overview of the deposition system is given in Fig. 2.1. A UHV vacuum vessel with a volume of 100 dm^3 is evacuated by a turbo-pump with a pumping speed of 520 dm^3/s (effective pumping speed 180 dm^3/s), which results in a base pressure of 1 μPa. The cathode (target), see Fig. 2.2, with a circular symmetry, is covered by a poly-crystalline silicon target (purity 99.999 %) and surrounded by a grounded metal ring, which serves as the main anode. All other grounded surfaces in contact with the plasma act as an anode as well. However, a large part of the grounded surfaces is covered by sputtered material and is expected to be covered by insulating material after a number of SiO_2 depositions. The sample deposition surface is also grounded and placed at a distance of 8.5 cm parallel to the cathode. Behind the target is a single magnet surrounded by a ring of magnets of opposite polarity. The resulting magnetic field confines the electrons in the plasma near the target. The field strength at 1 cm in front of the target is estimated to be 0.05 T. The entire cathode can be moved up and down over a distance of 30 cm, enabling position dependent analyses and also mounting samples *in-situ*. Sample substrates have an area of 1 cm^2, and are made of crystalline silicon with a (100) surface, or Sigradur® G glassy carbon with a diamond polished surface. The substrates can be introduced into the deposition system via a load-lock system. For ex-situ measurements the sample can be transported in a mobile vacuum system towards other UHV systems like the XPS analysis chamber. Argon is showered parallel to the target surface via a series of gas inlet ports attached to the ground ring.

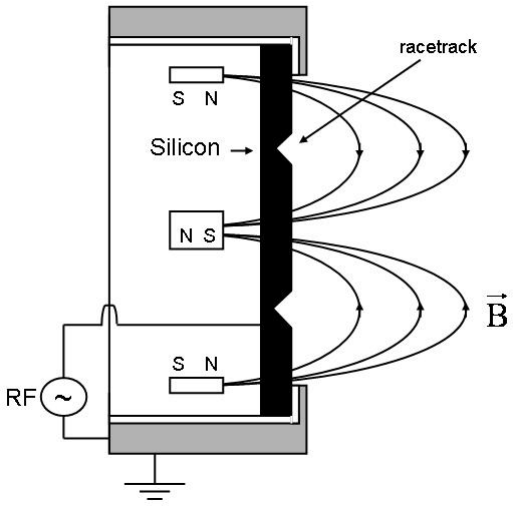

Figure 2.2 The sputter target in detail.

In Fig. 2.3 the deposition surface and mass spectrometer are projected on the cathode when the target is at standard height. Both the deposition surface and the mass spectrometer have the same distance to the centre of the cathode. The estimated size of the target sputter area ("racetrack") is indicated by the light grey shaded donut. The cathode can be moved in the vertical direction. The geometry as shown in Fig. 2.3 makes clear that the deposition and the mass spectrometer have equivalent positions with respect to the racetrack, independent of the vertical position of the cathode. The Langmuir probe shows a relative motion along the middle vertical dotted line upon movement of the target.

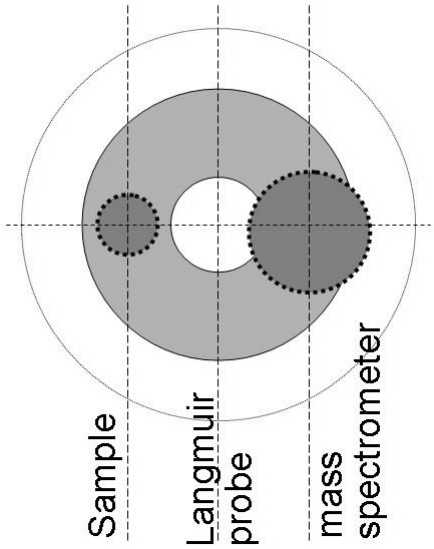

Figure 2.3 The deposition surface (small dark circle) and mass spectrometer (large dark circle) projected on the cathode, for normal position versus the cathode. The race-track is shaded light gray. By movements of the sputter cathode the indicated objects move along the indicated line relative to the cathode.

2.3 Gas characterisation

2.3.1 Total pressure measurement

The total gas pressure during deposition is measured using a MKS Baratron Type 627B capacitance manometer that measures 100 Pa full-scale. A foil pressing against an electrical sensor deflects under influence of the force exerted on it by the gas particles hitting it. Thus, it measures the force per unit of area, i.e., pressure. The advantage of this type of pressure gauge is that the pressure is directly measured independent of the type of gas. The resolution of this sensor is 0.01 Pa. This absolute pressure measurement is taken as a reference value when using other methods to gain information about the pressure.

2.3.2 Rest Gas Analysis

A Rest Gas Analyser (RGA) of the type MKS HPQ2S is mounted on the system. This RGA can measure the amount of particles in the gas with a mass of 80 a.m.u. or less. It consists of a total pressure gauge and a mass selective detector. Usually, several masses are selected and monitored in a multiplexed fashion. The RGA can be operated at normal deposition pressures without the need of a differentially pumped system. The mass selective detector has a finite size, which becomes important at higher total pressure, since ions are created in front of the mass filter, and at high pressures the particles in the background gas collide with the ions and prevent them from reaching the detector ballistically. This interference leads to a decrease in signal if the pressure increases. This so-called roll-over effect is compensated by a standard factory built-in calibration with the signal generated from the total pressure gauge. The raw signal without roll-over correction shows a dependence on oxygen partial pressure, thus a signal decrease from the mass selective detector. An increase in the oxygen partial pressure decreases the signal for all gases, including argon. Due to this effect it is necessary to introduce a second calibration to get an absolute value for the partial pressure for the gases present in the system. This second calibration is performed using the Baratron total pressure gauge as an absolute value for the pressure.

2.3.3 Gas pressure control

Gas pressure is maintained in a flow system using a MKS 647B multi channel flow controller. Gas flow through the valves is measured with as unit standard cubic centimetres per minute (sccm), which means that an amount of gas contained in one cubic centimetre at standard temperature and pressure flows through the controller in one minute. The argon flow can be set between 1.4 and 137 sccm. For oxygen, the flow to the system is zero or has a value between 0.1 and 10 sccm. The oxygen is introduced to the plasma via a gas inlet located far from the plasma. Using maximum flow a total pressure of about 1.5 Pa can be obtained using the normal pumping configuration. An additional increase in pressure can be obtained by reducing the pumping speed with which the system is evacuated. Partially closing of the valve between pump and deposition vessel reduces the effective pumping speed from 180 dm^3/s to 22 dm^3/s and increases the maximum pressure to about 4.0 Pa.

2.4 Plasma characterisation

2.4.1 Power management

Power is supplied to the system using a RFPP-RF5S power supply. Every power transmitter and receiver has a characteristic impedance. The impedance of the plasma alters with changes of settings of the plasma, and can even change with time. Optimal power transfer takes place if the impedance of transmitter and receiver are equal. For this purpose an Advanced Energy AM-5 matching circuit is attached to the transmitter. The matching circuit consists of a series of resistors and variable capacitors and equalizes the impedance of the transmitter and the plasma. Unfortunately this matching circuit reflects part of the power intended for the plasma in a slightly irreproducible manner, which at the end could result in an irreproducible composition of the deposited layers. To avoid this we have introduced an additional feedback loop; see Fig. 2.4, to make sure that the power absorbed by the plasma system, which is the intended power minus reflected power, is constant during the deposition. Since the amount of reflected power is not necessarily constant during the deposition the compensation routine is activated periodically (every 10 sec). The time average of the cathode potential is also measured by the power source.

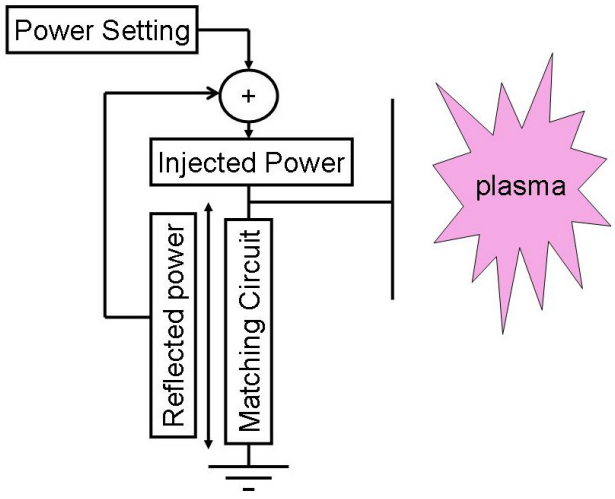

Figure 2.4 The applied power compensation circuitry schematically represented.

2.4.2 Langmuir Probe

A Hiden Espion Advanced Langmuir probe [1] is mounted in the top of the vessel, see Fig. 2.1. Perpendicular to the cathode a conductive tip can be moved to a certain distance from the cathode. The length of the tip is 10 mm and its diameter is 0.15 mm. Without connecting the tip to any electrical contact it gets charged to the local potential in the plasma surrounding the tip. Variation of the potential on the tip makes the tip either attract or repel electrons and ions. Thus by measuring the current while keeping the tip at a fixed potential we gain information about the local electrical properties of the plasma. Note that the signal averaging takes place over the length of the tip. Further details concerning the analysis using the Langmuir probe are presented in Chapter 4 of this thesis.

Usually, a tip is made of tungsten which is sufficient for most plasma's. However, it is known that tungsten is readily oxidized even if there is only a small amount of oxygen available. Therefore, the tip is replaced by a platinum tip in the cases when oxygen is introduced into the plasma. A highly unwanted effect is that material is deposited on the probe tip. This deposited material is removed by sputter cleaning, by deliberately putting a negative potential of -10 V on the tip for 95 ms and alternating this with 5 ms of actual current collection at a set voltage.

2.4.3 Energy resolved mass spectrometry

An energy resolved mass spectrometer, Hiden EQP-1000, has been mounted in the substrate holder (see Fig. 2.1). This mass spectrometer is differentially pumped and has a base pressure below $2 \cdot 10^{-7}$ Pa. A small aperture of 300 μm in the anode allows particles travelling from the plasma to the mass spectrometer. The pressure in the mass spectrometer during deposition is therefore limited to $5 \cdot 10^{-4}$ Pa, thus three orders in magnitude lower than the pressure in the deposition vessel. Charged particle collection from the plasma can be enhanced by applying an extraction voltage closely behind the orifice. This feature has hardly been used in the work described in this thesis.
The ions are guided through the mass spectrometer using electromagnetic lenses. Ions with a given kinetic energy are selected using an electrostatic energy filter and subsequently the ions are guided through a quadrupole mass filter. All ions that passed both filters are accelerated towards a channeltron. The ions collected from the plasma always carry a significant amount of energy, gained in the anode sheath. Therefore, without extraction voltage, the charged particle velocity is considered to be perpendicular to the anode surface. In this case, all ions move into the mass spectrometer perpendicular to the surface parallel to the central path of the mass spectrometer and thus every species has the same transmission function. All the ions from the plasma are expected to have similar energy and the transmission function is therefore expected to be mass independent.

Direct measurement of neutral particles coming from the plasma is not possible. However, it is possible to ionise these neutral particles in the mass spectrometer. For this purpose an ionisation cage is added behind the ion extractor. It is possible to safely tune the current in the ionisation cage between 50 and 2000 μA, with the electrons having an energy between 20 and 150 eV. Neutrals ionised in this cage have a different energy than the ions from the plasma. Thus it is easy to distinguish between these two particle contributions. Neutral particles arriving at the mass spectrometer aperture have not been accelerated over the sheath and therefore have a non-parallel velocity with respect to the mass spectrometer central ion path. The transmission-function of the mass-spectrometer, as well as the acceptance angle for neutrals are therefore different for different species. In combination with the difference in ionisation energy for different species we have to note that relative amounts of initially neutral species measured with the mass spectrometer mostly deviate from the actual relative amounts of those species present in the plasma.

2.5 Sample characterisation

The ion beam techniques RBS and ERD are applied to characterize the deposited layers in terms of thickness and composition (as a function of depth). However, as shown in the

literature, irradiation with MeV heavy-ion beams as used in ERD can alter the microscopic properties of SiO_x layers due to the strong tendency of SiOx to separate in silicon and silicon dioxide phases through the process of spinodal decomposition [2]. As a result of energy transfer to the thin film it relaxes by phase separation in oxygen-rich and oxygen-poor regions of the film. The overall bonding configuration is studied by means of Fourier Transform Infra-Red measurements (FTIR).

2.5.1 Rutherford Backscattering Spectrometry

RBS [3] is used as a post-deposition ex-situ technique. In RBS a beam of light ions, usually He^+, with an energy of 0.5-3 MeV is directed onto a sample. Travelling through the material the kinetic energy of the ions gradually decreases. Some of the He ions are scattered in a binary nuclear collision with the atoms in the layer at a certain depth. A silicon surface barrier (SSB) detector is used to determine the number of particles scattered under a given angle. The energy carried by these scattered particles just before entering the detector is representative for the mass of the particles they collided with and the depth at which the collision took place. Particles hitting a heavy atom transfer less energy in the collision than those that collide on a light atom at the same scattering angle. It is crucial to note that in RBS the outgoing particles are of the same species, in our case He, as the incoming ions. The concentrations of silicon, oxygen and argon are obtained with this method. The RBS measurements in this thesis have been made using a 2 MeV He^+ beam, provided by a 3 MeV single ended Van de Graaff accelerator. Usually, samples are deposited on a silicon (100) single crystal. Determination whether particles have been backscattered from silicon nuclei in the film or in the substrate is difficult for the interfacial region. Furthermore, the oxygen signal is superimposed on the Si-substrate signal, which makes an accurate determination of the oxygen concentration difficult, especially when this concentration is low. A solution to these problems is the use of a substrate that consists of atoms lighter than those in the top layer, for instance glassy carbon. All species in the deposited films, silicon, oxygen and argon have a higher mass than carbon and are nicely separated. Provided that the films are not thicker than about 0.5 μm, it is possible to produce a data fit (see section 2.4.1.2**)** without overlap between the O, Si and Ar spectral features.

2.5.1.1 RBS data analysis for layers on a c-Si substrate

Following reference 3 we find that the number of detected scattered particles of a given species in a thin film is given by

$$Y_s = \sigma(\theta)\ \Omega\ Q\ N_s \qquad (2.1)$$

Where the yield of particles of species s, Y_s, is obtained for a given scattering angle and primary energy dependent scattering cross-section $\sigma(\theta,E)$, the detector solid angle Ω, the total number of incident particles in the beam Q, and the number of atoms per unit of area (areal density) of species s in the film N_s. A particle travelling through a material will lose some of its energy. Thus the detected particles which have the highest energy are backscattered at the surface. Particles, scattered by the same species and detected with less energy, have been backscattered from an atom in a deeper lying layer.

The contribution of a crystalline substrate to an RBS spectrum is suppressed when we align the major crystalline directions parallel to the ion beam direction. In this situation, only the few topmost atoms of the crystalline structure are visible for the ions in the beam; the deeper laying atoms are in a shadow cone. A collision on the deeper atoms can only occur when they have left the shadow cone for instance because of their thermal vibrations or because the beam ions deviated from their original path due to interactions with the (amorphous) top layer. This effect of steering an ion beam in a crystal is called "channelling" [3].
In Fig. 2.5 a channelled RBS spectrum of a SiO_x film deposited on a piece of single crystalline Si-wafer is depicted. The oxygen, silicon and argon surface positions are indicated. Once the ion beam is accurately directed in the crystalline direction we can due to this effect easily distinguish the silicon in the deposited amorphous material from the silicon present in the crystalline wafer. The oxygen signal from the layer is superimposed on the suppressed silicon-substrate signal while the argon is almost separated from the silicon signal. The x-value can be determined from Fig. 2.5 using the following method, assuming that the x-value is constant over the thickness.

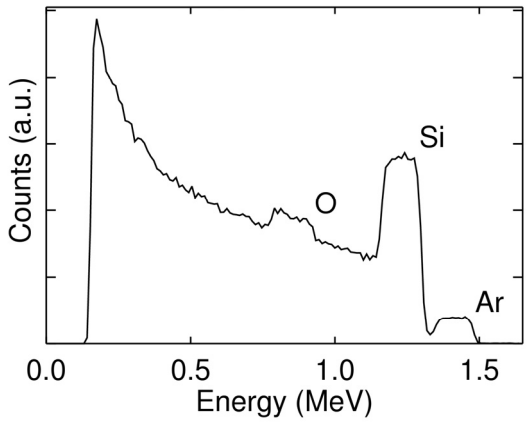

Figure 2.5 A typical channelled RBS spectrum of a SiO_x film deposited on silicon, Si, Ar and O surfaces are indicated

- Background subtraction of the Si signal around the oxygen to obtain the integrated detected counts from oxygen
- Background subtraction for silicon (if necessary) to obtain the integrated detected counts from silicon
- Division of Eq. 2.1 for oxygen through Eq. 2.1 for silicon gives the x-value.

$$x = \frac{N_O}{N_{Si}} = \frac{\sigma_{Si}(\theta)}{\sigma_O(\theta)} \frac{Y_O}{Y_{Si}} \qquad (2.2)$$

Eq. 2.2 is the resulting equation for determining the x-value for a given film. Geometrical film thickness can not be measured directly, but it can be estimated by comparison of the measured areal density of the atoms with the atomic (volume) density of the material.

The x-value can also be determined by comparing the ratio of the heights h_O and h_{Si} of the oxygen and silicon spectral features to the relative height for a sample with a known x-value, i.e., a thermally oxidized silicon wafer. From evaluation of the energy loss factors [3] for He ions that are scattered from O and those that are scattered from Si, it follows that the following expression gives a deviation from the actual value varying from 0 to only 4 % when x varies from 2 to 0. This is small compared to the statistical error, which is increasingly large at the lower x-values.

$$x = 2\frac{\left(h_O / h_{Si}\right)_{Sample}}{\left(h_O / h_{Si}\right)_{Ref}} \qquad (2.3)$$

Eq. 2.3 gives the x-value determination in case we make use of a SiO_2 reference sample. This method also has the advantage that the areal density of a film can be measured. From the energy width attributed to a certain species in an RBS spectrum from a sample compared to that of the same species from a reference sample of known thickness, we can determine the thickness of the SiO_x film on the examined sample. This is because the stopping power of amorphous Si and amorphous SiO_2 are about equal [4], although the atomic density in a-Si is $5 \cdot 10^{22}$ at./cm^3 while for a-SiO_2 we have $6.8 \cdot 10^{22}$ at./cm^3 [5].

2.5.1.2 RBS data analysis for layers on a glassy carbon substrate

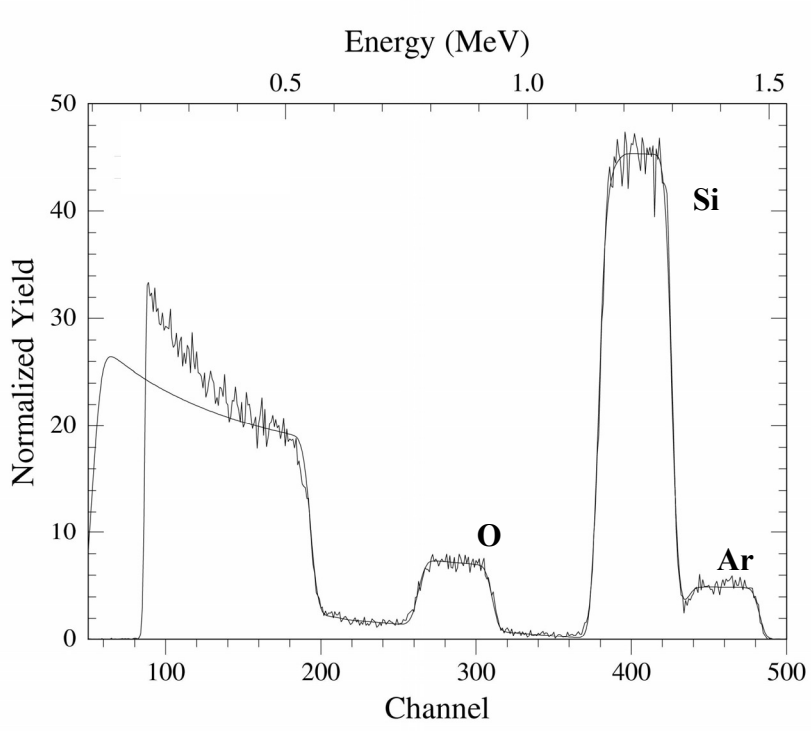

Figure 2.6 A measurement of an SiO_2 layer on a carbon substrate as well as the fitted simulated rump spectrum.

The so-called RUMP [6] analysis of the RBS spectra is done using a spectrum simulation and fitting routine to minimize the error between a simulated thin film structure and actual measurements. Fitting parameters are film areal density in at/cm^2, and the film composition The background under the oxygen peak in Fig. 2.6, which can have different causes, can easily be accounted for by introducing a heavier element with a linear profile, in the substrate. In Fig. 2.6 the measured spectrum of a thin SiO_2 film deposited on carbon is depicted as well as the simulated and fitted spectrum. Also argon is found in this deposited film, the silicon, oxygen and argon peak are indicated.

2.5.2.1 Elastic Recoil Detection

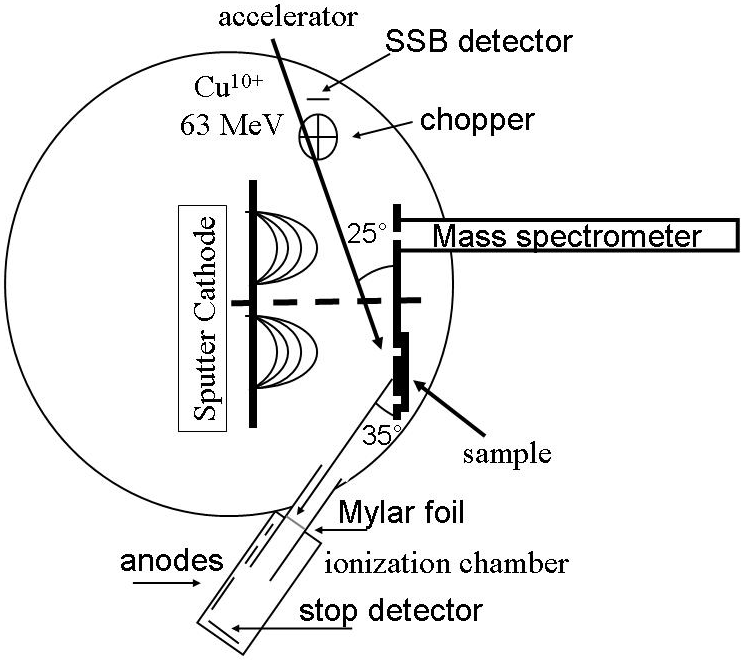

Figure 2.7 Horizontal cross section of the deposition vessel at the level of the ERD beam line.

In ERD [7] a beam of, usually heavy, ions impinges on the sample surface at a glancing angle. Some incoming ions knock out a single atom from the material in a binary interaction between the incoming ion and the atom involved. The ejected atoms are detected using differential energy measurement in an ionisation chamber. A 2 μm thin Mylar foil ($C_{10}H_8O_4$) separates the vacuum vessel from the ionisation chamber in which an easily ionisable gas, isobutane, is present at a typical pressure of 3000 Pa.
Particles to be detected first have to traverse the foil and with the remainder of their energy they cause ionisations in the chamber. Electrons produced in this way are collected on a series of 3 anodes. At a given kinetic energy the heaviest particles are the slowest and deposit the largest amount of energy in the first part of the ionisation chamber. Lighter atoms travel further into the chamber and have more energy left to deposit in the back part of the chamber. Under the most relevant experimental conditions only hydrogen is able to reach the stop-detector. This is an SSB detector similar to the one used in RBS. The amount of charge collected on each of the detectors is a measure for the energy that the recoiled particle has

lost in this particular section of the detector. A two-dimensional energy spectrum (dE-E) can be plotted in which the energy lost above the first or second anode is depicted versus the residual energy. These spectra contain signals which can unambiguously be attributed to a specific element or isotope. A 6 MV tandem van de Graaff accelerator is used to accelerate the desired ions. Typically, in our analyses 63 MeV Cu^{10+} ions impinge on the sample under an angle of 25° with respect to the sample surface while the recoil angle amounts to 35° with respect to the beam direction, see Fig. 2.7. A beam chopper in combination with an RBS detector is used to monitor the amount of incoming ions as a function of time by counting the Cu particles that are backscattered from the tantalum wings of the chopper.

2.5.2.2 Data Analysis in ERD

The energy of the recoiled particles is measured using an ionization chamber with an anode which is split in three parts. In Fig. 2.8 a two-dimensional spectrum of a SiO_x film on a glassy carbon substrate is depicted. The vertical axis depicts the energy released in the first part of the ionization chamber, ΔE_1, while the horizontal axis depicts the energy lost in the remainder of the chamber, ΔE_2+E_r. The features for silicon, oxygen and carbon are indicated. The signal above the carbon feature reveals that the substrate contains a small amount of nitrogen. In the lower panel, the intensities of the O and Si signal are depicted as a function of ΔE_2+E_r. It is clear that there is no need for background subtraction.

The particles from the ion beam carry a significant amount of energy and can alter the properties of the film, see chapter 3 of this thesis. Therefore it is crucial that, if one wants to obtain information concerning the film by other, non-destructive techniques such as FTIR, this technique is applied before the sample is exposed to the high-energy ion beam.

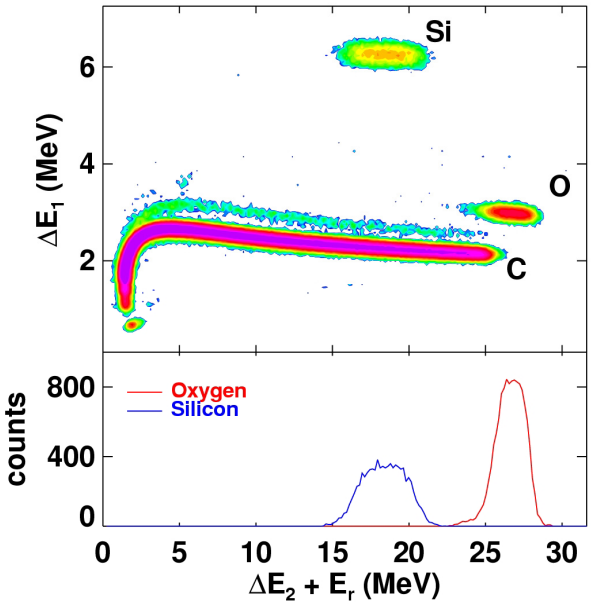

Figure 2.8 ERD spectrum of an SiO_x film deposited on carbon The amount of detected particles of O and Si are depicted as function of ΔE_2+E_r.

2.5.3 Fourier Transform Infrared Absorption Spectroscopy

Fourier Transform Infrared Absorption Spectroscopy **(**FTIR) is used ex-situ to determine the frequency of the Si-O-Si stretching vibration. The infrared absorption spectra of SiO_2 and SiO_x are extensively described and utilized in the literature [8, 9]. Infrared measurements are performed to determine the chemical backbonding structure of an Si-O-Si bridge, and are therefore sensitive for the nano-bonding structure of the material. A Si/SiO_2 phase-separated film therefore shows a different absorption wavelength compared to a not phase-separated film with the same x-value [2].

We use a Bruker Vertex 70 infrared spectrometer, to determine the infrared light transmitted perpendicularly through a thin film. A deuterated triglycine sulphate (DTGS) detector is used to detect the transmitted light between 370 and 7500 cm^{-1}. The resolution used is 4 cm^{-1}. The IR beam is split into two arms of an interferometer, one with a fixed mirror and one with a moveable mirror. This movement is measured using a HeNe laser (λ = 632,8 nm or ω = 15802,8 cm^{-1}). Since the wavelength of the HeNe laser is much smaller than the wavelength of the IR light, the position of the moveable mirror is very precisely known. The modulated light is transmitted perpendicularly through a silicon wafer. Comparison with the light transmitted through a reference sample yields the amount of light absorbed by the thin film. The modulated intensity of the total light collected by the DTGS detector is Fourier Transformed into a wavelength dependent signal.

2.6 References

[1] M. Bagatin, D. Desideri, E. Martines, G. Manduchi, G. Seriani and V. Antoni, Rev. Sci. Instrum. **68** (1997), 365.

[2] W.M. Arnoldbik, N. Tomozeiu, E.D. van Hattum, R.W. Lof, A.M. Vredenberg and F.H.P.M. Habraken, Phys. Rev. B **72** (2004), 125329.

[3] L.C. Feldman and J.W. Mayer, in *Fundamentals of Surface and Thin Film Analysis*, (PTR Pentice-Hall, Inc Upper Saddle River, NJ, USA, 1986) pp 51-52.

[4] J.F. Ziegler, J.P. Biersack and W. Littmark, *The Stopping and Range of ions in matter*, Pergamon, Oxford (1985)

[5] S. Sze, in *Physics of Semiconductor Devices*, 2nd ed. (John Wiley & Sons, New York, USA, 1981), pp.850,852.

[6] L.R. Doolittle Nucl. Instr. and Meth. **B9** (1985) 344.

[7] W.M. Arnold Bik and F.H.P.M. Habraken, Rep. Prog. Phys. **56** (1993) 859.

[8] C.T. Kirk, Phys. Rev. B **38** (1988), 1255.

[9] P.G. Pai, S.S. Chao, Y. Takagi and G. Lucovsky, J. Vac. Sci. Technol. A **4** (1986), 689.

3

The application of *in-situ real-time* ERD

3.1 Introduction

The subject of the research, described in this thesis, is the deposition of films of SiO_x. Usually the deposition and characterization of thin films are performed in different vacuum systems. In that case, the transport between the systems takes place through air and alterations to the film can occur, such as additional oxidation of the surface of our films, passivation of the surface and water absorption by possibly present pores in the film. To circumvent these effects we connected the deposition vessel to a beam line from a tandem van de Graaff accelerator so that the composition and thickness of the films can be determined by the high-energy ion beam technique Elastic Recoil Detection (ERD) immediately after deposition without breaking the vacuum. However, the appealing opportunity presents itself to attempt deposition and characterization at the same instant. Hereto, the beam line is differentially pumped over two flow resistors, so that the vacuum in the beam line is maintained when Ar and O_2 are led in the deposition vessel.
This chapter deals with the methods available to achieve such operation of *real-time* ERD and with the influences that deposition and characterization have on each other. As an example of the application of *real-time* ERD this chapter shows that the oxygen input flow is not the relevant physical quantity to describe the SiO_x deposition process, but rather that the oxygen partial pressure is the key parameter.

3.2 Influence of the plasma on the ion beam

The plasma is a charged gas and as such can interact with the particle beam used for ERD. However, the order of magnitude of the electrical potential is such that the electrical influence from the plasma on MeV ions is negligible. More important is the gas present in the deposition system. Simply stated; if an ion from the ERD beam has a large angle scattering event with a nucleus of a gas atom, it is lost or can even cause unwanted background in the spectrum. We will now estimate the fraction of the particle current which is removed from the ion beam by scattering at gas phase atoms, for the typical beam used in our work consisting of 50-63 MeV Cu ions. We define that a particle is lost when it has a collision that disturbs the path of the ion so much that it misses our sample. The pressure in the deposition vessel during deposition is in the order of 1 Pa. The distance that the ions travel through the plasma is about 50 cm. By assuming that all argon is confined to a thin layer at 50 cm distance from the sample, taking a permitted scattering angle of 3 mrad and using simple central force Coulomb scattering, we calculated an upper limit of the fraction of the particle current that miss our target due to collisions with Ar atoms to be well below 1%. The possible increase in background and loss of resolution as a result of scattering of primary or secondary ions with gas particles does not appear to be a problem. Finally, the energy loss that the ERD ions undergo in the plasma is about 50 keV. This does not affect the ERD results.

3.3 Interpreting the ERD signals

If we monitor the composition and thickness of the SiO_x film during its deposition by *real-time* ERD, the ion beam is put on the sample and the data acquisition is started before onset of deposition. An example of the $\Delta E/E$ ERD spectra, accumulated by the ionization chamber after the entire deposition process, is depicted in Fig. 3.1. Indicated are the elements that correspond to the individual features. In Fig. 3.1a the measured intensities are plotted versus ΔE_1 and ΔE_2+E_r. Here ΔE_1 is the energy loss that the recoiled particle experiences while traversing the first part of the anode of the ionization chamber. The sum of ΔE_2+E_r is the energy that is left after traversing the first anode. Fig. 3.1b is the equivalent for the second anode. Here ΔE_1 is not used. Since the first anode is a lot shorter than the second one (2, resp. 8 cm), it collects a smaller charge pulse and the signal to noise ratio is worse. This is reflected by the fact that O and C (let alone N) are hardly separable in Fig. 3.1a and easily separable in Fig. 3.1b. The advantage of a short anode is that a lower energy of the recoiled particle is allowed for fruitful detection, and therefore the probing depth is much larger. This is especially important for Si, which experiences a large stopping power in the ionizing gas. The layer is in the present example so thick that the Si recoils originating from the deeper layers have hardly any kinetic energy left after traversing the second anode (Fig. 3.1b). In the spectrum of Fig. 3.1a this not a problem at all. Thus: we extract Si data from $\Delta E_1/\Delta E_2+E_r$ spectra and O data from $\Delta E_2/E_r$ spectra.

In Fig. 3.1, the contours are put around the entire signal of a species. Elemental energy spectra of O and Si are obtained by a projection of the content of the corresponding contour on the associated horizontal axis, i.e. ΔE_2+E_r for Si and E_r for O. These elemental energy spectra are used for total-film data analysis.

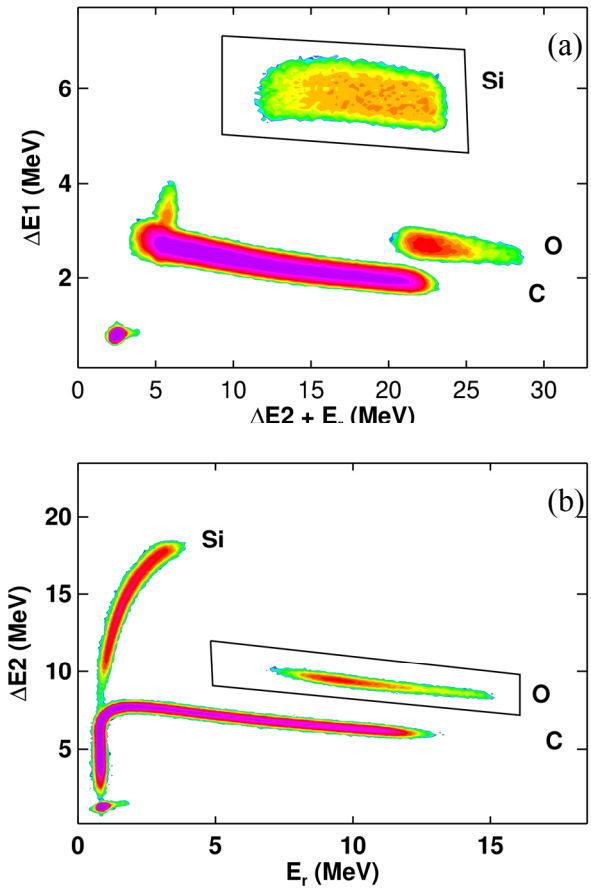

Figure 3.1 ΔE/E ERD spectra after running *real-time* ERD during an entire deposition process using a silicon substrate covered by 1 μm a-C:H. For further details see the text.

For the experiment in Fig. 3.1, the substrate used is a hydrogenated carbon film, thickness approx. 1 μm which is deposited on a silicon wafer by means of thermal expanding plasma [1]. This carbon film enables us to distinguish the Si in the SiO_x layer from that in the Si substrate. The used ion beam is 63 MeV Cu^{10+}, with the total current on the sample of ~10 nA. In the deposition process, the RF power has been changed abruptly from 50 W to 175 W in 5 steps.

3.4 Total-film *real-time* ERD

The O and Si signals in Fig. 3.1 are clearly separated from the other species. As long as the different elements are separable it is possible to determine the total content in a particular contour. At each moment, this content can be converted to the areal density (at/cm^2) of the corresponding element on the substrate. During deposition, the elemental growth rates (as a function of time) can be determined from the increase of the (elemental) areal densities. Once the growth rates of O and Si at a certain time are known we also know the x-value of the material that is deposited at that moment. Since we take into account all the particles we measure it is not necessary to use the reference sample for the determination of the x-value. This method can be used as long as the thickness of the deposited layer does not exceed the probing depth for O or Si, which is in our case about 500 nm, depending on the average composition of the layer.

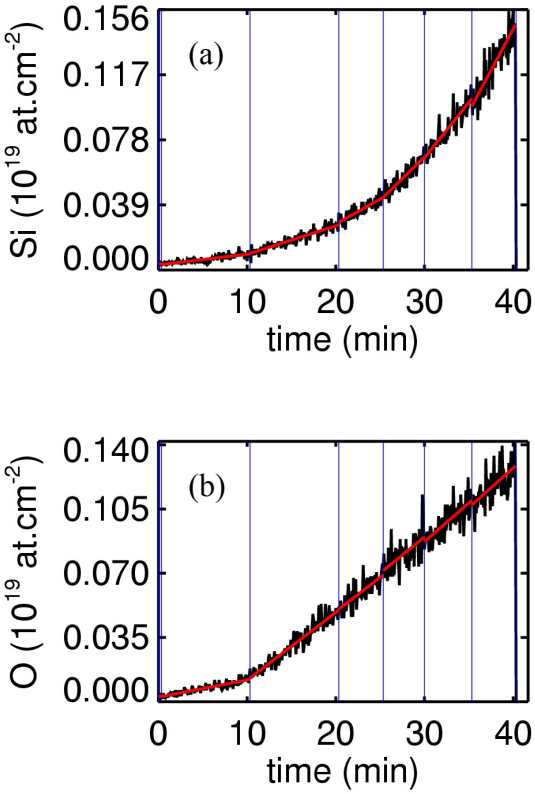

Figure 3.2 The silicon (a) and oxygen (b) growth rate as a function of time. The blue lines indicate the moments of power change.

In Fig. 3.2 the areal densities of O and Si are plotted as a function of time. The power is changed from 50 W to 175 W in 5 distinct steps of 25 W. These points in time are indicated in figure 3.2 by the vertical blue lines. During each time interval the slope of the signal has been fitted and this slope represents the amount of material deposited in the given time interval, i.e. the material growth rate. The values for the growth rate derived from Fig. 3.2 are

depicted in Fig. 3.3 where we find a sharp increase of the amount of silicon deposited with increasing power and a small increase in the amount of oxygen deposited with an increase in power, excluding the first measurement point. In the condition of low power and plenty of oxygen flow (0.75 sccm) the target is poisoned which results in a significantly lower silicon deposition rate. The oxygen deposition rate is in this case limited by the silicon growth rate and not by the number of oxygen particles colliding with the surface, for further details see

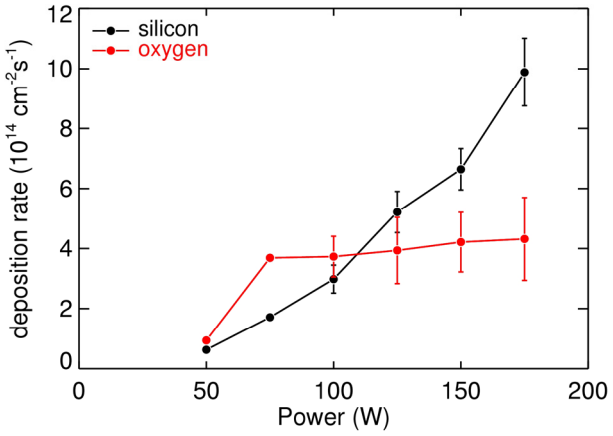

Figure 3.3 The material growth rate as function of power.
The drawn lines serve as a guide to the eye

chapter 5 of this thesis. Please note that a drawback of total-film ERD is that the experimental error in the growth rate increases as the film becomes thicker. In this case the error is large for the higher powers (see Fig. 3.3). This is caused by the fact that, for both O and Si, the total yield that is accumulated during deposition with the higher powers is dominated by the contribution from the under- laying already-deposited lower-power layers. This extra contribution to the yield is in principle constant, but adds considerably to the (Poisson) statistical error in the yield and introduces an extra inaccuracy in the value for the deposition rate.

3.5 Surface selective *real-time* ERD

For surface selective ERD we initially use the same energy projections of the distinct elemental contours made against an energy axis. By only selecting a small window of these contours at the highest energy part, which coincides with the surface of the material, we are able to determine the composition of the material which is currently being deposited. To determine accurately the x-value a measurement of a reference sample is necessary.

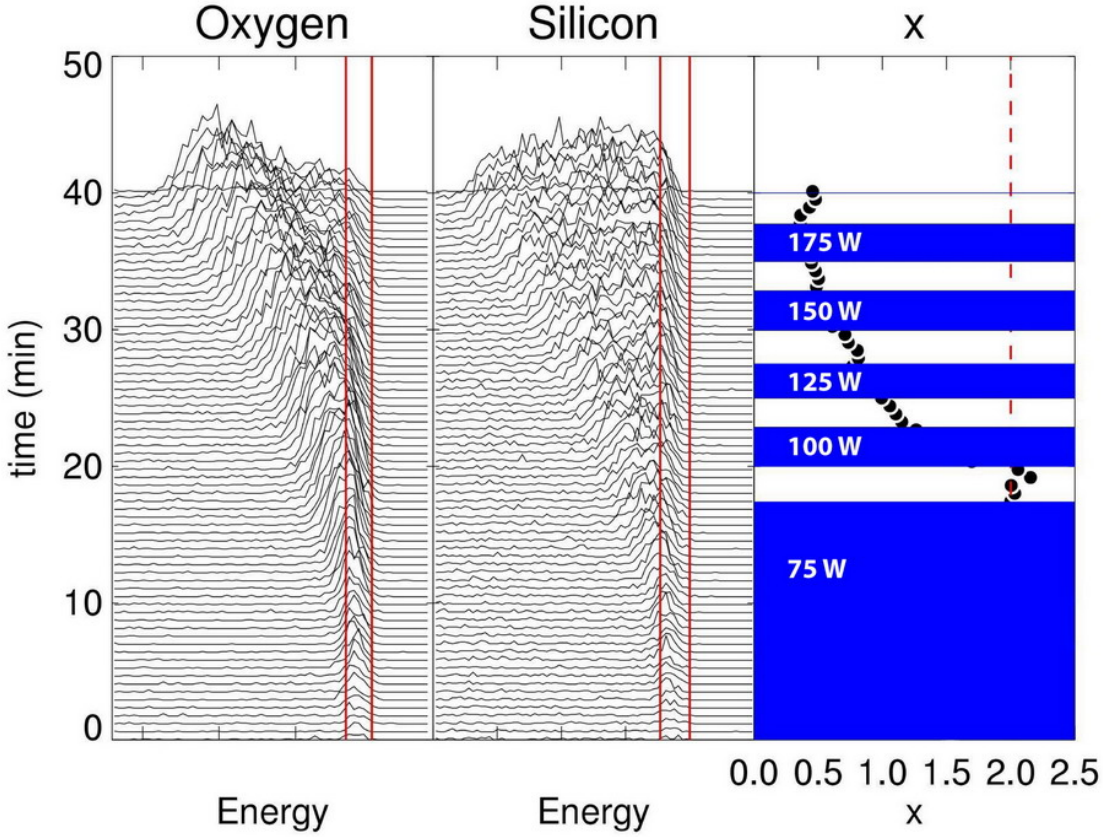

Figure 3.4 Evaluation of the oxygen and silicon elemental spectra as function of time. The surface windows are indicated by the red vertical lines. The x-value determined by the material in the windows is also depicted. For further details see text.

Fig. 3.4 shows how the elemental spectra of O and Si develop in time during the deposition process. For both Si and O holds that every minute a plot is made of the data accumulated in that minute. We analyze the same data stream as in total-film ERD to enable a comparison between both methods. Again the moment of power changes are indicated by blue lines in the right frame of Fig. 3.4. A window which selects the surface region is shown by red lines in both the left and middle frame indicating the oxygen respectively silicon signal. The right frame expresses the development of the x-value as determined by the signal from the surface windows. From considerations that involve the stopping power of SiO_x as a function of the compositions it follows that the x-value is simply proportional to the ratio of the number of counts in the O and Si surface windows. The material in the surface windows needs to be filled by material deposited using the current deposition conditions. This is also the reason why the first time interval (with 50 W) is omitted. If the surface windows reach deep into the

layer, it will long before the measurement reacts on a change in the deposited material composition. If they are restricted to a narrow surface region, the statistics will deteriorate. Furthermore, it makes no sense to use windows that correspond to a layer thickness thinner than the system's depth resolution, which amounts to ~5 nm. In Fig. 3.4 we defined windows that are slightly larger than the depth resolution. Since the deposition rate varies between 1 and 10 nm per minute it took some minutes after each change in RF power before the x-value stabilized. These periods are depicted in Fig. 3.4 by the blue areas hiding the x-values determined for these time-windows. The nice thing about surface selective *real-time* ERD is that total thickness of the deposited film is totally unimportant, as is the type of substrate. Even material deposition on a silicon wafer is suitable. Simply stated: A single substrate is sufficient to monitor the x-value for a range of deposition conditions when using surface selective ERD. The disadvantage of this mode of operation is that the material deposition rate is not determined.

3.6 Comparison of surface selective ERD and total-film ERD

The x-value determined with surface selective ERD, see Fig. 3.4, is compared to the x-value determined from the material deposition rate measured with total-film ERD, Fig. 3.3.

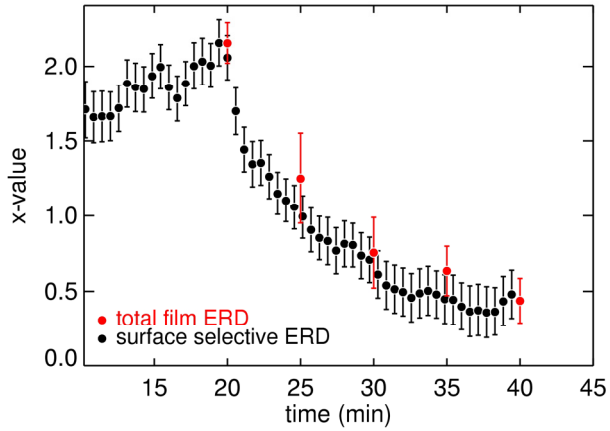

Figure 3.5 The x-value determined by total-film ERD and surface selective ERD. The red dots are derived from Fig. 3.3 and the results are plotted at the end of each time interval.

In Fig. 3.5 the x-value determined by surface selective ERD is indicated by the red dots. The transition period after each power change is clearly visible here. Please note that the observed decrease and subsequent increase in x-value at the start of deposition is meaningless. It is the mixed result of poor statistics due to the few O and Si counts originating from the very first atoms that have been deposited and the 'filling' of the surface windows from Fig. 3.4 as the film grows thicker. The red dots, measured by total-film ERD, are plotted at the time location where the surface selective dots become accurate. The x-values determined by either method coincide with each other, a clear indication that both methods are correct.

3.7 Influence of the ion beam on the argon content of the film

The high-energy ion beam used in ERD can significantly alter the deposited film, i.e. the 63 MeV Cu ions deposit energy in the film and sputtering processes might take place. Although application of a less intense beam will reduce possible effects this might not suffice, since the accuracy of the obtained results, which depends on the amount of detected particles (per second), sets a lower limit to the ion beam current. An increase in the spot size of the ion beam, i.e. a decrease of the ion beam current density, can result in less severe alterations to the deposited film.

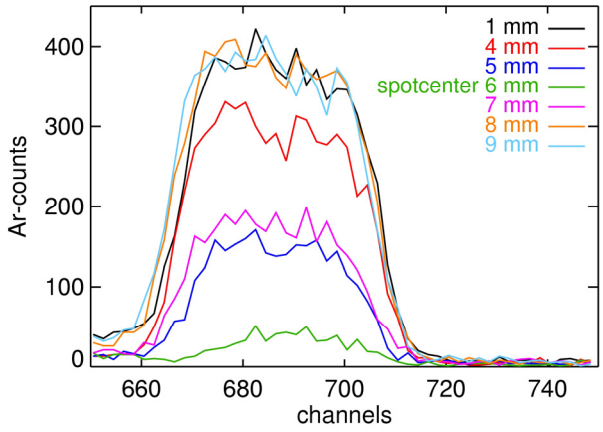

Figure 3.6 RBS spectra of argon in a sample deposited at 175 W and an x-value of 1.65 if not irradiated. Applied ion beam during deposition is 150 nA of 50 MeV Cu^{9+}.

The argon content of a film, deposited at 175 W with an oxygen flow of 1.35 sccm (x = 1.65 without irradiation) and a 50 MeV Cu^{9+} ion beam with a current of 150 nA, has been determined by using RBS. The 2 MeV He ion beam for RBS has a diameter of 1 mm, which is much smaller than that of the ERD ion beam. The RBS Ar spectrum for several positions on the sample is depicted in Fig. 3.6. A clear reduction of the amount of argon in the thin film is found in the center of the ERD beam spot. In Fig. 3.7 the content of the argon profile is depicted as a function of position on the sample. The beam spot is estimated to be 3mm and is indicated by the vertical green lines. It is clear that the ion beam results in a lowering of the argon content. It is also clear that the reduction of the argon concentration only takes place within the area of the beam spot, to the largest extent in the center. Supposingly, during irradiation the temperature variation over the surface area of the sample can be neglected [2]. This indicates that desorption of Ar from the material requires high temperature and/or other phenomena taking place in the ion track which accompanies the passage of the individual ions through the film [3,4]. Further discussion concerning the Ar incorporation in the film can be found in chapter 6.

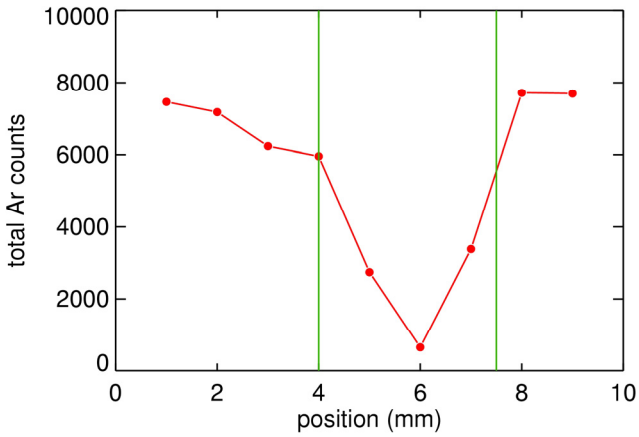

Figure 3.7 the content of the argon profiles as a function of the position on the sample.

3.8 Influence of the ion beam on the x-value of the deposited film

The influence of the ion beam is not limited to the argon desorption from the SiO_x film. Both the x-value and the thickness of the film can be significantly altered due to ion beam irradiation. A series of samples with different x-values is deposited with and without ion beam present during deposition. The x-values demonstrated are x = 0.75 and x = 1.65 deposited at a power of 175 W. The growth time and also the irradiation time amounted to 5 minutes. In Fig. 3.8 the x-value, as measured with RBS, is plotted as a function of the position of the sample for various particle currents. First we consider the films deposited such that they have x = 0.75 without irradiation. It is clear that an increase of the particle current results in a decrease of the x-value, thus more energy dumped into the sample results in a lower x-value. This happens both inside as well as outside the ERD beam spot, so we can conclude that this effect is due to heating of the entire sample.

Comparison of these results with the measurements in chapter 5, where the x-value has been evaluated for samples grown at temperatures above room temperature, reveals that the temperatures reached are in the order of 100 – 200^{o}C.
For the higher x-value, x = 1.65, we find a similar effect, outside of the beam spot. At i.e. 9 mm the x-value reduces when the power transferred to the thin film by the ion beam increases. However, within the beam spot, again indicated by the green vertical lines, we see an increase in the x-value.

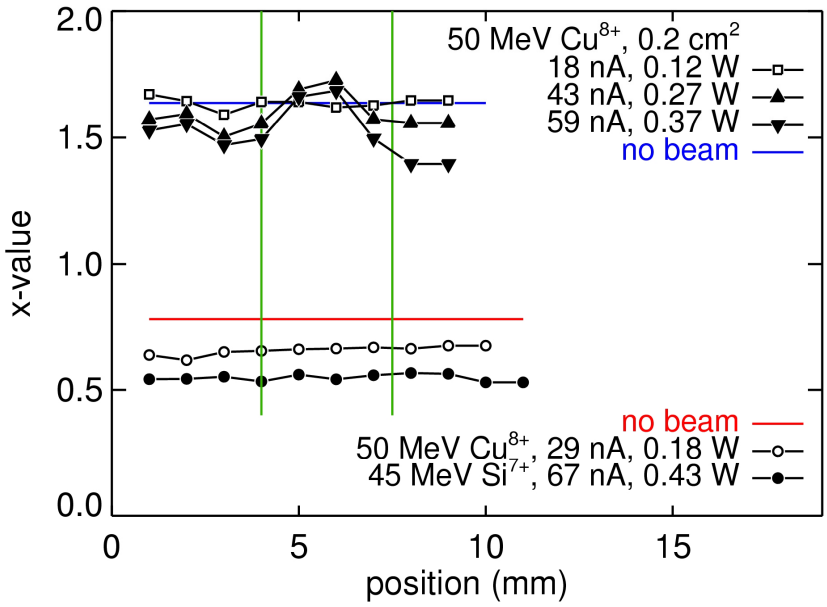

Figure 3.8 Position dependent x-value for films deposited while being irradiated with different ion beam currents. The legend gives the type of ion beam, the beam current and the power deposited by the ion beam in the sample.

3.9 Influence of the ion beam on the layer thickness

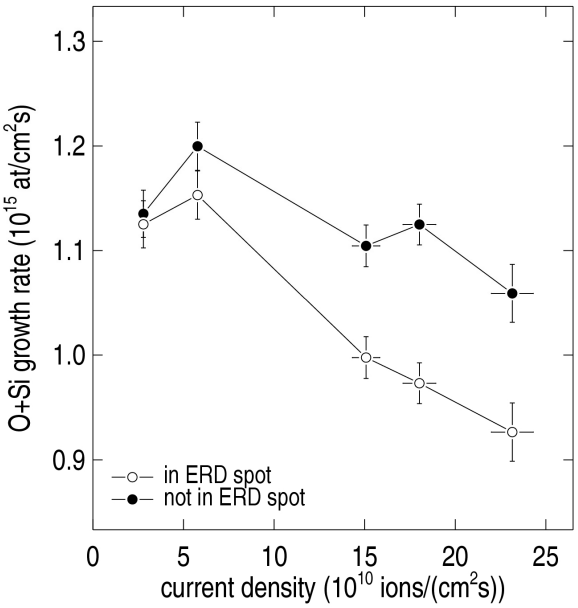

Figure 3.9 O+Si growth rate in and outside the beam spot, as a function of the particle current density. The x-value amounts to ~1.65, see Fig. 3.8.

For the determination of growth rates by using high-energy heavy ions one must be aware of the effect of sputtering of the material as a result of the energy deposition in the electronic system of the solid. In the geometry and with the primary ion beam of the present study, less than about 100 atoms from the surface of the solid are removed per incoming Cu ion [5] . This value is for x >1.5, for sub-oxides with lower x-values this electronic sputter rate is lower [6]. For the particle current density of upto 10^{11}/cm^{2}s (i.e. particle current density in the order of 15 nA/cm^2), applied in the present work, we remove by the ion beam upto about 10^{13} atoms/cm^{2}s. According to this calculation this effect is expected to be a serious problem when the growth rates are in the low 10^{14}/cm^{2}s range. However, we found that layers (x=1.65) deposited under continuous irradiation were upto 10 % thinner than samples without continuous irradiation at a growth rate of ~$2\cdot10^{15}$ at/cm^{2}s. Since we have found (see above) for those samples that the x-value within the ERD spot is larger than the x-value outside the spot in contrast to low x-value samples (see Fig. 3.8), we tend to hypothesize that in the ERD spot the Si-growth rate is smaller than outside the spot, for a thus far unclear reason. However, also other explanations (like enhanced electronic sputtering) are possible. We also conclude that for the lower currents the ion beam induced artefacts (except Ar desorption) are not significant.

3.10 Constant O_2 flow versus constant O_2 partial pressure: an application of *real-time* ERD

In this section we make a comparison between a *real-time* measurement in which the oxygen flow to the system is kept constant and a measurement in which the oxygen partial pressure is kept constant when increasing power.

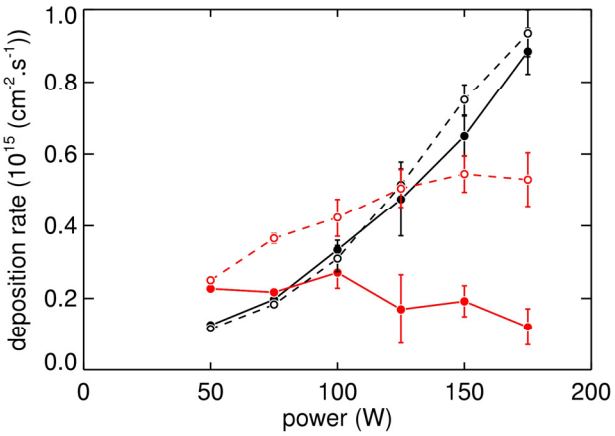

Figure 3.10 The silicon and oxygen deposition rate as function of power. A constant oxygen partial pressure, $6\cdot10^{-4}$ Pa, and a constant oxygen flow of 0.5 sccm are used. The Ar flow amounted to 40 sccm, resulting in a pressure of 0.35 Pa.

In Fig. 3.10 a comparison is made between the silicon and oxygen deposition rate as a function of power using total-film ERD. The evolution of the silicon deposition rate with power is hardly influenced by the different methods to control the oxygen flow. For the oxygen growth rate we find a striking difference between constant O_2 flow and

constant O_2 pressure. As shown before, at constant flow the oxygen deposition rate appears to be relatively constant although at higher powers it appears to decrease. At constant oxygen partial pressure the oxygen growth rate increases with increasing power, but again at higher power we see a flattening in the deposition rate.

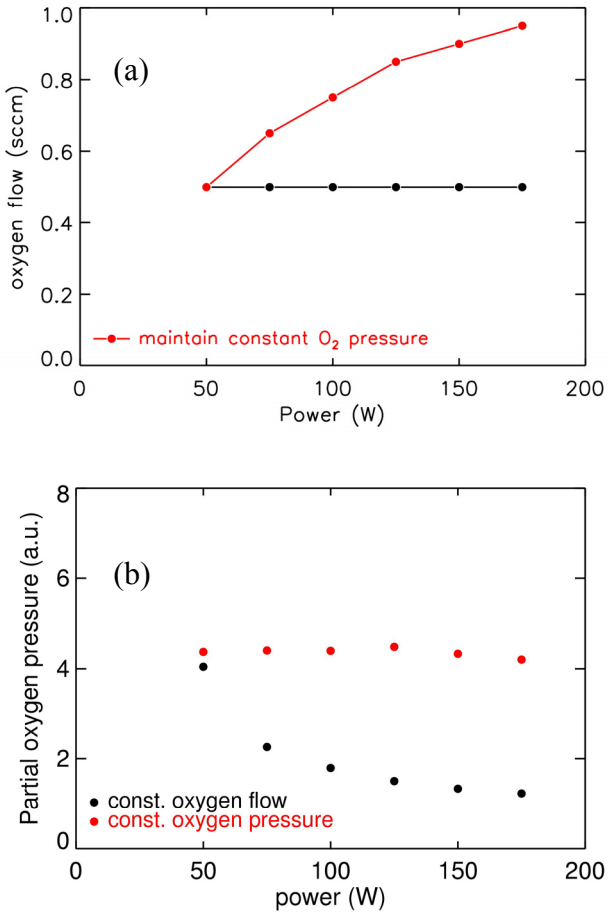

Figure 3.11 (a) The settings for the oxygen flow used and (b) The oxygen partial pressure measured by the mass-spectrometer as a function of power for constant oxygen partial pressure and constant flow to the deposition vessel.

A clue to what is happening is found by monitoring the oxygen partial pressure which in this case is done by the mass-spectrometer that measures the relative amount of oxygen neutrals hitting the anode. Fig. 3.11a depicts the oxygen flow settings used in the depositions, while Fig. 3.11b depicts the count rate for oxygen neutrals in the mass spectrometer as a function of power. The amount of oxygen neutrals found at constant partial pressure of oxygen is indeed found to be constant, which confirms that the pre-determined values that are used to adjust the O_2 flow are correct. However, a clear decrease in the oxygen pressure is found at constant oxygen flow when increasing power. A decrease in the oxygen partial pressure for an increase in RF power can only be explained by a larger removal rate of oxygen from the deposition vessel. Apparently the deposited material, not only on our substrate, but also on the vessel walls, acts as a powerful oxygen pump. It seems reasonable to assume that the

oxygen pump is increasingly effective if more Si is deposited, thus the total pumping capacity for oxygen increases upon increasing power.
The evolution of the O growth rate in the case of the constant partial pressure series has an equivalent explanation. In a first order, simple model the growth rate is limited by both the availability of vacancies on the surface of the growing material and the number of oxygen particles arriving at the surface. At a constant partial pressure the number of oxygen molecules that hit the surface per second is constant for each applied RF power. The density of vacancies on the surface is expected to increase as the power increases, since the Si deposition rate increases. Therefore the O deposition rate is expected to increase. Since the O deposition rate increases less than the Si deposition rate, as can be seen in Fig. 3.10, and therefore the x-value decreases, the simple model that the oxygen incorporation rate is determined by the availability of adsorption sites is not complete.

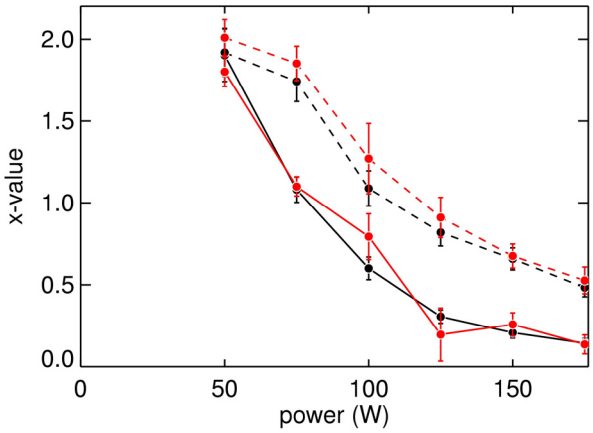

Figure 3.12 The x-value determined for constant oxygen flow (solid line) and constant oxygen partial pressure (dashed line) as a function of power determined with surface selective (black) and with total-film (red) ERD. The drawn lines are to guide the eye.

In fact, the data in figure 3.10 suggest that the oxygen growth rate tends to be constant for a power above 125 W and x<1. For further details concerning the oxygen incorporation during growth, see chapter 5.
The x-value is determined for both situations with both modes of *real-time* ERD and depicted in Fig. 3.12. The two modes of ERD again give equal results. The x-values for constant oxygen flow are lower than for constant partial pressure, notably at higher x-values, as already could have been deduced from the representations in terms of the oxygen and silicon growth rates (Fig. 3.10). Again, the difference is ascribed to an increased oxygen gettering at an increased power. The message is that the gettering of oxygen, and therefore the oxygen pumping speed, depends on the experimental parameters during the deposition. Therefore the ratio between the oxygen partial pressure and the oxygen input flow depends on the experimental deposition parameters. As a consequence it is necessary to monitor the oxygen partial pressure when studying the sticking probability of oxygen and controlling its incorporation rate, despite the difficulty to monitor this partial pressure over a wide range of total pressure.

3. 11 Conclusions

By application of total-film ERD and surface selective ERD we have demonstrated the possibility of using these measurement techniques as tools for monitoring the O/Si concentration ratio and deposition rate in SiO_x during deposition. A single experiment is sufficient to obtain results in a range of plasma conditions.
It appears that the ion beam causes the Ar incorporated to desorb. Deviations of the x-value measured with the beam on the sample compared to the situation without the beam indicate a uniform heating of the sample which limits the ion current that can be applied. For larger current density the effect of the ion beam on the final layer thickness is larger than expected on the basis of the values for electronic sputtering rate determined in ex-situ experiments.
As an application we have shown that the partial O_2 pressure is a more appropriate parameter in the deposition process of SiO_x than the O_2 flow.

3.12 References

[1] J.W.A.M. Gielen, M.C.M. vandeSanden and D.C. Schram, Appl. Phys. Lett. **69** (1996), 152.

[2] E.H.C. Ullersma, P. Ullersma and F.H.P.M. Habraken, Phys. Rev. B **61** (2000), 10133.

[3] M. Toulemonde, C. Trautmann, E. Balanzat, K. Hjort, A. Weidinger, Nucl. Instr. and Meth. B **216** (2004), 1.

[4] C.H.M. Marée, A.M. Vredenberg, and F.H.P.M. Habraken, Mater. Chem. & Phys. **46**, (1996), 198.

[5] W.M. Arnoldbik, N. Tomozeiu and F.H.P.M. Habraken, Nucl. Instr. and Meth. B, **203** (2003), 151.

[6] W. M. Arnoldbik, P. A. Zeijlmans van Emmichoven, and F. H. P. M. Habraken, Phys. Rev. Lett. **94** (2005), 245504.

4

Characterization of the argon plasma and deposited films

4.1 Introduction

Thin layers of silicon sub-oxide (SiO_x) are deposited using an RF magnetron reactive sputtering plasma. A plasma is a partly ionized gas, and in our case the RF field (13.56 MHz) mostly affects the free electrons which gain kinetic energy by following the electric field. The ions are much heavier than the electrons and react therefore only slowly to the changes in the external electrical RF field and will not gain a significant amount of kinetic energy due to the applied power. The energetic electrons can lead to further ionization of the gas by colliding with the gas particles. The free electrons cover macroscopic distances in a single cycle of the RF field whereas the ions are rather immobile. The difference in ion and electron mobility results in a time averaged negative potential for all electrically isolated surfaces in contact with the plasma. The sputtering cathode is electrically isolated and therefore builds up a negative potential. Due to this potential the electrical field points towards the cathode in the vicinity of the cathode and the positively charged ions are accelerated towards the surface of the cathode. The potential of the cathode settles at a magnitude such that the cycle averaged electron current and ion current reaching the surface are equal. The maximum amount of kinetic energy of the ions, when they hit the cathode, is equal to the maximum potential difference between the plasma and the cathode. This energy is released by sputtering atoms and clusters from the surface, i.e., breaking the chemical bonds in the surface of the cathode, and the atoms and clusters will be ejected from the surface. In our

experiments the cathode, often also referred to as the sputter target, consists of a poly-crystalline silicon disc.

The parts of the deposition system that are grounded are by definition at zero electrical potential. Since we have a negative potential at the cathode, which is not grounded, charge conservation requires the plasma itself to be positively charged. There is therefore also a potential difference between the plasma and the grounded parts of the system. However, the energy carried by the ions bombarding these grounded surfaces is substantially lower than the energy of the ions bombarding the cathode and consequently the amount of particles sputtered from the grounded surfaces is significantly lower. The difference in sputtering rate from the cathode and the grounded surfaces, including the deposition surface, is the basis of plasma-sputter deposition.

Particles sputtered by ion impingement on a surface have on average a velocity directed perpendicular to the surface. To make optimal use of the sputtered particles the grounded deposition surface is therefore fixed directly opposing and parallel to the target. Some of the sputtered particles stick to this surface and while sputtering takes place at the cathode, a thin film is formed on the deposition surface. However, not all sputtered particles will stick to the surface that they hit and, moreover, some of the sputtered particles will be deflected from their path by collisions with the background gas while passing though the plasma. To minimize the amount of particles that is not deposited a low total pressure in the deposition system is used, and the mean free path of the sputtered particles is therefore larger than the cathode-anode distance.

As mentioned before, the energetic electrons can ionize the atoms in the background gas, which predominantly consists of argon atoms. The electron impact ionization of argon with an ionization potential of 15.76 eV from the ground state, has been shown [1], under the plasma conditions present in our RF plasma setup, to be either a one-step direct ionization:

$$e^- + Ar \rightarrow e^- + Ar^+ + e^-$$

or a two step ionization process:

$$e^- + Ar \rightarrow Ar^m + e^-$$

$$Ar^m + e^- \rightarrow + e^- + Ar^+ + e^-$$

Where Ar^m is one of the two long-lived meta-stable argon states: the $4s\left[3/2\right]_2$ state, 11.54 eV above the ground state, or the $4s'\left[1/2\right]_0$ state, 11.72 eV above the ground state.

The radiative decay of excited atoms or the recombination of ions and electrons also occurs in the plasma and high energetic photons are emitted. A complete characterization of a plasma therefore requires the measurement of the ion and electron density, the determination of the ion and electron temperature, detection of the photons emitted in the plasma, measurement of the potential of the surfaces in contact with the plasma and the local bombardment of ions coming from the plasma.

Using a Langmuir probe we are able to determine the values of the particle densities and temperatures in the plasma, as well as the local electrical potential. Particles striking the deposition surface are monitored using an energy resolved mass spectrometer placed in the

deposition plane. Optical Emission Spectroscopy is used to monitor the light emission from the plasma, but a direct detection of the argon atoms in a meta-stable state is not possible, since these atomic states are non-radiative and chemically similar to non-excited argon atoms. The presence of argon meta-stables can, however, be indirectly determined through their participation in the ionization processes.
Thin film production is the ultimate goal of plasma sputtering and the characterization of the thin films and the dependencies of their characteristics on the plasma conditions will be addressed subsequently in this chapter.

4.2 Langmuir probe measurements

4.2.1 The Langmuir probe setup

The Langmuir probe is used to determine the properties of the electrically charged particles in the plasma as function of position in the plasma. A small metallic tip (ca. 1 cm in length) collects charged particles from the plasma and by moving the tip to various locations in the plasma the characteristics (kinetic energy and density) of the charged particles are determined. Electrical motors are used to move the tip perpendicular to the target (z direction) and the target in the vertical direction (r direction). At r = 0, the Langmuir probe points to the center of the target. At z = 0 the Langmuir probe touches the cathode surface. Fig. 4.1 shows the Langmuir probe definitions used.

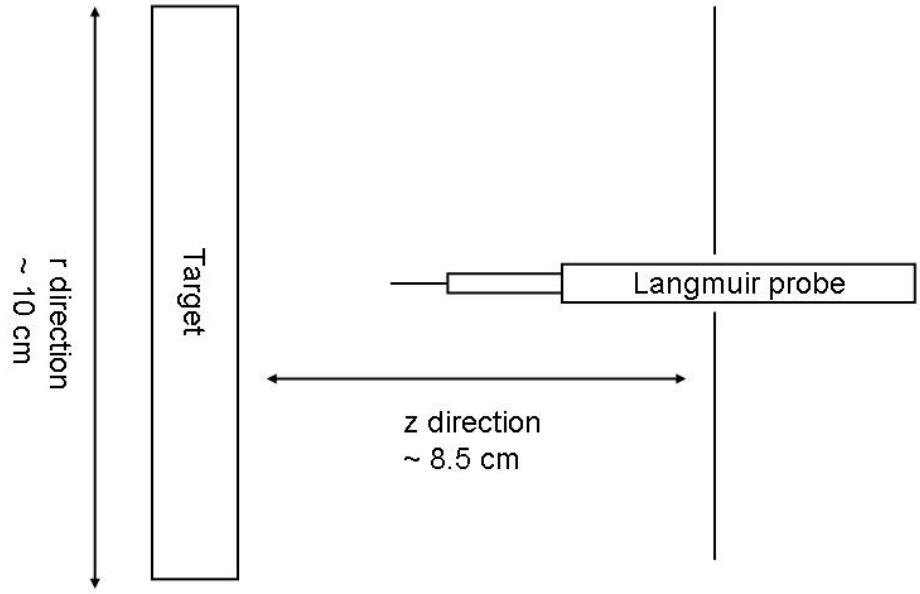

Figure 4.1 The Langmuir probe in relation to the plasma volume

4.2.2 Interpretation of the Langmuir probe results

The charged particle densities, temperatures and the local plasma potential can be determined using the Langmuir probe. However, to collect relevant results, the movement of the charged

particles may not be influenced significantly by any external measurement method. In a magnetron sputter plasma the magnetic field is introduced to confine the plasma closer to the cathode by confining the free movement of the electrically charged particles. The standard Langmuir probe theory [2] therefore has to be modified. In the following the standard Langmuir theory is first presented. Afterwards, the influence of the magnetic field is accounted for.

4.2.3 Langmuir probe: interpretation of the characteristic curve

The Langmuir probe consists of a metal tip to be placed in a plasma. A negative potential on the tip, compared to the plasma potential, attracts the positive ions, and a relative positive potential on the tip attracts electrons and possibly negative ions, although the latter will be disregarded in the following (see Fig. 4.2). If the ion current and electron current are equal in magnitude we find a zero net current. The voltage at which this occurs is called the floating potential. Far below the floating potential only positive ions are collected and we obtain the so-called ion saturation part of the probe characteristic curve. Far above the floating potential only electrons are collected and we measure the so-called electron saturation part of the probe characteristic curve. Assuming that the electrons have a Maxwellian velocity distribution we obtain [3] Eq. 4.1 for the electron current at a given probe potential, V:

$$I_e = en_e A\left(\frac{k_B T_e}{2\pi m_e}\right)^{1/2} \exp\left[\frac{e(V - V_P)}{k_B T_e}\right] \tag{4.1}$$

Where I_e is the electron current, n_e the electron density, T_e the electron temperature, m_e the electron mass, V_P the plasma potential and A the collection probe surface area, e the magnitude of electron charge and k_B the Boltzmann constant.

$$I_s = 0.5 n_i e A\left(\frac{k_B T_e}{m_i}\right)^{1/2} \tag{4.2}$$

The ion saturation current I_s is given by Eq. 4.2, where we have introduced the ion density n_i and the ion mass m_i. Since the total current consists of ions and electrons, a combination of Eqs. 4.1 and 4.2 is necessary to describe the total current collected by the Langmuir probe.

Changing the tip potential leads to a characteristic experimental I-V curve; this is shown in Fig. 4.2. The electron current is given a positive sign and the ion current is depicted as a negative current. The electron saturation part of the I-V curve is omitted since it suffers significantly from interference by the magnetic field.

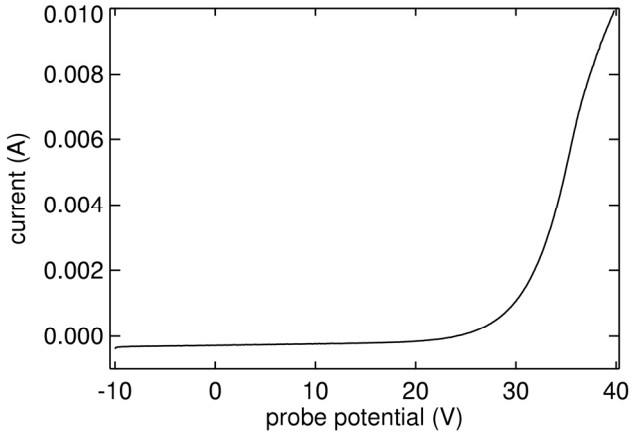

Figure 4.2 An I-V curve measured with the Langmuir probe at r = 1.5 cm and z = 8 cm (0.66 Pa Ar, 100 W)

To obtain results in the presence of a magnetic field an additional iterative procedure is followed. A combined approach of a four parameter fit [3,4] and the introduction of an upper cutoff voltage [5] is taken to estimate ion density, electron temperature, plasma potential and the derivative of the potential, the electric field. Note that it is not possible to estimate the electron density using this method. Far away from the cathode, i.e., several centimeters away from the deposition surface, where the magnetic field can be neglected, it is possible to apply the standard Langmuir probe theory for the interpretation of the I-V curve.

The total current is described by four parameters (I_s, R, V_f, T_e). A fitting parameter, R, which takes into account a variation of the effective collecting area, is introduced using this method. Eq. 4.3 yields the current as function of the parameters.

$$I = I_s\left[1+R\left(V_f - V\right)\right]\left\{1-\exp\left[\frac{e\left(V-V_f\right)}{k_B T_e}\right]\right\} \qquad (4.3)$$

The five step approach to determine n_i, T_e and V_P from Eq. 4.3 is as follows:
First we determine the floating potential V_f and the ion saturation current I_s. As long as electrons play no role Eq. 4.3 reduces to $I = I_s\left[1+R\left(V_f - V\right)\right]$. Fitting the characteristic curve at negative potentials gives values for R and I_s. The electron temperature (T_e) is then estimated by introducing an upper cutoff voltage. The data above this voltage is not taken into account any further. Iteratively fitting of Eq. 4.2 to the curve and reducing the cutoff voltage gives us a series of values for the electron temperature. The minimum of the determined values for the electron temperature is taken as the actual value. This procedure is valid if the used approximation is valid. Thus

$$1 \gg \exp\left(\frac{e\left(V - V_f\right)}{k_B T_e}\right)$$

If this is valid the ion density can be estimated using Eq. 4.2 and the plasma potential can be determined using Eq. 4.4

$$V_P = V_f + \frac{k_B T_e}{2e} \ln\left(\frac{2}{\pi}\frac{m_i}{m_e}\right) \qquad (4.4)$$

Eq. 4.4 is derived from Eqs. 4.1 and 4.2 but since the surface used in our experimental setup is planar and not spherical the constant $\frac{2}{\pi}$ should be replaced by $\frac{1}{2.3}$ [6]. Once the potential is estimated we can also calculate the electrical field present in the plasma.

4.2.4 Langmuir probe: spatial mapping of electron temperature, ion density and plasma potential

We have constructed a spatially resolved map from over 1500 Langmuir probe measurements for a plasma of 100 W and an argon pressure of 0.66 Pa, without oxygen.

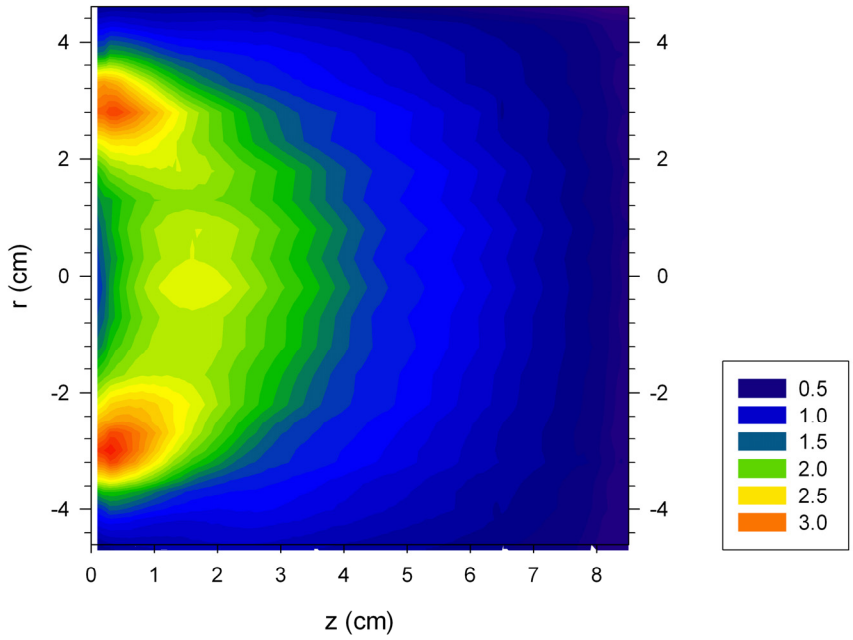

Figure 4.3 Map of the ion density, (in units of 10^{17} ions/m^3) for a pure argon plasma. (0.66 Pa, 100 W)

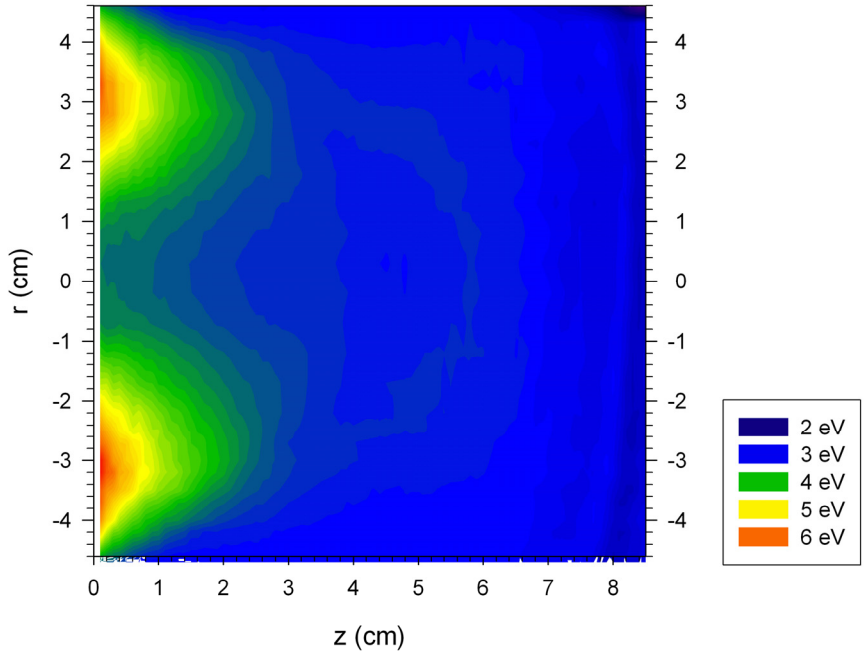

Figure 4.4 Map of the electron temperature for a pure argon plasma. (0.66 Pa, 100 W)

Fig. 4.3 shows the ion density in the plasma, with z being the distance from the sputter target and r the height with respect to the centre of the cathode. Moving the target up (+ direction) results in measurement below the centre of the cathode, thus the bottom part of the ring of the plasma is around r = +3 cm. A clear maximum in the ion density is visible in the plasma ring with a value of about $3 \cdot 10^{17}/m^3$. The value of the ion density in front of a surface is indicative for the local amount of ion bombardment on that surface. Following this argument we find significant ion bombardment near the plasma ring but much less in the centre of the target. The gas density at a pressure of 0.66 Pa amounts to $1.6 \cdot 10^{20}$ particles/m^3. In combination with the measured ion density we derive an ionization degree of ~0.2 % in the plasma ring, assuming the gas temperature to be 300 K.

In Fig. 4.4 the average electron temperature is depicted for the same conditions, derived from the same series of measurements. We find that the average electron temperature is highest in the plasma ring, where it amounts to 6 eV. Only electrons in the high energy tail of the electron distribution can therefore contribute to the one-step electron impact ionization of argon atoms since the ionization potential from the ground state is 15.7 eV. As the average electron energy in the plasma ring is much higher than in the plasma bulk we also expect the concentration of electrons capable of ionizing particles in the plasma ring to be much larger than in the plasma bulk. Hence the ion density is also larger in the plasma ring, see also Fig. 4.3.

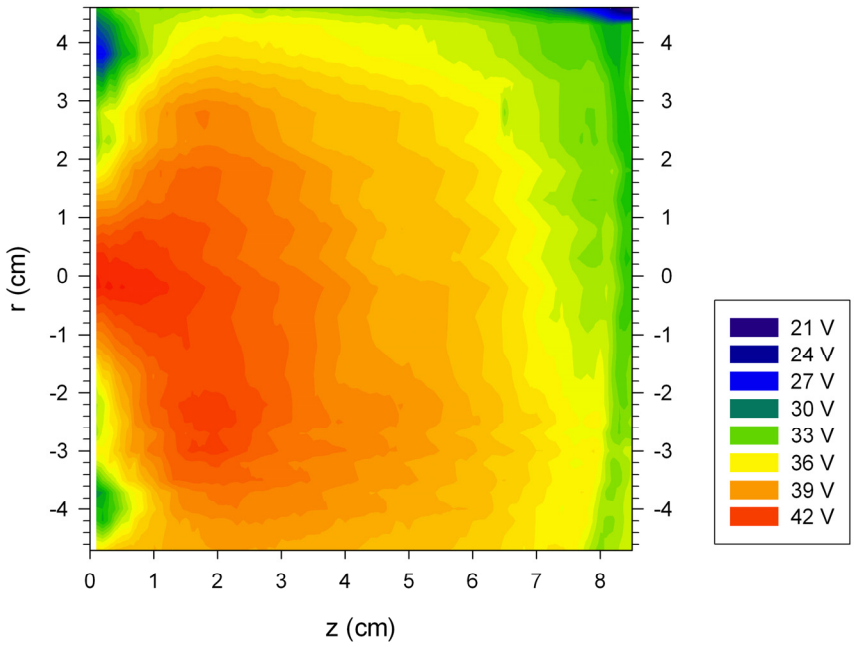

Figure 4.5 Map of the plasma potential for pure argon plasma.
(0.66 Pa, 100 W)

Given the floating potential, electron temperature and ion density we can now calculate the plasma potential, see Fig. 4.5. We note that in the centre of the cathode (r = 0, z = 0) the plasma potential remains high at a value of +42 V, thus ions are not accelerated towards this position. Near r = -3.5 and 3.5 cm we see the potential decrease from a maximum located around 2 cm from the cathode surface. The decrease itself is rather small but significant, keeping in mind that the potential is averaged over the tip length, which is 1 cm, in the direction perpendicular to the target.

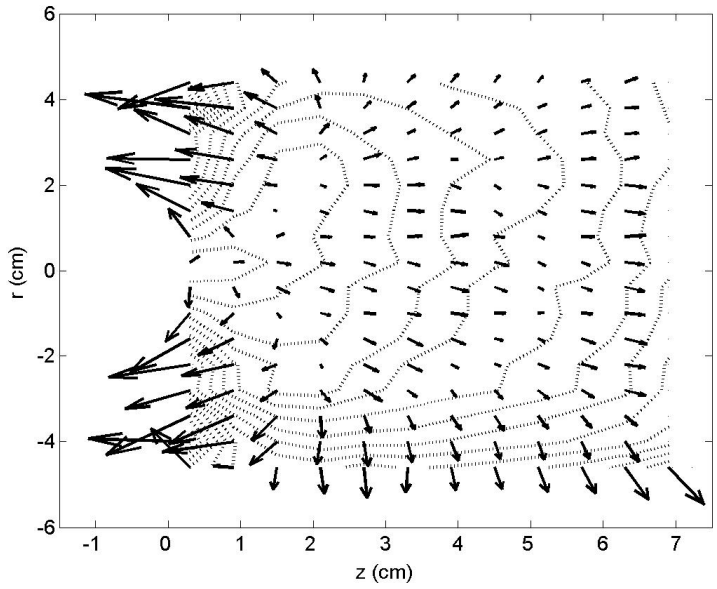

Figure 4.6 The electric field determined from the plasma potential. (0.66 Pa, 100W)

The local electric field strength is equal to minus the gradient of the potential. The electric field derived from the measured potential distribution is presented in Fig. 4.6. We distinguish two regions in the plasma; in the *sputtering plasma region* the electrical field points towards the race-track on the cathode and in the so-called *afterglow region* the field points toward the deposition surface. The largest field strength occurs in front of the race-track, i.e., the part of the target that is most intensively bombarded with ions. It is important to notice that the electrical field inside the plasma is not zero. An electrical field is present, also in the afterglow region and the positive ions are accelerated from the maximum in potential by the electrical field direction towards the deposition surface. The ions therefore have a significant amount of kinetic energy (several eV) once they reach the edge of the plasma which corresponds to the beginning of the deposition sheath.

4.2.5 Plasma properties in front of the race-track as a function of total pressure and absorbed power

A comparison is made for the plasma quantities along a line in front of the race-track and perpendicular to the target surface, for different argon pressures at 100 W, Fig. 4.7, and for different powers at 0.66 Pa, Fig. 4.8. From Fig. 4.7 we deduce that with increasing pressure the ion density increases slightly everywhere along the line, whereas the electron temperature decreases. Thus the electrons have more collisions per unit of time and are therefore capable of ionizing an increasing number of atoms which results in a higher ion density. Since the ion density in the plasma does not change significantly for different pressures we can conclude that the ionization degree in the plasma does change significantly.

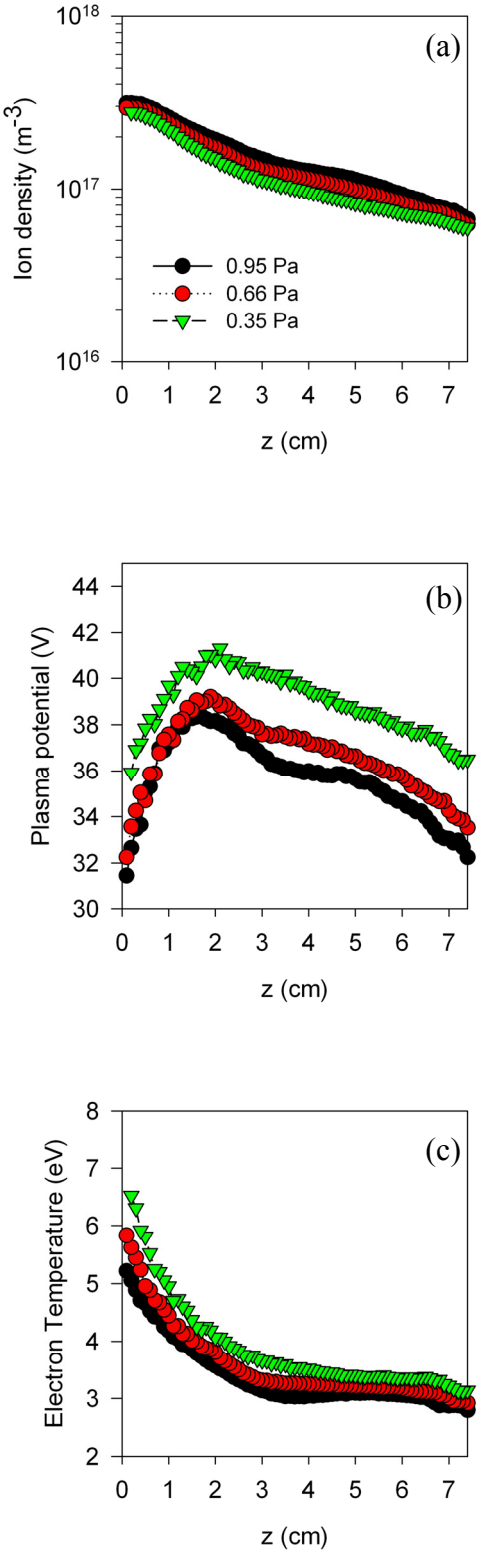

Figure 4.7 (a) Ion density n_i, (b) plasma potential V_p and (c) electron temperature T_e in a pure Ar plasma as function of position and for different pressures at 100 W.

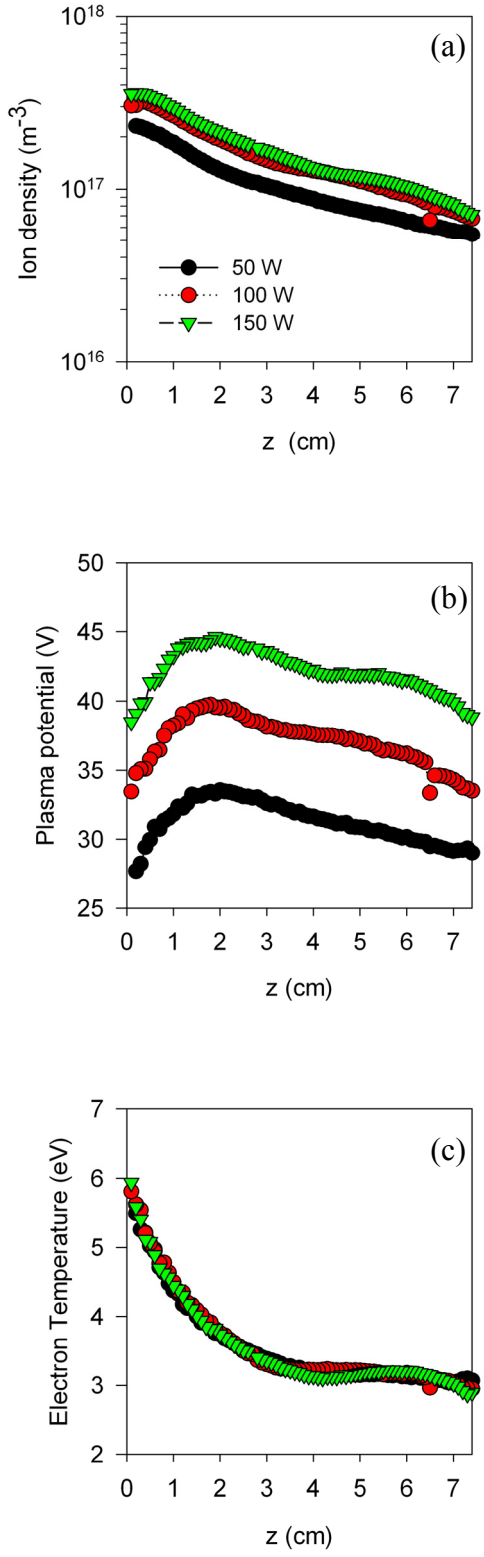

Figure 4.8 (a) Ion density n_i, (b) plasma potential V_p and (c) electron temperature T_e in a pure Ar plasma as function of position and for different powers at 0.66 Pa.

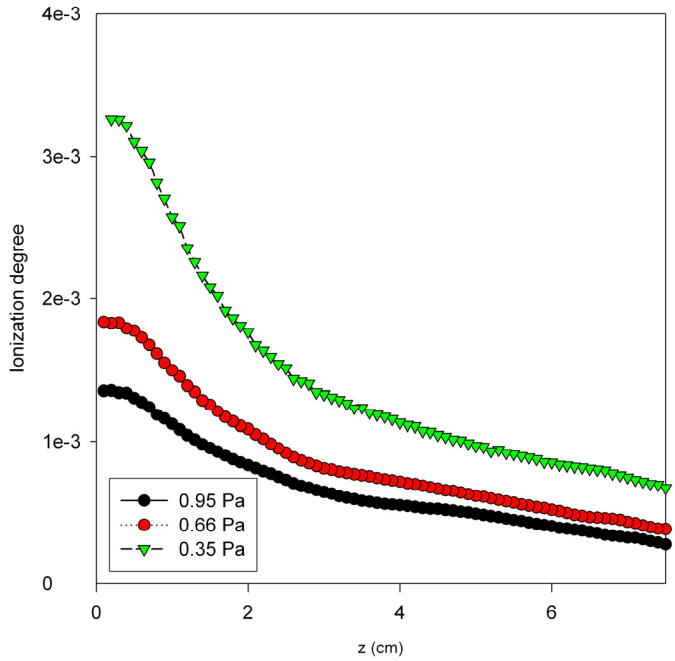

Figure 4.9 Ionization degree in the plasma in front of the centre of the target for various pressures and a power of 100 W.

The ion density is plotted in Fig. 4.9 perpendicular to the target in front of the race-track. The increase in ionization degree is clearly visible and is highest at the lowest pressure. The plasma potential at constant power is shown to decrease with increasing pressure. Apparently the increased amount of ionization increases both the number of free electrons and free ions and the concentration difference between both reduces, thereby reducing the local potential. A very slight shift [9] is also occurring in the location of the maximum in potential. For higher pressure the maximum in potential (Fig. 4.7 c) has shifted a few millimeters towards the cathode. This suggests that the negative potential of the cathode is more efficiently screened by the positively charged particles in the sheath, which corresponds to a greater number of charged particles present in the plasma (see also Fig. 4.7 a).

In Fig. 4.8 is shown, for a total argon pressure of 0.66 Pa, the ion density, plasma potential and electron temperature as a function of RF input power. Clearly, the electron temperature is unaffected by a change in power in the region 50 - 150 W. However, the ion density in the plasma is affected by a change in the power. An increase in power increases the ion density in the plasma. Also the plasma potential increases with increasing power. Clearly, the difference between positive and negative charge present in the plasma changes to contain a larger amount of positive charges with increasing power. The location of the maximum in potential, with respect to the cathode, does not vary as a function of the RF power, at least in the investigated range of conditions. The screening of the negative potential of the cathode by positively charged particles from the plasma seems unaffected by the amount of RF power. Apparently, the screening of the cathode is more dependent on the total number of particles present in the plasma than on the amount of ions in the plasma. The spatial extent of

the cathode sheath depends on the pressure in the system but not on the RF power supplied to the plasma.

4.3 Mass spectrometry

4.3.1 Mass spectrometer configuration

Particles bombarding the deposition surface are monitored using the mass spectrometer with an entrance aperture, which is mounted in the plane of the deposition surface and parallel to the sputter cathode. Fig. 4.10 shows the configuration with respect to the cathode. Positive ions created close to the cathode will be accelerated towards this surface as the electrical field points towards this surface. Particles from the remainder of the plasma might reach the

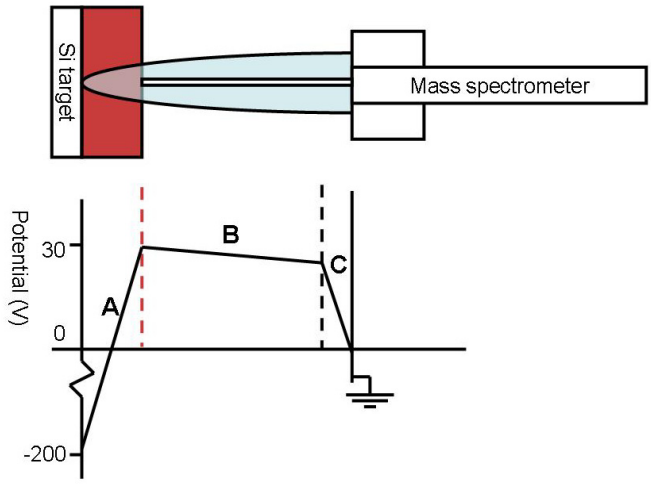

Figure 4.10 The mass-spectrometer. Ions created in the red zone are accelerated towards the target while the sputtered particles follow the blue cone towards the deposition surface. The detection volume of the mass spectrometer at low pressure is indicated by the white cone. Values for the potentials are indicated in the lower figure which also depicts the cathode sheath (A), potential fall across the plasma afterglow (B) and the deposition sheath (C).

deposition surface where we can detect these particles with the mass-spectrometer. The mass-spectrometer has an effective detection cone, which means that ions created in this cone, and with the proper direction, will reach the mass spectrometer. The sputtered particles are spread from the impact point of the sputtering ion in an approximately “cosine square” spatial distribution [8]. In order for a sputtered particle to be detected by the mass-spectrometer in the plane of the anode, the ionization process of the sputtered particle has to take place in the so-called afterglow region of the plasma and within the detection cone of the mass-spectrometer. The ionized sputtered atoms are otherwise not able to overcome the quasi-electrostatic plasma potential.

4.3.2 Mass spectrometry: Basic ion properties

To illustrate the variety of ions coming from the plasma we have measured the mass spectrum at 0.66 Pa and 100 W, see Fig. 4.11. Only ions with around 34.5 eV of kinetic energy (approximately the plasma potential) are detected. The mass scan reveals a wide range of different particles in the plasma. The detection of mass/charge = 40, attributed to the main argon isotope, is suppressed to avoid detector damage. The main species contributing to a certain mass/charge ratio are also denoted in Fig. 4.11. Apart from easily identifiable ions such as Ar^+ and Si^+ we find a number of clusters, Ar_2^+, $SiAr^+$, Si_2^+ and Si_3^+. Other mentionable species in Fig. 4.11 are ArH^+, Ar_2^+ and SiO^+. As we will show later in chapter 5, the SiO^+ ions detected are originating from the cathode. For every species it is possible to determine the energy profile of the ions entering the mass-spectrometer. The question arises what species are actually important contributors to the film growth.

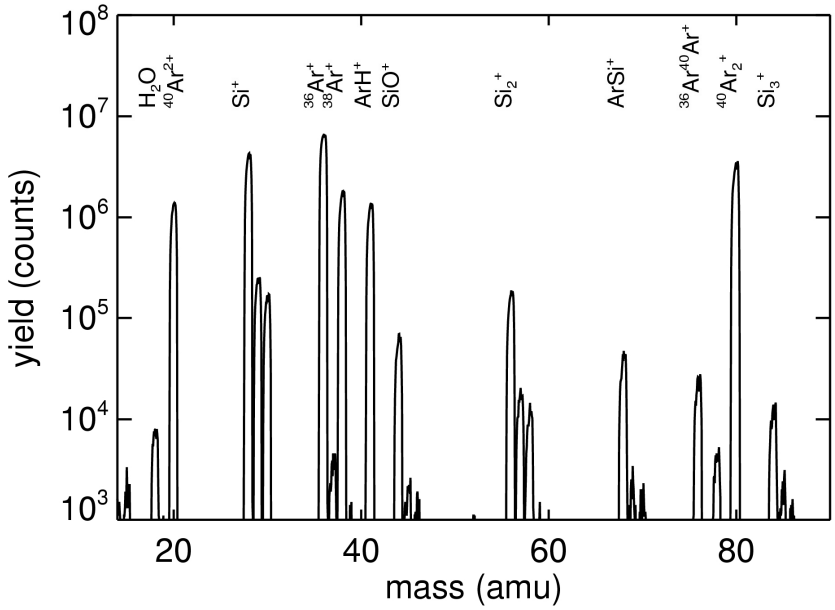

Figure 4.11 Mass-scan for positive ions with energy of 34.5 eV, $^{40}Ar^+$ is omitted (0.66 Pa, 100 W)

In Fig. 4.12 the high energy negative ions (-162 eV) are depicted. The only species present in a significant amount is O^-. Although the kinetic energy carried by the negative ions is quite large, for the total amount of energy given to film the positive ions are more important.

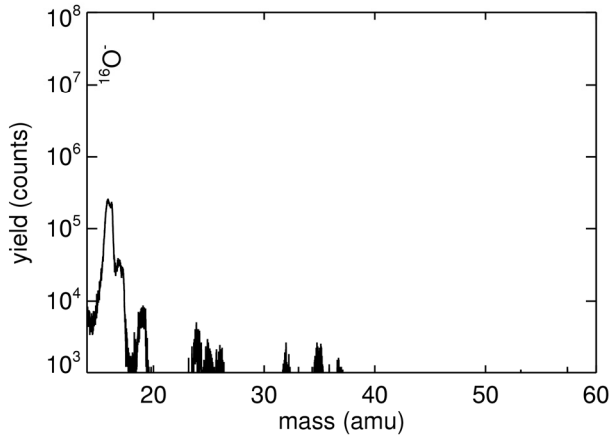

Figure 4.12 Mass-scan for negative ions with energy of -162 eV (0.66 Pa, 100 W)

The positive ions measured at the anode level with the mass spectrometer are created in the afterglow, thus between the point of maximum plasma potential and the deposition surface. Positive ions created in the plasma ring, which are also in the sputter plasma region, are accelerated towards the sputter target. The sputtered particles can also be charged. However, positively charged sputtered particles cannot overcome the plasma potential near the cathode since their kinetic energy cannot be greater than the energy of the ions accelerated towards the surface, which cause the sputtering.
It is tempting to take the amount of measured Si^+ ions with the mass spectrometer at the anode level as a measure for the amount of material being deposited. However, in Fig. 4.11 we have already seen that the abundance of ions like SiO^+ and $ArSi^+$ and clusters of Si_n^+ arriving at the growth surface is certainly not zero, and they may contribute significantly to the thin film growth. However, one should be cautious about judging the relative contribution of the various atomic and molecular species based on the ion signal, since their relative ionization rate is not necessarily comparable in the plasma. We will therefore discuss the ionization mechanisms and rates for several species in the following section.

Although negatively charged sputtered species are accelerated away from the cathode, we estimate [9] that the amount of negatively charged silicon is two orders of magnitude lower than the amount of sputtered positive silicon ions. The production of both the negative ion and positive ion silicon production is greatly dependent on the oxygen coverage of the cathode. For higher oxygen coverage of the surface a higher amount of sputtered secondary ions is observed. SIMS studies [10] revealed that the secondary positive-ion yield lays four orders of magnitude below the amount of neutrals that are sputtered. In combination with a silicon sputtering yield of 0.33 at 200 eV [11], we find a silicon secondary positive ion yield three orders of magnitude lower than the amount of sputtered neutrals. In conclusion, the amount of negative secondary silicon ions is estimated to be at least 5 orders of magnitude below the amount of sputtered neutral particles, and their contribution to the plasma characteristics and film growth is therefore considered negligible. Moreover, the absence of

Si^- ions in the negative ion spectrum, given in Fig. 4.12, means that the Si^- ions that are expected to come from the cathode, do not survive the transfer to the deposition region.

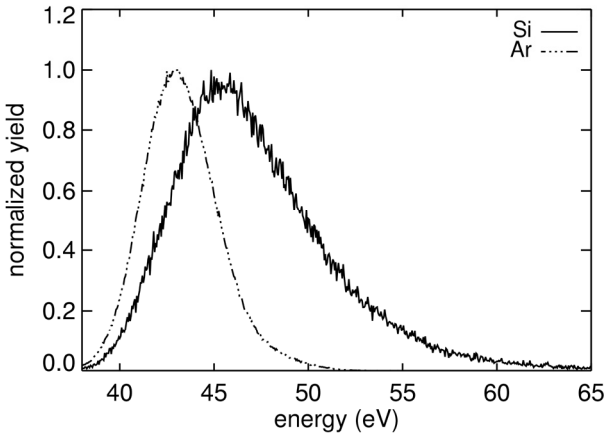

Figure 4.13 Normalized energy profiles of silicon and argon ions at 0.2 Pa argon pressure and a power of 150 W. Oxygen partial pressure is $1.38 \cdot 10^{-3}$ Pa

In Fig. 4.13 we present the normalized energy distribution of ^{29}Si and ^{38}Ar at 0.2 Pa and 150 W. Peak position, width and contents are specific for each ion. The peak position is equal to the deposition sheath potential fall plus the energy of the ions when they have reached the edge of the sheath. The shape, like the appearance of a high energy tail, contains information about the ion transparency of the plasma and possibly the origin of the ions. A low energy tail can be an indication that the deposition sheath is no longer collision free. The width of the peak is a convolution of the ion energy profile with the response function of the energy resolved mass-spectrometer. The area-under-the-curve of the total peak is proportional to the total number of ions of a certain species bombarding the surface. In Fig. 4.13 we see a narrow profile for argon with a small tail at high energy and for silicon ions a much broader distribution. The main argon ion peak is assumed to be argon which reaches the deposition sheath with thermal energy, and these ions are subsequently accelerated over the plasma sheath. The small tail originates from ions that have gained energy, at least for a small part, in the electric field present in the plasma. It is also seen in Fig. 4.13 that the silicon ions have a higher kinetic energy than the argon ions when they reach the deposition surface. The measured silicon ions originated as neutral silicon atoms sputtered from the cathode and have subsequently been ionized in the afterglow. These sputtered particles can have a significant amount of kinetic energy which is not removed during the ionization process, as seen in the energy distribution of the silicon ions. The maximum in the silicon energy profile is expected to be at the silicon surface binding energy, 4.7 eV [12].

4.3.3 Ion bombardment of the anode: Ion energy profile at low pressure plasmas

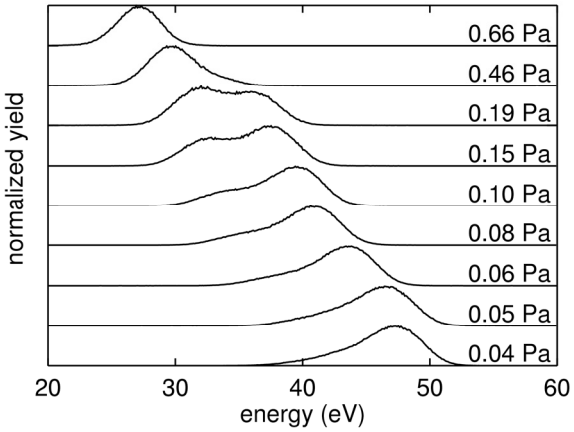

Figure 4.14 The Ar^+ ion energy distribution for lower pressures and for an injected power of 60 W.

In Fig. 4.14 the energy distribution is shown for argon ions at various pressures. When decreasing the pressure from our "standard deposition pressure", 0.66 Pa, to lower values the plasma potential increases. (See also Fig. 4.7) A second peak appears in the argon ion mass spectrum at very low pressures, this suggest that not all the detected ions have the same origin in the plasma. For the "normal pressure", 0.66 Pa, we assume that the maximum in energy of the peak is related to the plasma potential near the deposition surface, see also Figs. 4.7 and 4.8. For lower pressures the plasma potential increases, i.e., the density of ions compared to the density of electrons has increased. Or stated differently, the electrons from the plasma are collected by the walls a little more efficient due to an increase in the mean free path of the electrons. This is expected to be compensated by a relative increase in the number of positively charged particles, thus the plasma potential increases. Both the additional electrons at the wall including the cathode and the increased amount of positive ions in the plasma give rise to an increase in the magnitude of the electrical field. For a pressure of 0.19 Pa we note a large shoulder in the ion energy distribution function towards higher energy, which becomes the most important peak at 0.15 Pa. The second peak has completely overtaken the primary peak for a pressure of 0.1 Pa. The second peak is interpreted as due to ions which originate from the region of the maximum in the plasma potential near the plasma ring and traverse across both the plasma and the deposition sheath without losing energy due to collisions. The peak at lower energy is believed to be ions which interacted, i.e. in a charge exchange process, with particles from the background gas and resembles the particles that only have gained energy over the deposition sheath.

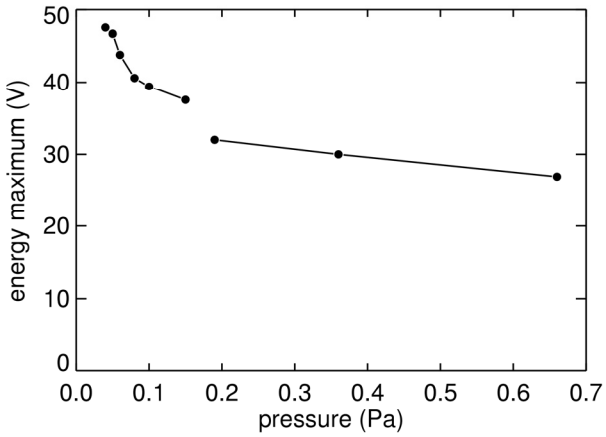

Figure 4.15 Energy at which most argon ions are available as a function of argon pressure. The discontinuity coincides with the shift of the maximum between the two peaks.

The peak position of the peak with highest magnitude is depicted in Fig. 4.15. Here we define the peak position as the energy with the largest yield in the spectrum, without taking the shape of the peak into account. The discontinuity in this picture coincides with the location where the highest magnitude changes between the two peaks. By comparison between Fig. 4.15 and 4.7c we can clearly see that the plasma potential at a given pressure, as determined with the Langmuir probe, yields significantly higher values (34 V vs. 28 V for 0.66 Pa). However we have also to take into account that the power applied in Fig. 4.15 is 60 W. The graphs shown in Fig. 4.8 clearly indicate a voltage drop of about 1V per 10 W extra power in the given power range. Therefore we find that the potential determined by the Langmuir probe is 30 V vs. the 28 V determined by the mass spectrometer for an argon plasma at 0.66 Pa and 60 W of power, and therefore consistent with our description, since this difference is considered to be insignificant. Another effect can be the limited spatial resolution of the Langmuir probe. It is conceivable that the potential maximum is higher and is distributed over a narrower region.

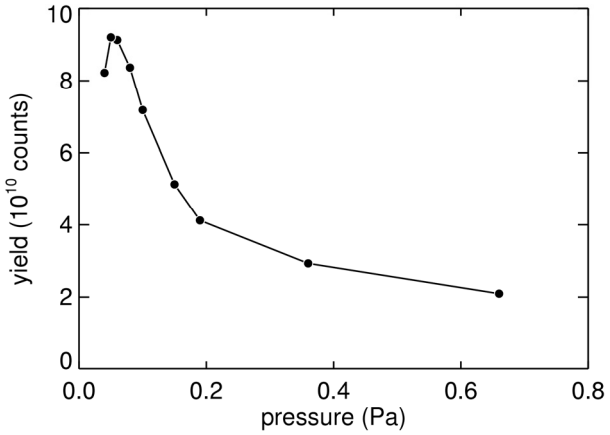

Figure 4.16 Total content of the argon ion energy profiles shown in Fig. 4.14

In Fig. 4.16 the total amount of Ar^+ ions in the spectra given in Fig. 4.14 is shown as a function of total pressure. Starting from the "normal deposition pressure", 0.66 Pa, and going to lower pressure we find an increase in the total amount of measured ions. Apparently, the increase in potential difference between plasma and substrate increases the unperturbed flow of ions towards the deposition surface, thus there are less collisions between charged particles and the background gas. This positive ion flow can be interpreted as the argon ion current towards the deposition surface. A subsequent decrease in the current is visible from 0.06 Pa and is associated with a decrease in the amount of argon ions in the plasma discharge. It is worth mentioning that plasmas below the lowest pressures depicted in this graph can not be sustained long enough to make measurements. The increase in the measured ions when reducing the pressure from 0.66 to 0.35 Pa is accompanied by a small decrease in the ion density in the plasma (see also Fig. 4.7).

4.3.3.1 Estimation of the argon ion bombardment at the deposition surface

An estimation of the flux of argon ions bombarding the deposition surface can be made, although a complicating factor is the change in the shape of the argon ion energy distribution, which subsequently indicates that the kinetic energy distribution of the flux of argon on the deposition surface is different for the varying deposition conditions. At low pressure there is a large fraction of the ions which seem to originate from the plasma ring. For these conditions, we find an ion density (n_i) of about $7 \cdot 10^{10}$ cm^{-3}, at 0.35 Pa at a position of 5 cm see Fig. 4.7. At this position the ions originating from the plasma ring have been accelerated to an energy of at most 2 eV, corresponding to a velocity in the direction of the deposition surface (v_i) of $3.1 \cdot 10^5$ cm/s. Since we are in a weakly collisional regime, we assume that these ions reflect the ion flux at the deposition surface. Using Eq. 4.5 we find the particle flux (Φ_i).

$$\Phi_i = n_i v_i \qquad (4.5)$$

Following this method we estimate an upper limit of the ion flux to be $2.2 \cdot 10^{16}$ ions/(cm^{2}s), at 0.35 Pa.
Another way of estimating the ion flux on the deposition surface is by considering the plasma to be in a collisional regime, at higher pressures. Following Fig. 4.9 we have an ionization degree for argon of $3 \cdot 10^{-4}$ near the deposition surface sheath. The number of particles striking a surface is given in Eq. 4.6

$$\Phi = \frac{\bar{p}}{\sqrt{2\pi m k_B T}} \qquad (4.6)$$

Given the number of neutral particles striking a wall at room temperature, an argon pressure of 0.95 Pa, an ionization degree of $3 \cdot 10^{-4}$ and a complete thermallization of the ions, we find the Ar ion flux hitting the surface to be $7 \cdot 10^{14}$ ions/(cm^{2}s), which is considered to be a lower limit. Following Fig. 4.15 we estimate the measured ion flux at 0.95 Pa to be a factor of two lower than the flux at 0.35 Pa. Thus by comparing the numbers following from the two different types of estimation we note a difference of one order of magnitude. This seemingly large difference is probably due to non-realistic nature of the assumptions in the lower limit approximation: it is difficult to conceive that the ions are completely thermalized and have an isotropic velocity when entering the sheath. In the following sections of this thesis we will assume the upper limit value to be valid. However for both estimations it can be concluded that the ion flux at the growth surface is appreciable in comparison with the growth rate of the film.

4.3.4 Silicon ion yield as a function of total pressure

The amount of Si^+ ions detected is depicted for various pressures in Fig. 4.17. Within the considered pressure range the amount of silicon ions found in the plasma increases linearly with the total pressure of argon. Since the amount of collisions between a constant concentration of sputtered particles and gas particles increases linearly with the number of gas particles, it seems that the argon atoms are responsible for the ionization of the sputtered silicon atoms. It is unlikely that the ground state Argon atoms can have sufficient kinetic energy to ionize the Si atoms (IP= 8.15 eV).

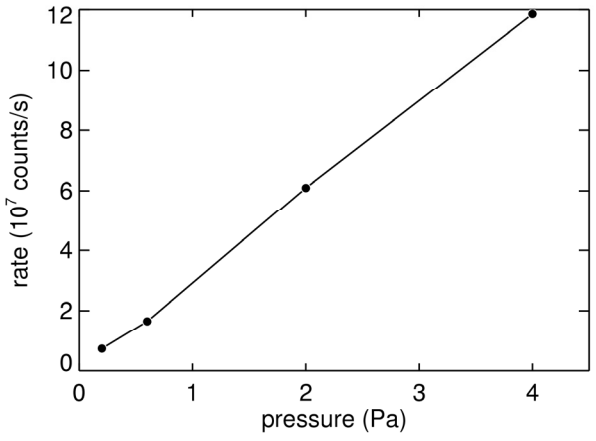

Figure 4.17 The total number of silicon ions as a function of pressure and for a power of 150 W

Based on the observed linearity with the argon pressure the most likely candidate for the silicon ionization process involves the interaction with an argon atom. It can either be an ionization process due to collisions with argon meta-stable atoms, the so-called Penning ionization.

$$Ar^m + Si \rightarrow Ar + Si^+ + e^-$$

or a so-called charge exchange reaction in a collision with an Argon ion

$$Ar^+ + Si \rightarrow Si^+ + Ar$$

The latter process is most likely enhanced by the presence of nearly resonant electronic states in the Si^+ ion. Since the observed number of Si^+ ions is proportional to the argon total pressure, then, for the Penning ionization process to be dominant, the number of meta-stable argon atoms resident in the plasma should also be proportional to the amount of neutral particles, independent of the pressure. Indeed the proportionality constant between argon meta-stable particles and the argon neutral particles is only weakly dependent on the electron temperature through the ratio of the rate constants for electron impact meta-stable creation and electron impact meta-stable annihilation. At higher pressures the amount of silicon which is thermalized in the gas can become significant. For these gas-phase silicon atoms Penning ionization is more likely due to the limited velocity of both the silicon atoms and the argon meta-stable. Since in Fig. 4.17 we see no evidence in an additional increase of the amount of detected silicon ions, we conclude that in our system the amount of thermalized silicon particles at a pressure of 4 Pa is still negligible [1].

4.3.5 Sputtered clusters of silicon

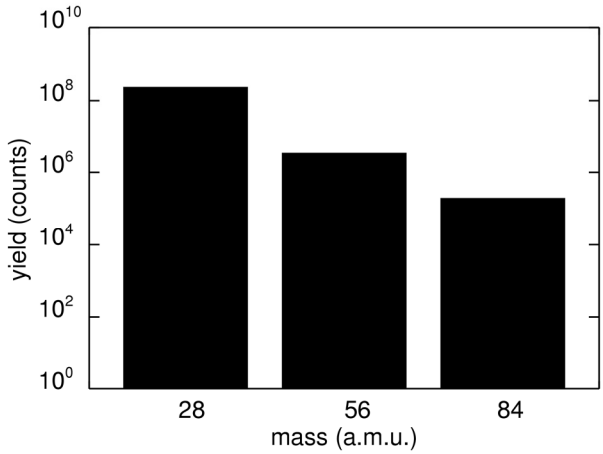

Figure 4.18 The amount of silicon cluster ions compared to silicon ions

In Fig. 4.18 the amount of Si_2^+ and Si_3^+ found in a plasma without oxygen and at a pressure of 0.66 Pa and 100 W of absorbed power is shown. Clusters have been found for different materials, i.e. Si and Ni [13,14]. Under the assumption that the relative ionization rate for the different ions is comparable in the afterglow region we find that the most important ion is atomic Si^+. However, the amount of kinetic energy of the sputtered fragments is more or less

similar to that of single atoms and consequently the larger fragments have a lower velocity, thus the time to get ionized is larger. Moreover, since the clusters are larger than the atoms these fragments have a larger geometrical cross-section, and although this does not necessarily mean that the ionization cross section is larger, it is conceivable that the difference between silicon ions and ionized silicon clusters is smaller than the difference between silicon neutrals and neutral silicon clusters. The contribution to the deposition process from silicon clusters is therefore expected to be less than 1 %. We will therefore neglect the silicon clusters in the description of film formation.

4.4 Thin film deposition: Silicon deposition rate

The silicon deposition rate is of pivotal importance to the whole deposition method. A high deposition rate will generally not allow depositing films of a given thickness very accurately and a low deposition rate, will take too long. For the purpose of depositing silicon sub-oxides, the use of magnetron sputtering allows us to accurately tune the material deposition rate in the desired range. For the moment we will only focus on the silicon deposition rate, but as we will show in chapter 5, there is no substantial change in the silicon deposition rate when adding a small amount of oxygen to the plasma.

4.4.1 Silicon deposition rate as function of absorbed power

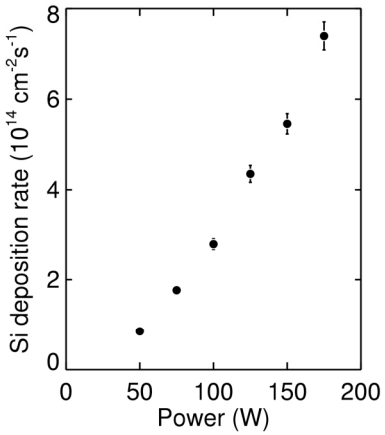

Figure 4.19 Silicon growth rate versus power at 0.66 Pa

In Fig. 4.19 the silicon deposition rate as function of absorbed power is depicted. The argon pressure amounts to 0.66 Pa. The deposition rate is determined using RBS on a sample deposited on a carbon substrate. The deposition rate shows an above-linear increase. Following ref. 7, we find this supra-linear increase to be related to the increase in cathode potential. The cathode potential increases sub-linearly with the applied power which suggests that the fraction of power utilized in the deposition process does not remain constant when increasing the total power to the system. Put differently, we find the confinement of the plasma to become less efficient when increasing the amount of energy in the plasma.

4.4.2 Silicon deposition rate as a function of pressure

The silicon deposition rate is depicted for plasma deposition with argon pressures ranging from 0.2 Pa to 0.8 Pa in Fig. 4.20a. Power is kept at 100 W. The deposition rate is measured right in front of the cathode. At these low pressures the deposition rate of silicon is constant and amounts to approx. 0.05 nm/s. For higher pressures, 0.4 to 4.0 Pa depicted in Fig. 4.20b, the deposition rate decays with increasing pressure. At these pressures the sputtered particles increasingly collide with the background gas and thereby lose their initial directionality; the particles which lost their initial direction will be deposited elsewhere in the system. Hence the amount of material deposited on the surface due to scattered particles can be neglected in the first approximation. The amount of material not deflected is traditionally described by the Keller-Simmons formula (Eq. 4.7) [15].

$$r = \phi_0 \frac{p_0 L_0}{pL}\left[1 - \exp\left(-\frac{pL}{p_0 L_0}\right)\right] \tag{4.7}$$

This relation describes the deposition rate of a given material, r, as a function of the number of sputtered particles per unit of time and area, ϕ_0, the gas pressure, p, and the distance between the growing film and the cathode, L.
The so-called throw distance, $p_0 L_0$, is a characteristic distance-pressure product specific for the given sputtered particles and the plasma. In general this is a constant value which again is dependent on the electrical power supplied to the plasma [16]. The fit of the Keller-Simmons formula yields a ϕ_0 of $3.63 \cdot 10^{14}$ part./sec. while for the throw distance we find 10.4 Pa cm.

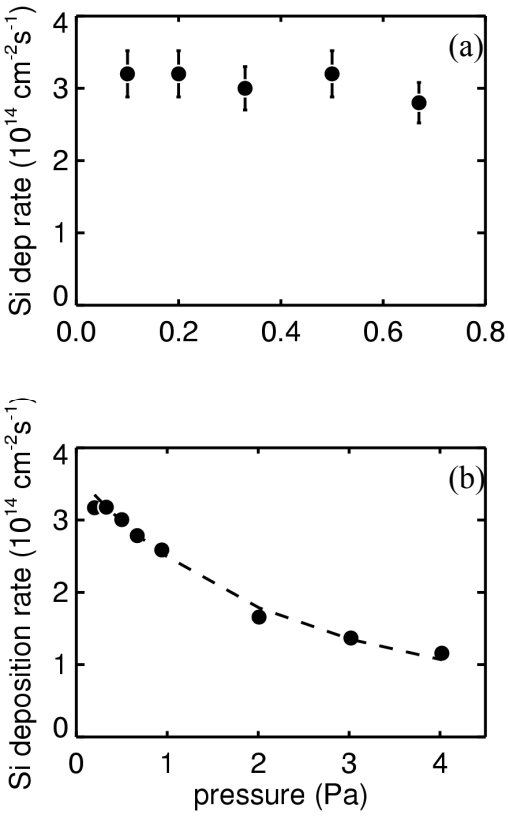

Figure 4.20 Silicon growth rate as a function of the total pressure. The absorbed power amounts to 100 W, no oxygen. The symbols represent the measured values. The dashed line represents the fitted Keller-Simmons formula.

Recently, a modification of the Keller Simmons formula was proposed, which takes the temperature of the growing film into account, but ignores thermal gradients in the deposition system [17]. This analysis shows that the empirical parameter $p_0 L_0$ is related to the temperature T_s of the growing film and the integral cross-section σ for elastic scattering of a sputtered atom from a neutral argon atom:

$$P_0 L_0 = \frac{k_B T}{\sigma} \qquad (4.8)$$

A reduced geometrical cross-section, $\sigma = 0.6\ \sigma_{geom}$, is taken to account for the relative momentum of the sputtered particles.

A fit of the experimental data in figure 4.20 with equations (4.7) and (4.8) yields a value for the temperature of the deposition surface below 400 K. This value is realistic and rather low compared to the deposition of metals like vanadium and tungsten [16] and it is therefore concluded that thermal gradients can be neglected in our system [17]. Thus, the (modified) Keller-Simmons formalism appears to describe the pressure dependence of reactive magnetron sputtering of silicon well [18].

4.5 Relative extent of argon ion bombardment as function of the applied power

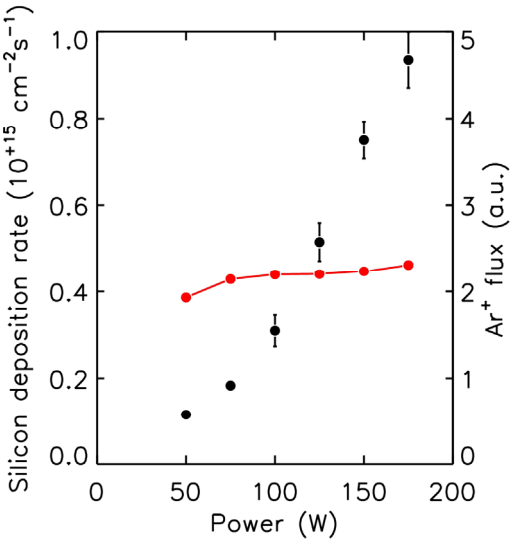

Figure 4.21 The growth rate and Ar^+ ion bombardment as a function of power, at 0.35 Pa

In Fig. 4.21 a comparison is made between the deposition rate of silicon and the argon ion bombardment. The silicon deposition rate is determined using *in-situ* ERD. The argon ion bombardment, i.e. the number of Ar ions that hit the deposition surface per unit of time, is measured using the mass spectrometer. An increase, as a function of power, is observed for both. However, the increase in the amount of deposited silicon is much larger than the increase in the amount of argon ions bombarding the deposition surface. As a consequence we conclude that the relative amount of ions bombarding the surface per deposited particle is decreasing with increasing power. This is depicted in Fig. 4.22. The plasma potential, defined as the ion energy at which most ions are measured is shown as well. Clearly, there is a decrease in the amount of ions per deposited silicon atom bombarding the deposition surface, but the ions carry a higher amount of energy per ion. However, the increase of the amount of energy is only small compared to the decrease in the number of ions bombarding the deposition surface. The amount of energy deposited per deposited particle by means of the ion bombardment does therefore decrease. As a result it is expected that the extent of modification in the growing film caused by ion impingement diminishes for increasing power supplied to the plasma.

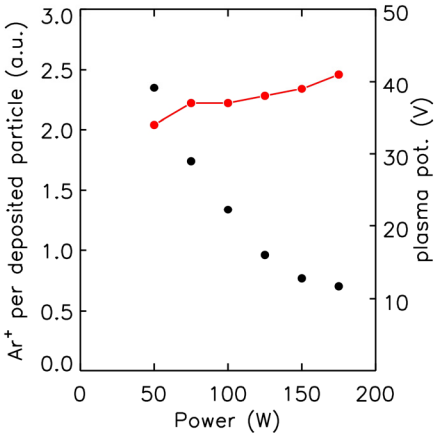

Figure 4.22 The relative ion bombardment (black) and plasma potential (red) of the bombarding ions as a function of the power, at 0.35 Pa.

4.6 Spinodal decomposition in deposited films

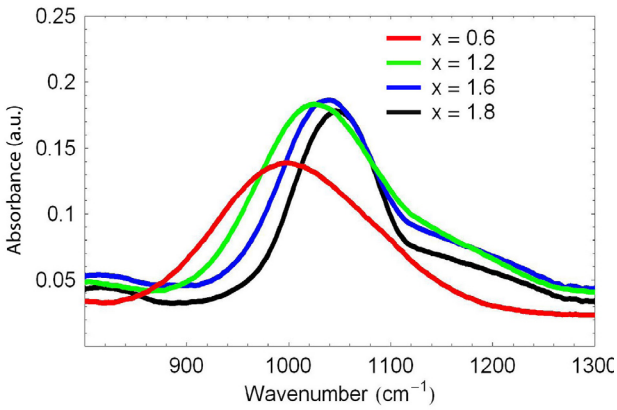

Figure 4.23 The absorption peak of the Si-O-Si stretching vibration for different x-values, deposited at 100 W.

Infrared absorption transmission measurements (IR) are made for samples deposited on silicon wafers. The IR spectrum is measured from 500 cm^{-1} to 8000 cm^{-1} with a resolution of 4 cm^{-1}. The most interesting part of the spectrum is the region around the Si-O-Si stretching mode which, in bulk SiO_2, is at 1076 cm^{-1}.
In Fig. 4.23 several absorption spectra are shown for samples deposited at 100 W. The total thickness of the examined films is approximately 120 nm.
Obviously the position and shape of the main IR peak changes as a function of the x-value, is as it would be expected: the peak position has been found to shift from about 950 cm-1 for an

isolated Si-O-Si bridge in a-Si, up to higher wavenumbers with increasing x-value [19], or considered more locally, with an increasing oxygen backbonding of a Si-O-Si bridge. Moreover, the higher x-value films develop a shoulder at higher frequencies, indicative for the presence of SiO_2 regions [20]. Because of this complicating feature a fit of the peak is omitted. The frequency with the highest absorption intensity is taken as the peak position, and is considered to be a probe for the maximum in the local, bound oxygen concentration distribution.

To investigate the importance of the relative ion bombardment for the deposition process we deposited samples with different powers, 100 W and 250 W. For these series of samples with varying x the peak position is determined by taking the maximum of the IR absorption signal. This is plotted in Fig. 4.24.

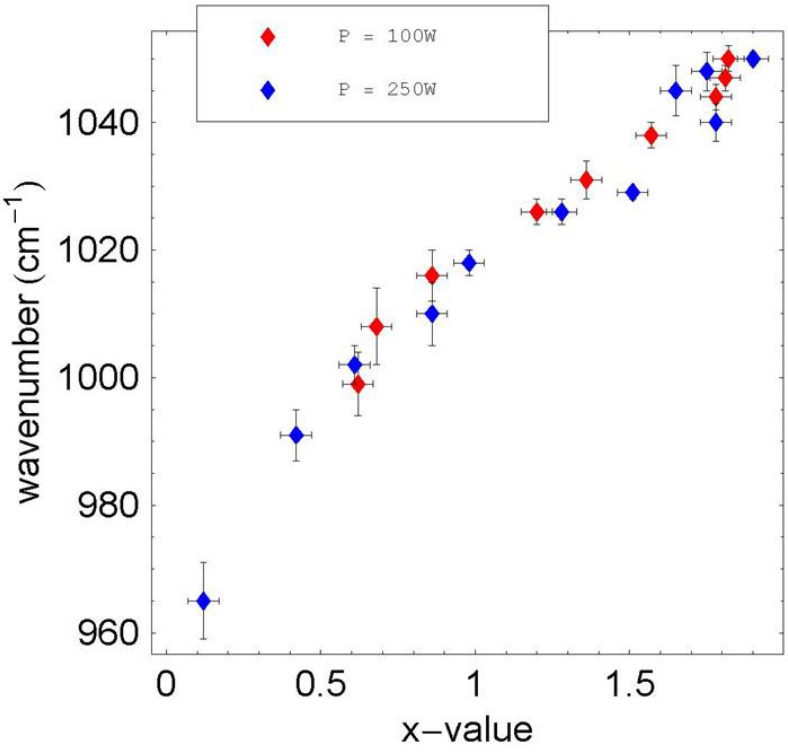

Figure 4.24 Peak position of the Si-O-Si stretching mode vs. the x-value of the film for films deposited at 100 and 250 W.

There appears to be no significant difference between the samples deposited at 100 W and 250 W, in the range between x = 0.6 and x = 2. So the conclusion is that in this range of power the nano-structure of the material is not significant influenced by the ion bombardment during the deposition.

4.7 Summary

From the experiments described in this chapter the following picture of the RF magnetron plasma sputter deposition process of SiO_x in our system emerges:
The plasma can be divided roughly in two regions. The boundary of the two regions is given by the surface in the plasma where the plasma potential has a maximum, and is about 2 cm from the cathode. For comparison, the distance between the cathode and the surface where the deposition takes place and is investigated, amounts to 8.5 cm.
The region closest to the sputter cathode is strongly non-uniform parallel to the plane of the silicon cathode surface, due to the presence of the magnetic field. This non-uniformity causes the sputtering to take place mainly in a ring-shaped area, the so-called racetrack. Ions in this region are accelerated towards the racetrack, and bombard the cathode with an energy determined by the sum of the absolute values of the plasma potential and the cathode potential, which results in our system to about 200-300 eV. An increase in the power injected into the plasma increases the sputtering rate, because of the increase in the ion density and the ion kinetic energy. A variation of the Ar pressure does not result in a variation of the sputtering rate.
In a zeroth approximation the position of the boundary between the two regions mentioned above does not depend on the injected power or the pressure. The region closest to the investigated growth surface is much more laterally uniform, and is called, somewhat arbitrarily, the plasma afterglow. This region is characterized by a slowly decreasing ion density, a more or less constant electron temperature and a plasma potential, which decreases about 4-6 eV from the maximum of 30-50 eV to the edge of the anode sheath. The growth surface is grounded and therefore ions created in this region are accelerated towards the growth surface with an energy of 30-50 eV. There are plenty of details observed in the mass and energy spectra of the species impinging on the growth surface. These details reflect the kind of atoms and molecules present in the plasma due to the gas input and the sputtering, the position in the afterglow where the ions are created and which mechanism is responsible for the ion creation. However, far the most ions bombarding the growth surface are Ar^+ ions. The flux of these ions towards the growth surface has been estimated to be in the order of $\sim 10^{16}$ /cm^2 at rather low pressures, where interactions of the ions with gas atoms on their way to the growth surface can be neglected. The ion flux on the growth surface does not strongly depend on the injected plasma power, in contrast to the sputtering rate. The result is that the extent of ion bombardment per deposited atom decreases with increasing plasma power, because of the more than linear increase of the growth rate, which amounts to $10^{14} - 10^{15}$ Si atoms/cm^2 in our power range.
The possibility to vary the extent of ion bombardment per deposited atom in a controlled manner enabled the investigation of the role that ion bombardment possibly could play in the formation of the internal nanostructure of the grown SiO_x. This is considered interesting because of the tendency of this material to separate in Si and SiO_2 phases, the extent of which is expected to have a strong influence on the electrical and other properties. It appeared that the average number of oxygen atoms which are bonded to the silicon atoms in a Si-O-Si bridge at a certain x-value, does not measurably depend on the power injected in the plasma during growth and therefore does not measurably depend on the extent of ion bombardment during deposition.

4.8 References

[1] A. Palmero, E.D. van Hattum, H. Rudolph and F.H.P.M. Habraken, submitted

[2] K.Wasa and Shigeru Hayakawa, editors, *Handbook of sputter deposition technology*, Noyes Publications, 1991, pp. 117

[3] M.Spolaore, V. Antoni, M. Bagatin, A. Buffa, R. Cavazzana, D.Desideri, E. Martines, N. Pomaro, G. Serianni and L. Tramontin, Surf. Coat. Technol. **116** (1999), 1083.

[4] D.Desideri and G. Serianni, Rev. Sci. Instrum. **69** (1998), 2354.

[5] M. Bagatin, D. Desideri, E. Martines, G. Manduchi, G. Serianni and V. Antoni, Rev. Sci. Instrum. **68** (1997), 365.

[6] A.Grill, *Cold plasma in materials fabrication*, IEEE press 1993, pp.14

[7] A. Palmero, E.D. van Hattum, H. Rudolph and F.H.P.M. Habraken, accepted for publication in EPJ. D

[8] K.Wasa and Shigeru Hayakawa, editors, *Handbook of sputter deposition technology*, Noyes Publications, 1991, pp. 57

[9] D.Marton, Appl. Surf. Sci. **5** (1980), 65.

[10] E. Franke, H. Neumann, M. Zeuner, W. Frank and F. Bigl, Surf. Coat. Technol. **97** (1997), 90.

[11] P.C.Zalm, J. Appl. Phys. **54** (1993), 2660.

[12] K.Wittmaack, Phys. Rev. B **68** (2003), 235211.

[13] M.Zeuner, H. Neumann, J. Zalman, D. Slavínská and H. Biederman, Vacuum **51** (1998), 417.

[14] N.Ray, P.Rajasekar and S.D.Dey, Surf. Sci. **322** (1995), 90.

[15] J.H. Keller and R.G. Simmons, IBM J. Res. Develop. **23** (1979), 24.

[16] T.P. Drüsedau, Surf. Coat. Technol. **174-175** (2003), 470.

[17] A.Palmero, H. Rudolph and F.H.P.M. Habraken, Appl. Phys. Lett. **89** (2006), 211501.

[18] A. Bogaerts and R. Gijbels, J. Anal. At. Spectrom. **19** (2004), 1206.

[19] P.G. Pai, S.S. Chao, Y. Takagi, and G. Lucovsky, J. Vac. Sci. Technol. A **4** (1986), 689.

[20] C.T. Kirk, Phys. Rev. B **38** (1988), 1255.

5

Oxygen incorporation during deposition

5.1 Introduction

In this chapter we describe a detailed investigation of the growth of SiO_x films in a reactive RF magnetron sputter deposition process. The focus is on the oxygen incorporation on the growth surface and on the sputter target. In our unbalanced magnetron RF sputter deposition process we apply a silicon cathode as source of silicon and gaseous O_2 as source of oxygen, with argon as the sputter gas. We varied the power injected into the plasma and the O_2 flow into the system. The growth rates of the distinct elements on the deposition surface are determined by *in-situ* elastic recoil detection [1] and ex-situ Rutherford backscattering spectrometry. An energy resolving mass spectrometer is used to measure the amount and energy of the various ions impinging on the growth surface during the deposition. A model concerning the oxygen coverage on the cathode erosion area, the so-called race track, during sputtering is discussed. The various possible contributions to the oxygen incorporation on the growth surface have been distinguished and the magnitude of their contribution is estimated, including that of molecular SiO.

5.2 Material growth rate

5.2.1 Growth rate of silicon

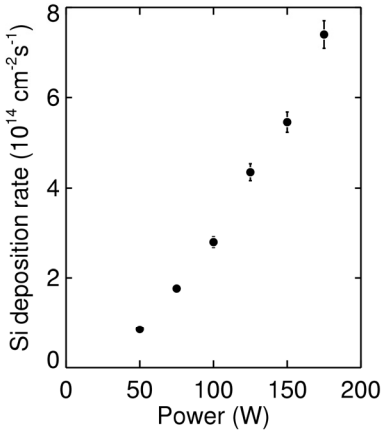

Figure 5.1 Silicon deposition rate vs power at 0.66 Pa., without oxygen in the plasma.

The deposition rate of silicon has been described in chapter 4. The deposition rate depends hardly on the argon pressure at low pressure, and decreases at higher pressure, due to collisions of the sputtered atoms with argon atoms (see chapter 4).
The silicon deposition rate as a function of the injected power is (again) depicted in Fig. 5.1. When oxygen is added to the plasma, this oxidizes (a part of) the surface which is deposited. The amount of oxygen ending up in the film is dependent on various parameters most important are the ratios of the fluxes of oxygen and silicon species arriving at the surface and their respective sticking probabilities.
SiO_2 is considered the film composition with the highest amount of oxygen in the deposited film, although exotic configurations i.e. Si-O-O-O-Si are also considered in literature [2]. If only a small amount of oxygen is introduced into the plasma we expect that complete oxidation of the silicon cannot take place and we can therefore deposit films with intermediate x-values. Although the amount of oxygen in the deposition vessel is mainly determined by adjustable parameters such as the oxygen flow into the system and the pumping speed, we actually have to consider the partial pressure of the reactive species being present in the plasma [3], since gettering of oxygen on the walls of the system, on which silicon is being deposited, plays a less controlled role. Oxidation of surfaces is actually removing part of the oxygen from the gas phase, effectively reducing the oxygen partial pressure. Therefore it is possible to think of the growing film as an oxygen sink, or oxygen pump. Shortly stated, we find that there is a difference in the effective observed pumping speed between a reactive species and the inert buffer gas. Therefore, not the adjustable input flow, but instead the partial pressure accurately describes the number of reactive particles that collide with the deposition surface per unit of time (see also chapter 3).

5.2.2 Growth rate of oxygen

The oxygen growth rate r_O, i.e. the increase in the number of oxygen atoms per cm^2 per second on the growth surface can be determined from the obtained x-value and the silicon deposition rate r_{Si}. The following relation holds:

$$x = \frac{r_o}{r_{Si}} \tag{5.1}$$

Thus the x-value can be determined from the independent measurements of the silicon and oxygen deposition rates. The two procedures give the same result [1].

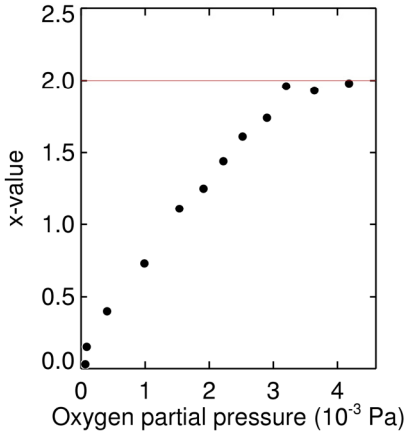

Figure 5.2 The x-value versus the oxygen partial pressure at a power of 175 W and a total pressure of 0.66 Pa. The error in the oxygen partial pressure is estimated at $\pm 2.10^{-4}$ Pa.

In Fig.5.2 the x-value is depicted for a plasma of 175 W for a series of films as a function of the oxygen partial pressure and argon pressure of 0.66 Pa, the statistical error from the analysis is below 0.5 %. A more or less linear relationship between the x-value of the deposited films and the oxygen partial pressure is found. Moreover, in figure 5.3 the silicon deposition rate found is shown for the different films, plotted as function of the oxygen partial pressure for a power of 175 W, up to an oxygen partial pressure value where SiO_2 is being deposited. The input flow of oxygen is on the order of 1% of that of argon, and so the total pressure is hardly influenced by the introduction of oxygen into the system. From Fig. 5.3 we can conclude that the silicon deposition rate is not influenced by the introduction of oxygen until we have reached a pressure where we deposit SiO_2.

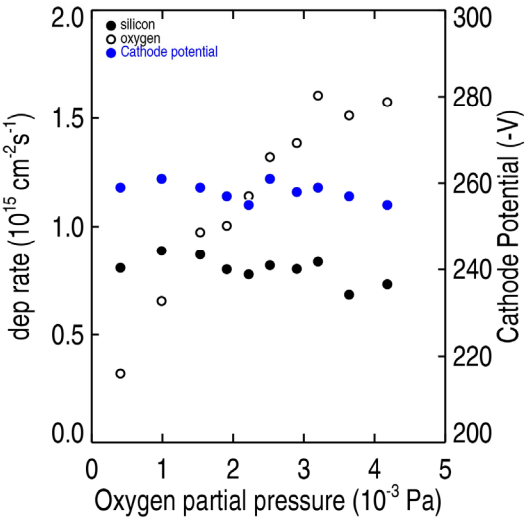

Figure 5.3 Silicon deposition rate (closed) and oxygen deposition rate (open) as well as the cathode potential (blue). The data concern the same measurements as presented in Fig. 5.2.

Since the silicon growth rate is independent of the oxygen partial pressure and therefore independent of the x-value, it is consistent that we observe that the oxygen growth rate also increases linearly with the oxygen partial pressure almost up to the pressure where SiO_2 grows (Fig. 5.3). The deviation from linearity occurs at lower oxygen partial pressure at lower power, due to the smaller silicon growth rate at the lower power, whereas the oxygen growth rate hardly depends on the RF input power (see Fig.5.4a).
The oxygen growth rate does hardly, if at all, depend on the injected RF power, as is shown by the *in-situ real-time* measurements, as presented in Fig. 5.4b.
In contrast, the oxygen growth rate appears to depend on the growing film temperature, whereas the silicon growth rate does not, see section 5.3.

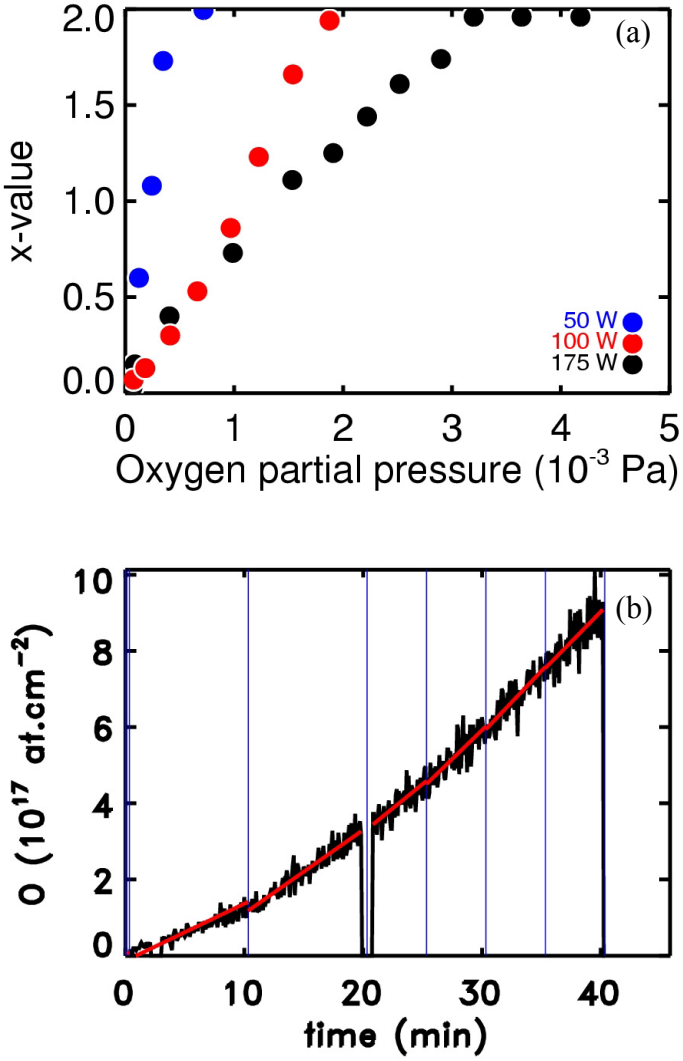

Figure 5.4 (a) The x-value of deposited films at given powers as a function of the oxygen partial pressure. For low power the deposition of SiO_2 takes place at lower oxygen partial pressure. (b) *Real-time* ERD measurement (see chapter 3) of the amount of oxygen present in the growing layer, with changing the power at the moments indicated by the blue lines from 50 W up to 175 W, in steps of 25 W. The oxygen partial pressure amounts to $6 \cdot 10^{-4}$ Pa and the total pressure is the 0.66 Pa. The (generally constant) slope gives the oxygen deposition rate. The deposition at 50 W exhibits a relatively low O deposition rate because at this power the Si growth rate is so low that material with x near 2 is grown. The interruption in the curve is due to a spark in the accelerator.

The effective O_2 reaction probability α_{eff} on the growing film is defined as the overall probability for an O_2 molecule, impinging on the growth surface, to decompose, in which process 2 oxygen atoms are incorporated, assuming that this is the only process contributing to oxygen incorporation.

$$\alpha_{eff} = \frac{1}{2}\frac{r_O}{\Phi_{O_2}} \tag{5.2}$$

In Eq. 5.2 Φ_{O_2} represents the flux of oxygen molecules impinging on the surface per cm^2 per second. This flux at given temperature, T, and oxygen partial pressure p_{O_2} is given in Eq. 5.3, m is the mass of a single particle.

$$\Phi_{O_2} = \frac{p_{O_2}}{\sqrt{2\pi\, m k_B T}} \tag{5.3}$$

With this definition the preliminary conclusion must be that the O_2 reaction probability is constant as a function of the oxygen partial pressure, i.e., it does not depend on the x-value for nearly the entire range $0 < x \leq 2$.

If we now assume that decomposition of gaseous O_2 molecules on the surface is the only process which contributes to the oxygen incorporation, we could calculate a real O_2 reaction probability from the data in figure 5.2. The thus obtained value for the reaction probability amounts to 0.16±0.02, depending only slightly on the power injected into the plasma.

5.3 Temperature dependence in the growth rate of oxygen

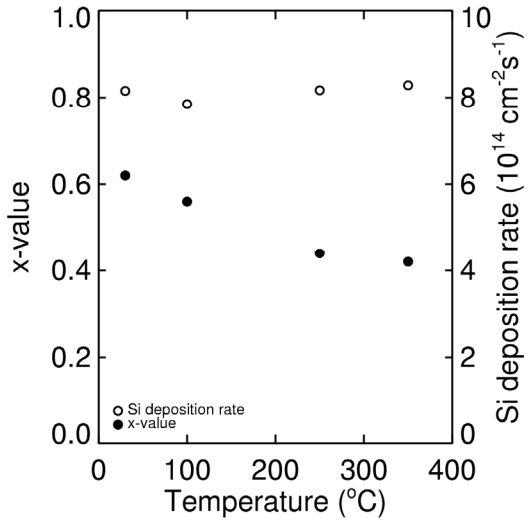

Figure 5.5 The deposition rate of silicon (open) and the x-value of films (closed) deposited with an oxygen partial pressure of $6 \cdot 10^{-4}$ Pa, a power of 175 W and total pressure of 0.66 Pa. Error in the x-value due to the analysis is below 0.5%, the error in the temperature is estimated at 40 °C.

It appears that if the substrate is at an increased temperature during deposition, the oxygen growth rate, and therefore the O_2 reaction probability is significantly lower than if no additional heating of the substrate is applied, see figure 5.5. The silicon deposition rate appears independent of the substrate temperature. Consequently, the x-value is found to decrease at higher temperatures. It is important to note that the temperature is measured behind the sample-holder; the temperature of the front side of the substrate lags behind, in time. It is not known how much the temperature difference between the front and backside of the substrate actually is. The sample is heated by two standard filaments from a Halogen light source of which the wires are exposed to the reactive gas. Thus we expect the heater to have a limited life time. The error in the temperature for the data given in Fig. 5.5 is estimated to be 40 °C.

A priori we do not know if the decomposition of impinging O_2 molecules is the relevant process for the oxygen incorporation. In fact this information cannot be deduced from the measurements presented so far. There could be other sources for oxygen incorporation in the growing film:
-atomic oxygen originating from dissociation of O_2 in the plasma region
-atomic oxygen, originating from the sputter cathode
-other oxygen containing molecular species like SiO and SiO_2, originating from the plasma or from the sputter cathode.
To address this matter we refer to the measurement of the ion fluxes in the plane of the growth surface, as measured with the energy resolved mass spectrometer. The relevant information is not straightforwardly determined from the ion fluxes, since the ion flux is assumed to be only a fraction of the flux of neutral particles, which is the relevant quantity, and it is not trivial to calculate or deduce the neutral flux from the ion flux.

5.4 Mass spectrometer measurements

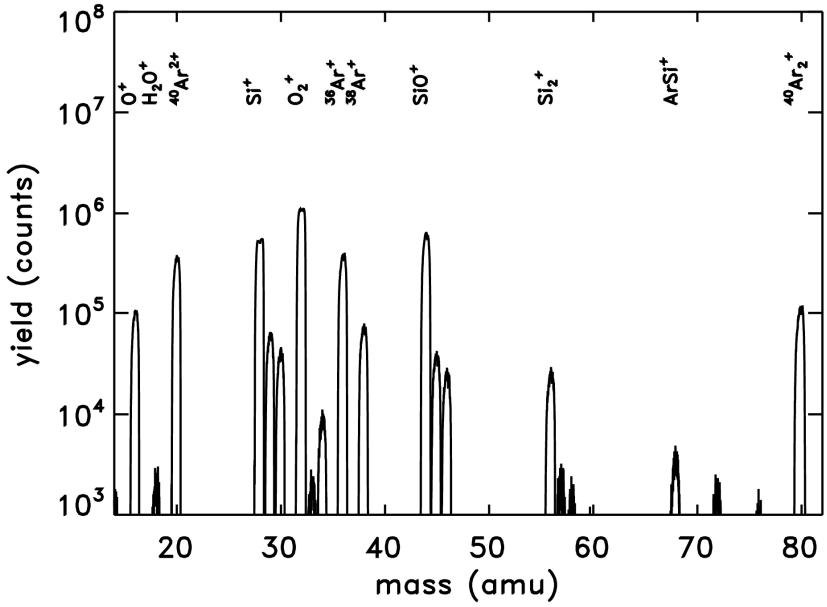

Figure 5.6 The mass spectrum of positive ions bombarding the deposition surface in a plasma with a power of 200 W, total pressure of 0.66 Pa and an oxygen partial pressure of $2.4 \cdot 10^{-3}$ Pa. The signal at m/z = 40, the signal of the main argon isotope, is omitted to avoid detector damage.

A mass-spectrum of positive ions, impinging on the growth surface with a kinetic energy of 36.5 eV, the plasma potential, is depicted in Fig. 5.6. The main ion species involved in the deposition process are, besides argon, Si^+, O^+ O_2^+ and SiO^+. The other species attributed to the distinct mass/charge signals are indicated in Fig.5.6 as well.

Figure 5.7 shows the ion flux in the mass spectrometer for various ions and for several values of the RF power (100, 150 and 200 W) as a function of the oxygen partial pressure. The total pressure amounts to 0.66 Pa. As expected we note a strong increase in the yield of O_2^+ ions with an increase of the oxygen partial pressure, but the ion yield appears relatively independent of the power input. The Si^+ ion yield remains constant for low oxygen partial pressure for higher levels of the power input. At a certain partial pressure, whose value depends on the RF power, the Si^+ yield decreases.
The apparent large amount of SiO^+ ions we find warrants a separate discussion of the role of this species in the growth process.
Previously, in section 4.3.5 clusters of silicon particles have been discussed. Although not visible in Fig. 5.6, because of the low SiO_2 yield at that particular setting of the oxygen partial pressure, we also find a contribution at m/z = 60 for higher oxygen partial pressure, which we ascribe to SiO_2^+. As we see in figure 5.7 the amount of SiO_2^+ increases strongly with increasing oxygen pressure, but it remains always low and we will therefore not discuss it further.

In Fig. 5.7 the ion intensity is plotted on a logarithmic scale. For reactive species we find on this scale that at low oxygen partial pressures the amount of ions is independent on the power injected into the plasma. As can be expected the amount of O^+, $O2^+$ and SiO^+ ions increase with increasing oxygen partial pressure. From a comparison between the cathode potential and number of Si^+ ions (Fig. 5.7b) we find that both show no decrease if the pressure remains below $5 \cdot 10^{-3}$ Pa. Hence, below this pressure there is no significant influence from the oxygen on the plasma parameters.
In figure 5.7c a strong increase of the SiO^+ ion yield in the mass spectrometer is noted with increasing O_2 partial pressure in the low partial pressure region. In this region the yield of these ions hardly depends on the RF power. The attribution of these signals to carbon dioxide can be excluded because of the ratios of m/z = 44 and 45 which corresponds to the ^{28}Si and ^{29}Si isotope abundance ratio. Strikingly, for values of the O_2 partial pressure at which near-stoichiometric SiO_2 films are grown, the SiO^+ yield has the same order of magnitude as the Si^+ ion yield. Whereas at higher oxygen partial pressure there is a clear difference between the amounts of SiO^+ ions for the different powers, at low oxygen partial pressure the number of ions is independent of the applied power. Only the oxygen partial pressure is important for the number of SiO^+ ions that reach the deposition surface.

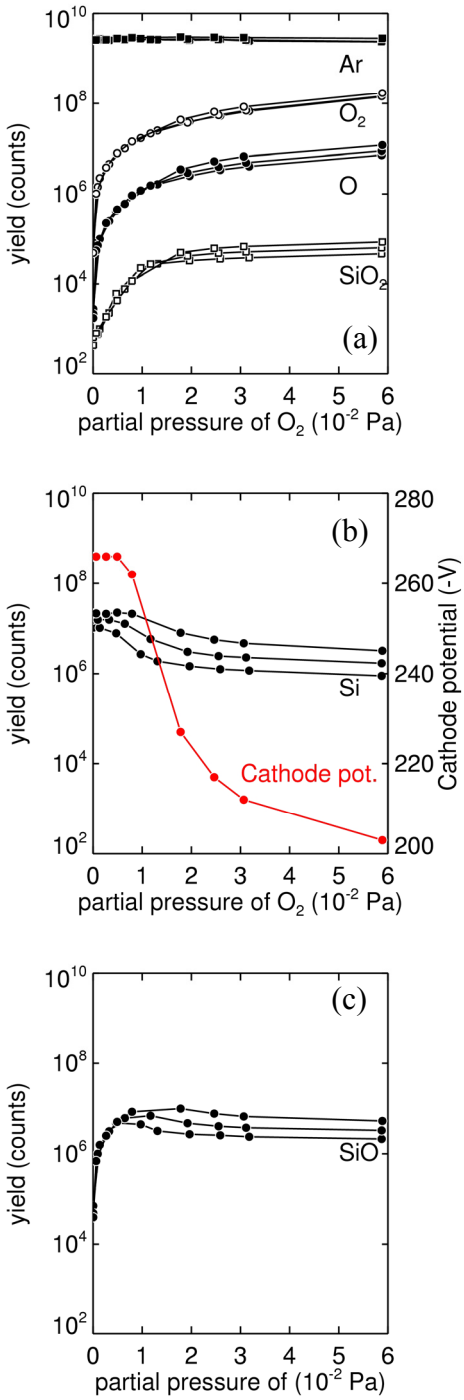

Figure 5.7 The amount of ions of several ion species as a function of the oxygen partial pressure present in the system. The total pressure is 0.66 Pa and the applied powers are 100, 150 and 200 W. (a) Ar^+, O^+, O_2^+ and SiO_2^+, (b) Si^+ and cathode potential at 200 W, (c) SiO^+ ions. The error in the oxygen partial pressure is estimated at 10 %.

5.5 Ion yield dependence on the vertical position with respect to the plasma

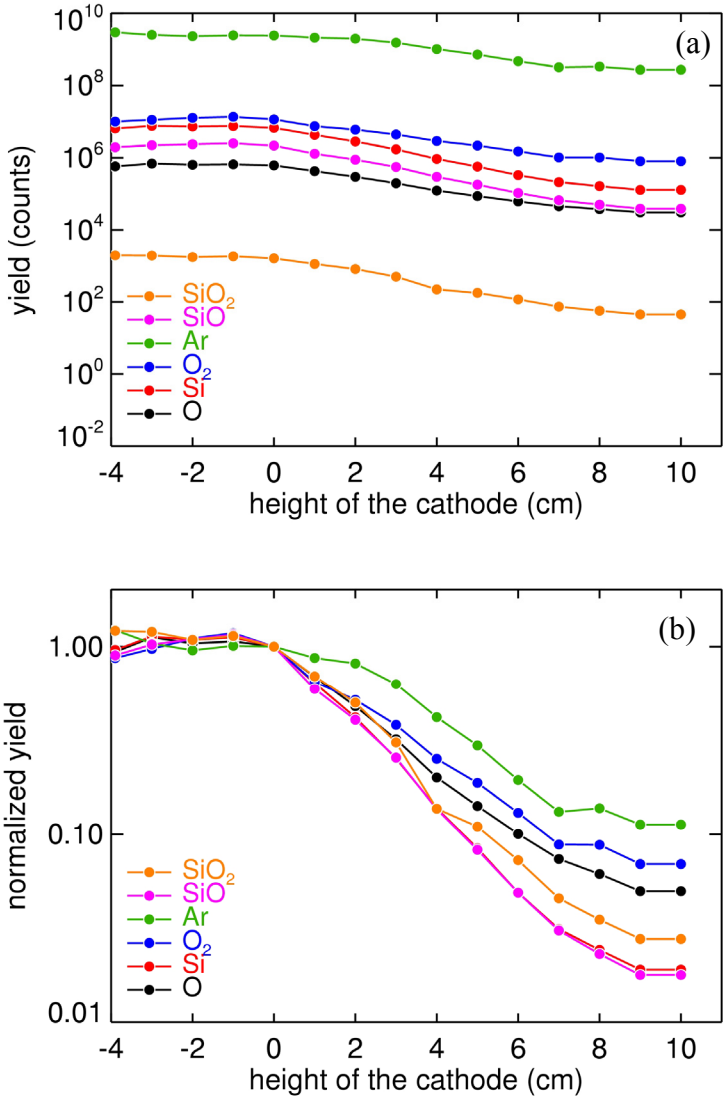

Figure 5.8. Positive ions detected as a function of the height of the cathode. Plots are (a) logarithmically, (b) and normalized to the position in front of the race track.

As expected, figure 5.7a also shows an increase of the O^+ ion yield with increasing oxygen partial pressure. The O^+ ions detected may have two origins: they could originate from sputtering of the oxygen covered cathode and ionised in the plasma, and they could originate from dissociation and ionisation of gas phase molecular oxygen.

Presuming that the measured flux of the ions is indicative for the impingement of the much larger amount of neutrals, it is relevant to discuss the possible role of the SiO molecules and of atomic oxygen in the deposition.

To get experimental information about the origin of the SiO^+ and of the O^+ ion yield, and thus about the O atoms and SiO molecules in the plasma, we make use of the difference in

velocity distribution of sputtered and of gas phase species. Figure 5.8a gives the measured ion flux for several relevant species as a function of the height of the cathode as compared to the mass spectrometer aperture. For small values of the height for all species the ion flux remains constant, for larger values of the height the flux decreases for all species. This behaviour can qualitatively be explained by considering the spatially resolved plasma characteristics [4]. However, the behaviour is not the same for all species. Figure 5.8b shows the behaviour of the different species normalised to the ion yield at zero target height (race track in front of the opening of the mass spectrometer). These measurements are for a total pressure of 0.2 Pa, where the collisions of the sputtered particles with the plasma gas atoms (predominantly argon) can be neglected thereby preserving as much as possible the original velocity distribution. From these measurements we use the observation that the Si^+ and the SiO^+ fluxes behave identically. The O^+ and the O_2^+ fluxes exhibit a mutual similar behaviour, which is however different from that of SiO^+ and Si^+. From this we conclude that SiO^+ ions have the same origin as the detected Si^+ ions, namely from the sputter cathode. Similarly, we conclude that the O^+ yield predominantly originates from the gas phase where O_2^+ ions are assumed to originate from. Since the height dependence of the O^+ and O_2^+ ion yields is not completely the same, a small contribution of sputtered atoms from the cathode to the O^+ signal can not completely be ruled out.

Supporting evidence for the sputtering of SiO from oxidised silicon surfaces is the observation that SiO is found to be emitted as a result of ion bombardment of a silicon surface, interacting with gaseous O_2 [5] and that SiO is the major species desorbing from SiO_2 heated to high temperature (above 600°C) [6].

It is evident that in addition to the detected SiO^+ ions also a large number of SiO neutrals from the sputter cathode impinge on the growth surface. However, in absence of the knowledge of the SiO ionisation probability in comparison to that of Si we do not know yet the magnitude of the flux of SiO neutrals, in comparison to that of the Si neutrals. In the following section we attempt to estimate the flux of SiO on the growth surface. The important aspect of the SiO impingement lies of course in the fact that SiO also carries a silicon atom and as such potentially contributes to both the oxygen and the silicon growth rate. We therefore compare the several ion yields with the growth rates of the distinct elements, thereby assuming that the silicon growth rate is indicative for the silicon neutral flux on the growth surface.

5.6 The SiO contribution to the deposited material

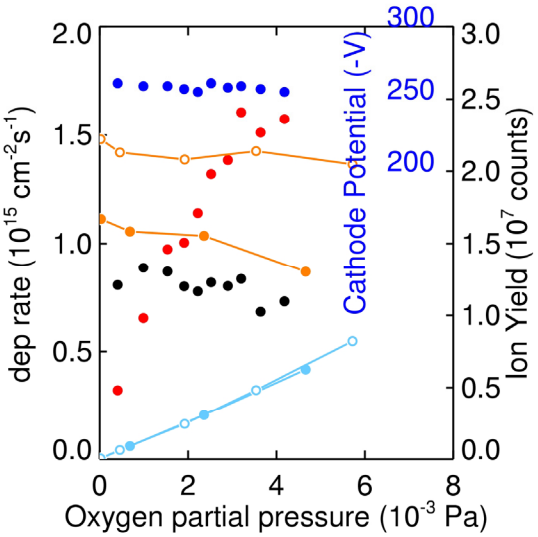

Figure 5.9 Silicon deposition rate (black), oxygen deposition rate (red) and cathode potential (blue) for the samples deposited at 175 W depicted vs. the oxygen partial pressure. Also Si^+ (orange, 150 (closed) and 200 W (open symbols)) and SiO^+ (light blue) ions at 150 W (closed) and 200 W (open symbols) bombarding the surface.

Figure 5.9 shows the Si^+ and SiO^+ ion yields for 2 values of the power as a function of the oxygen partial pressure together with the silicon deposition rate, the oxygen deposition rate and the cathode potential. For a wide range of oxygen partial pressure, or stated differently, for the entire range of x-values $0 < x \leq 2$, we find a constant silicon deposition rate, a constant Si^+ flux, and an increasing and not negligible yield of SiO^+ ions. Since the data are for the same total pressure, the transport of silicon neutrals is expected not to depend on the oxygen partial pressure; therefore the yield of Si in the sputtering process seems independent of the oxygen partial pressure within the range of figure 5.9.
The apparent O_2 reaction probability also appears to be independent of the x-value for a wide range, as already concluded before. On the other hand, assuming that the SiO^+ flux is proportional to the sputter yield of SiO, with the same proportionality constant for all x-values the SiO neutrals flux on the growth surface increases with increasing oxygen partial pressure. The observed constant values for the silicon deposition rate and for the oxygen reaction probability suggest that SiO does not measurably contribute to the growth of silicon and oxygen incorporation in the film, despite the appreciable value of the SiO^+ flux.
In principle, the explanation for this intriguing set of observations can be one or more of the following explanations:
- the ionisation probability of SiO has a high value such that the SiO neutrals flux can be neglected compared to both the Si and reacting O_2 flux.
- the sticking probability of SiO is small compared to that of Si and O_2 or other oxidizing species.

- the Si neutral flux or sticking probability and the O_2 reaction probability decrease with increasing x-value, but this decrease is compensated by the increase in SiO neutral flux.
In order to estimate an upper limit for the role SiO is playing in the deposition, we now assume that the removal of oxygen from the cathode surface proceeds solely through the sputtering of SiO. We furthermore assume that the reaction of molecular oxygen with the cathode silicon surface proceeds in the same manner as on the anode, i.e., molecular oxygen is supposed to react with the same effective reaction probability with the cathode surface (of 0.16 when the cathode surface would be at room temperature), independent of the coverage for a wide range of values for the oxygen coverage. In the following we apply the Berg model for reactive sputtering [7] in our situation.
We estimate the surface area of the ring shaped region where the sputtering predominantly takes place on the cathode (the erosion area or "racetrack") to amount to a, in our case $a \approx 30$ cm^2. From the measurements in which we varied the height of the cathode we estimate the projected surface area A, where silicon, and also SiO, is being deposited and where molecular oxygen reacts with this deposited silicon with the same value (of 0.16) for the reaction probability, to amount to at least 300 cm^2 (see Fig.4.10).
In steady-state, per unit of time and per unit of surface area on the cathode, oxygen, assumingly in the form of SiO, is sputtered in an amount which is equal to the amount which is adsorbed. This amount is distributed over a $A/a \approx 10$ times larger surface area (where additionally per unit area and unit time the same amount is adsorbed as on the cathode). This estimation leads to the conclusion that in our system at most 10% of the oxygen being incorporated in the growing film is due to oxygen containing species originating from the cathode, even if the incorporation probability of this species would be 1. This is an upper limit since we have assumed that all oxygen from the cathode in the racetrack is removed through the SiO channel.
Note that the result of this reasoning is independent of the value of the O_2 reaction probability, as long as its value is more or less equal for the anode and the cathode, or whether SiO or O is the main oxygen containing sputtered species.

To our knowledge, the value for the sticking probability of SiO is not known, but it most probably has an appreciable value in view of the successful attempts to deposit silicon sub-oxides from a SiO sintered target [8] or from a high temperature oxidised sputter target, from which SiO is assumed to evaporate resulting in a significant increase of the deposition rate [9]. It must be noted that the data and the interpretation thereof in figure 5.8b only make sense if the sticking probability of SiO is comparable to that of Si. Smaller values of the SiO sticking probability immediately result in an even lower contribution of SiO to the growth on the anode.

Summarizing, it is inferred that SiO sputtering does not significantly contribute to the silicon and oxygen growth rate in the sputter deposition of SiO_x, if the cathode operates in the metallic mode. The same arguments can be used to show that sputtered oxygen atoms do not contribute significantly to the deposition, if they are emitted in the sputtering process anyhow. The above analysis shows that the contribution of oxygen, sputtered from the cathode, to the growth of the material depends on the geometry of the deposition system, to be more specific, on the ratio of the erosion area on the cathode to the area of the deposition region.

5.7 The contribution of atomic oxygen to oxygen incorporation

We now address the question how large the contribution of atomic oxygen to the film growth could be. In contrast to the situation with SiO, the value of the electron impact ionisation cross-section for atomic and molecular oxygen is well-known [10-13]. The ratio of the electron impact ionisation cross-section of O and O_2 for an electron temperature of 3 eV, as in our plasma, amounts to 0.5. The ratio of the experimentally observed O^+ and O_2^+ ion fluxes amounts to about 0.05, see figure 5.7a. This ratio depends only slightly on the RF input power. Every O_2 molecule carries two O atoms. So the number of oxygen atoms impinging on the surface as atomic oxygen amounts to about 5% of the number of oxygen atoms arriving at the surface in the form of O_2. The sticking probability of atomic O on silicon is generally assumed to be 1 [14].
For the oxygen deposition rate $dN_{O_{film}}/dt$ on the growing film surface, where we have neglected the contribution from SiO:

$$\frac{dN_{O_{film}}}{dt} = 2\alpha_{eff}\Phi_{O_2} = 2\alpha\Phi_{O_2} + 0.05\Phi_{O_2} \qquad (5.4)$$

Here α denotes the O_2 decomposition probability at the surface.
Above we have deduced that:
$\alpha_{eff} = 0.16$, and therefore we calculate that $\alpha = 0.14$. We also deduce that atomic oxygen contributes, at room temperature, no more than about 16 % to the total oxygen growth rate.
We conclude that our analysis above, in which we have assumed that the oxygen growth is mainly due to molecular oxygen, is more or less correct. The value for the O_2 decomposition probability, as deduced from Eq. 5.4 amounts to 0.14±0.02.
This value of for the decomposition probability of O_2 agrees reasonably well with literature values for the sticking probability of O_2 on silicon [15], although also much smaller values have been reported for smooth, well annealed single crystal surfaces [16]. Here we have to take into account that the growing film is continuously bombarded with low-energy electrons and Ar^+ ions, which has been shown to enhance the effective reaction probability [15,17,18]. Also, the surface of the growing film is assumed to be rough on an atomic scale, giving rise to an increased sticking probability as well [19].

5.8 Summary of the oxygen incorporation in the growing films

Summarising, in our system the oxygen incorporation in the growing SiO_x films is for the majority due to molecular oxygen, about 16% is due to atomic oxygen and for a smaller, thus far unknown, fraction to SiO. These conclusions are for a substrate which is not additionally heated. Under the assumption that the sticking probability of atomic oxygen hardly depends on the surface temperature, it is also concluded that the contribution of atomic oxygen increases with increasing substrate temperature and therefore becomes more significant at higher temperatures.

The observations that the oxygen reaction probability is more or less independent of the x-value and decreases with increasing surface temperature complete a consistent picture.

Namely, the adsorption of oxygen on silicon from O_2 proceeds via a molecular precursor state [15], and under certain conditions this process gives rise to an overall sticking probability with a value that is independent of the coverage of the adsorbate [20] and to a decreasing sticking probability with increasing temperature.

It is clear from the above analysis that important parameters in the relative contributions of the gaseous and sputtered oxygen containing species to the oxygen incorporation are the emission angular distribution of sputtering on the cathode and the distance from the sputter surface towards the growth surface. These two parameters, in combination with the total pressure, determine the ratio between the areas on the cathode where the sputtering takes place and the projected area where deposition occurs. At lower pressures, where deposition through ballistic particles prevails, the relative contribution of SiO is expected to decrease with increasing distance, because the ratio of the areas increases. At higher pressures, in the diffusive deposition regime, the ratio of the areas is expected to be large already at relatively small distances and therefore the SiO contribution is expected to be small in this condition.

5.9 The cathode

In figure 5.9 it is seen that the silicon deposition rate and the Si^+ ion flux are independent of the O_2 partial pressure for the entire range necessary to grow SiO_x for $0 \leq x \leq 2$. This implies that, in this range, the sputter rate is independent of the oxygen partial pressure. With a constant ion density [9] and cathode potential [9] (see also figure 5.9) and hence a constant ion current density on the cathode [21], the number of sputtered silicon atoms per incoming ion (*i.e.* Si sputter yield) is deduced to be independent of the oxygen partial pressure in the considered range.

In a simple model, in which the effective oxygen removal rate from the cathode is taken to be proportional to the oxygen coverage and the oxygen incorporation rate independent of the coverage as on the growth surface, we can write the relative oxygen coverage in the racetrack region on the cathode θ_O in the steady-state as:

$$\frac{dN_O}{dt} = 2\alpha_{eff}\Phi_{O_2} - J_{Ar}Y_{SiO}\theta_O - J_{Ar}Y_O\theta_O = 0 \qquad (5.5)$$

$$\theta_O = \frac{2\alpha\Phi_{O_2}}{J_{Ar}Y_{SiO}} >> \frac{r_O}{10r_{Si}} << 1 \ , \ x \leq \sim 1.8 \qquad (5.6)$$

No is the number of oxygen atoms on the surface of the cathode, J_{Ar} is the argon ion current density at the cathode surface and Y is the sputter yield for the different indicated species.
In equation 5.6 we have neglected the removal of oxygen via the atomic oxygen sputtering. The second part of equation 5.6 gives expression to the assumptions that the oxygen incorporation on the growth surface and on the cathode proceeds in the same manner with the same effective reaction probability, and thus both surfaces have a similar temperature. We have also taken into account that the deposition area, as is present in our particular setup, is

about 10 times the sputter erosion area. With these assumptions we can already conclude that the oxygen coverage on the cathode is low for a wide range of x-values.

In the literature some information can be found regarding the sputter rates for varying oxygen concentration on a silicon surface under argon ion bombardment. This work generally relates to Secondary Ion Mass Spectrometry (SIMS) where it is common to apply O_2 flooding during analysis, to enhance the ion yields [22]. However, translating this information to our conditions is not so straightforward, since in SIMS the bombardment energy is usually in the region above 5 keV and therefore much higher than during plasma sputter deposition. Furthermore, one of the relevant parameters in SIMS is the (silicon) sputter yield, which denotes the total number of (silicon) atoms removed per incoming ion [23], irrespective of the species in which it leaves the surface. In case of an elemental silicon target, the number of silicon atoms produced in the sputtering and the number of silicon atoms removed is equal, neglecting the clusters produced in the sputtering.
When bombarding a silicon surface with 5-10 keV Ar^+ ions in the presence of a varying pressure of O_2, the silicon sputter yield has been observed to decrease significantly when the oxygen to silicon concentration ratio in the surface region becomes larger than ~0.8 [24] or ~0.1-0.3 [22]. The important observation is that for lower oxygen to silicon surface concentration ratios the silicon sputter yield appears to be independent of the oxygen concentration. Again, it must be emphasised that this conclusion has been drawn based on results for higher energy primary ions compared to the experimental conditions during sputter deposition. However, the result could make it plausible that, also in our case for lower values of the oxygen coverage on the cathode erosion area, the sputter yield is independent of the oxygen surface concentration.

Next it is argued that in the considered range of oxygen partial pressures the amount of silicon sputtered as SiO molecules is low compared to that sputtered as Si atoms, so that variations in the SiO yield do not become noticeable in the Si growth rate. Consider the situation in Fig. 5.9 where we effectively deposit: x = 1. On the growing film the silicon deposition rate is in this situation equal to the oxygen deposition rate. If the oxygen adsorption proceeds in the same manner on both the growth surface and the cathode, the oxygen deposition rate on the cathode is for x=1 equal to the silicon deposition rate on the growth surface. The measured silicon deposition rate on the growth surface is a result of sputtering of silicon and distribution of the sputter atoms over a factor A/a larger surface area. In this way we can infer that for x = 1 the amount of silicon atoms produced in the sputtering in our deposition system is about a factor of 10 larger than the amount of SiO molecules sputtered. In general, this expressed as detailed equations, in steady-state means:

$$x = \frac{r_O}{r_{Si}} = \frac{2\alpha\Phi_{O_2}}{0.1\Phi_{Si}} = \frac{JY_{SiO}\theta_O}{0.1JY_{Si}} = \frac{Y_{SiO}\theta_O}{0.1Y_{Si}} = \frac{\Phi_{SiO}}{0.1\Phi_{Si}} \qquad (5.7)$$

or

$$\frac{\Phi_{SiO}}{\Phi_{Si}} = \frac{Y_{SiO}\theta_O}{Y_{Si}} = 0.1x \qquad (5.8)$$

From equation 5.8 it is deduced that even for the oxygen partial pressure where films with x-values close to 2 are grown, the amount of SiO sputtering is close to 20 % of the amount of Si sputtering.
From the analysis above it follows that the ionisation probability for SiO molecules on their way through the plasma towards the mass spectrometer entrance appears more or less equal to that of Si atoms under the conditions considered in figure 5.9, since for the situation of film deposition with x = 1, described above the ratio of the ion yields of SiO^+ and Si^+ is in the range of the 0.1. To the best of our knowledge the values for the electron impact ionisation cross-section or for other mechanisms of ionisation of SiO have not been reported in the literature. Factors which may influence the ionisation probability are the (possibly resonant) channels for Penning ionisation by meta-stable argon, the ionisation potential (SiO:11.45 eV, Si:8.15 eV), the residence time in the plasma which is longer for SiO because of its lower speed as compared to Si at the same energy; the energy distribution of sputtered species, where it can be assumed that SiO has a lower average energy than Si. Also a sticking probability for SiO lower than 1 results in a longer residence time of the SiO particles in the plasma which subsequently can give rise to an increased ionization fraction of the particles of this species. Many of these factors would cause a larger ionisation probability for SiO, but these effects have a much smaller influence at the electron temperature in our system than the more than 3 eV difference in ionisation potential. This suggests that the mechanism of ionisation of one or both of the species considered is not solely electron impact ionisation.

5.10 Transition region in the cathode composition

We now understand how, for a wide range of x-values, the silicon deposition rate and oxygen reaction probability are independent of the O_2 partial pressure. However, at a certain oxygen partial pressure a transition region sets in, which leads to a decrease in growth rate and the cathode potential (see Fig. 5.7). The system enters the so-called dielectric mode of deposition [25], associated with the so-called poisoning of the cathode erosion area, and which is accompanied by a less efficient coupling of the RF power into the plasma [9].
Let us first consider qualitatively what could happen on the cathode. At low oxygen partial pressure the oxygen coverage on the cathode silicon surface is so low that it does not affect the rate of production of atomic silicon in the sputtering process, but this coverage increases with increasing oxygen partial pressure, see equation 5.6. In this region the silicon deposition rate is constant. At a certain oxygen coverage the rate of production of atomic silicon as well as the total sputtering rate starts to decrease, which on its turn, results in a steeper increase of the oxygen coverage with increasing oxygen partial pressure. The consequence thereof is that the sputtering rate decreases further, with a further increase of oxygen incorporation on the cathode surface etc. Effectively the cathode becomes fully covered by oxygen and is called poisoned. In experiments in which the flow of oxygen is regulated instead of the oxygen partial pressure, this instability is likely to be more serious in this region, since the decrease of the gettering of oxygen by the (decreasing amount of) deposited silicon results in a higher partial pressure at the same input flow [7].
From our analysis above, we conclude that the transition sets in at a relatively low oxygen-to-silicon concentration ratio at the surface. In fact, the transition occurs at an oxygen partial pressure at which in our system layers with x=2 start to be grown. From equation 5.6 it then follows that $\theta_o \approx 0.2$, which is consistent with the results of Franzreb et al [22].

The transition region is further characterised by a strong decrease of the measured Si^+ flux and a high observed value for the SiO^+ flux, also visible in Fig. 5.7.

5.11 Conclusions

From measurements of the growth rates of oxygen and silicon in RF reactive magnetron sputter deposition of SiO_x films from a O_2/Ar plasma and from measurements of the ions impinging on the growth surface for various deposition conditions, we have deduced and discussed the following conclusions:
-The silicon deposition rate increases strongly with input power. However, the oxygen deposition rate is independent of the power injected in the plasma.
-In our system the silicon deposition rate appears independent of the oxygen partial pressure, and therefore on the x-value, up to $x = 2$. In chapter 4 it has already been deduced that the silicon growth rate does not depend on the total Ar pressure for the pressure values smaller than 0.7 Pa.
-The decomposition probability of molecular oxygen on the growth surface amounts to 0.14 and is independent of the x-value up to $x \approx 1.8$ and independent of the RF input power. This probability decreases with increasing substrate temperature.
-For the substrate at room temperature the contribution of atomic oxygen to the oxygen incorporation amounts to about 16%, independent of the input power and total pressure. The contribution of SiO, sputtered from the cathode, to the total oxygen incorporation is in our system smaller than about 10%. The latter contribution is discussed to depend on the geometrical details of the deposition system and on sputter conditions.
-From a simple model it is deduced that the oxygen coverage on the cathode erosion area is well below one monolayer when the effects of poisoning of the cathode become noticeable in the silicon deposition rate, cathode voltage and other plasma quantities.

5.12 References

[1] E. D. van Hattum, W. M. Arnoldbik, A. Palmero and F.H.P.M. Habraken, Thin Solid Films **494** (2006), 13.

[2] J.R. Chelikowsky, D.J. Chadi and N. Binggeli, Phys. Rev. B. **62** (2000), R2251.

[3] W.D. Sproul, D.J. Christie, D.C. Carter, Thin Solid Films **491** (2005), 1.

[4] A. Palmero, E.D. van Hattum, W.M. Arnoldbik, A.M. Vredenberg and F.H.P.M. Habraken, Journal of Applied Physics **95** (2004), 7611. Chapter 4 of this thesis.

[5] D. Marton, Applied Surface Science **5** (1980), 65.

[6] M.P. D' Evelyn, M.M. Nelson and T. Engel, Surface Science **186** (1987), 75.

[7] S. Berg, H-O Blom, T. Larsson and C. Nender, Journal of Vacuum Science and Technology A 5 (1987) 202.

[8] H. Miyazaki and T. Goto, Journal of Non-Crystalline Solids **352** (2006), 329.

[9] R.Y. Chan, W.S. Ho, J.C. Wolfe and D.L. Licon, Thin Solid Films **287** (1996), 57.

[10] W. L. Fite and R.T. Brackmann, Phys. Rev. **113** (1959), 815.

[11] Y.-K. Kim and J.-P. Desclaux, Phys. Rev. A **66** (2002), 012708.

[12] B.L. Schram, F.J. de Heer, M.J. van der Wiel and J. Kistemaker, Physica **31** (1965), 94.

[13] W.Hwang, Y.K. Kim, and M.E. Rudd, J. Chem.Phys. **104** (1996), 2956.

[14] T. Engel, Surface Science Reports **18** (1993), 91.

[15] A.E. Morgan, H.A.M. de Grefte, N. Warmoltz, H.W. Werner and H.J. Tolle, Applied Surface Science **7** (1981), 372.

[16] F. Meyer and J.J. Vrakking, Surface Science **38** (1973), 275.

[17] J.Z. Xu, W.J. Choyke and J.T. Yates, Journal of Applied Physics **82** (1997), 6289.

[18] A. Terrasi, C. Coluzza, G. Margaritondo, Journal of Applied Physics **78** (1995), 3820.

[19] R. Dorn, H. Lüth and H. Ibach, Surface Science **42** (1974), 583.

[20] D.A. King and M.G. Wells, Proceedings of the Royal Society (London) A **339** (1974), 245.

[21] A. Palmero, E.D. van Hattum, H. Rudolph and F.H.P.M Habraken, Eur. J. of Phys. D accepted for publication.

[22] K. Franzreb, J. Lorincik and P. Williams, Surface Science **573** (2004), 372.

[23] V.S. Smentkowski, Progress in Surface Science **64** (2000), 1.

[24] A.E. Morgan, H.A.M. de Grefte, N. Warmoltz, H.W. Werner and H.J. Tolle, Applied Surface Science **7** (1981), 372.

[25] J.A. Thornton and J.E. Greene in: Rointan F. Bunshah, editor, *Handbook of deposition technologies for films and coatings*, second edition, Noyes Publications 1994, ch. 5.

6

Argon incorporation in the deposited films

6.1 Introduction

In the previous chapter the incorporation of oxygen into the depositing silicon matrix has been discussed. Since argon is abundantly present in the deposition vessel and bombards the deposition surface with a kinetic energy which is about equal to the plasma potential, this element is also found in the deposited films [1,2].
Earlier work [2] showed that inert gas atoms can be incorporated into silicon in a quite stable fashion. However, it remains open for discussion what the local binding configuration of the incorporated argon in the thin film structure is.
In this chapter we describe and discus the argon concentrations in the SiO_x film for a range of deposition conditions in our deposition system for films deposited on carbon. The argon concentration is measured with RBS and the relative statistical error from this analysis is below 0.5 %, unless otherwise indicated.

6.2.1 Argon incorporation into silicon films as a function of power.

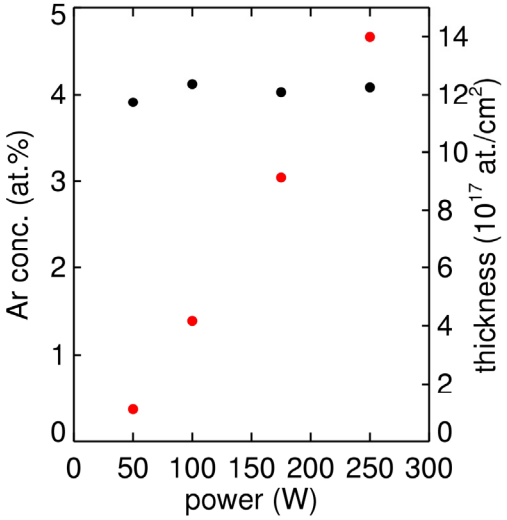

Figure 6.1 Argon-concentration (black) found in deposited silicon films with their thickness (red) after a deposition time of 20 minutes, pressure is 0.66 Pa.

Several pure silicon films (x = 0) were deposited on a carbon substrate as a function of power, each with a total deposition time of 20 min and at 0.66 Pa without oxygen present in the plasma. In Fig. 6.1 both the total thickness and argon concentration are shown. It is seen that the argon concentration in the film amounts to 4 at.% and that the concentration is independent of the injected power and of the thickness.

6.2.2 Argon incorporation as a function of the x-value.

The amount of argon which can be contained in the film does dependent on the x-value of the film. In Fig. 6.2 the atomic percentage of argon as a function of the final x-value is shown. All deposited films have a total thickness of 50 nm. A maximum in the Ar concentration is found at an x-value of 0.5.

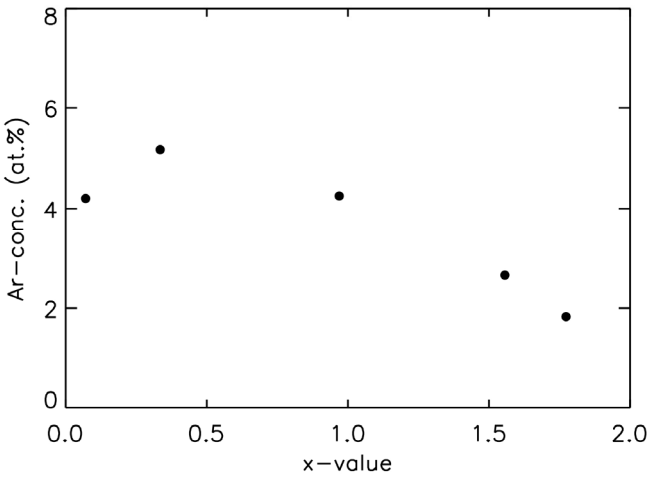

Figure 6.2 Argon-concentration as function of the x-value of the deposited films. Total pressure is kept constant at 0.66 Pa and injected power is 100 W.

6.2.3 Argon incorporation as a function height of the cathode.

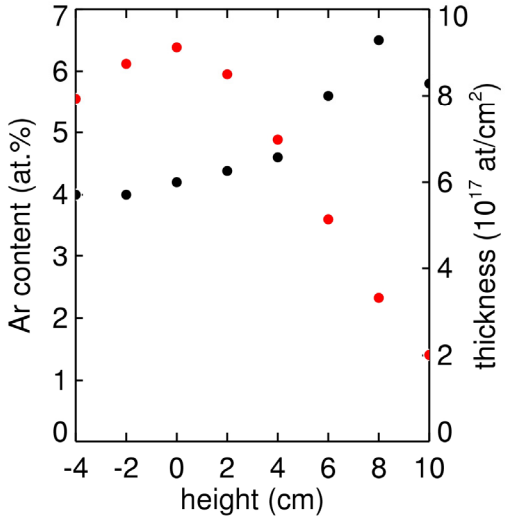

Figure 6.3 Argon content (black) of silicon films (x = 0) and their thickness (red) deposited with the sputter cathode at different heights. At 0 cm, the deposition surface and the centre of the sputter cathode are at the same height. The total pressure is 0.66 Pa and the power is 175 W, deposition time is 20 minutes.

Pure silicon films have been deposited while varying the height of the sputter cathode. The argon concentration and the thickness in these samples are depicted in Fig. 6.3. We find that the argon content does not to vary significantly when the cathode height is varied within 4 cm of the central position, but for larger heights we note an increase in the argon concentration. At the same time we note a strong decrease of the deposition rate with increasing target height as seen from the measured total layer thickness after the deposition. The ion flux towards the deposition surface, as measured with the mass spectrometer,

decreases faster than the silicon deposition rate as a function of height. Therefore, the ratio between ion flux and deposition rate is minimal at minimal height.

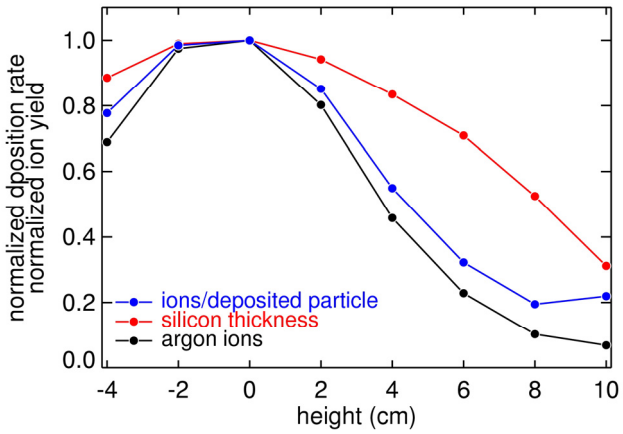

Figure 6.4 Normalized silicon deposition rate, argon ion bombardment and the ratio between these for the samples of Fig. 6.3.

Also, samples containing oxygen have been deposited and measured as a function of cathode height. The main result is the observed variation of the x-value for larger heights, Fig. 6.5. The deposited x-value when the deposition surface is facing the race track, i.e., at zero height, amounts to 0.6. Whereas the oxygen deposition rate remains constant as a function of position, within a certain range, see also chapter 5, the silicon deposition rate diminishes due to the more peaked angular distribution of the sputtered silicon. As a consequence, the resulting x-value of the deposited film increases once the distance to the target increases above a certain value. Here, also the total film thickness diminishes. The oxygen deposition rate only starts to decrease once the x-value of the films exceeds 1.5. For these high x-value films we also notice that the argon content of the film decreases.

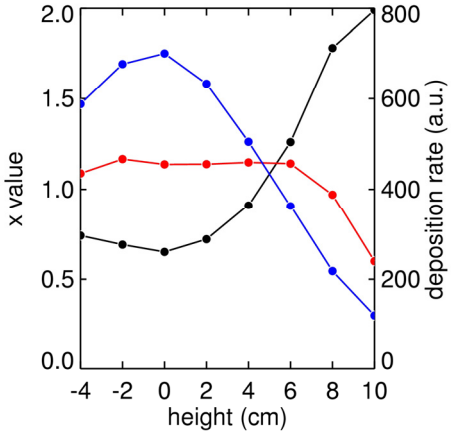

Figure 6.5 Oxygen (red) and silicon (blue) deposition rate and the x-value (black) for films deposited at various locations with respect to the position of the plasma. (total pressure 0.66 Pa, oxygen partial pressure $1.2 \cdot 10^{-3}$ Pa, 175 W)

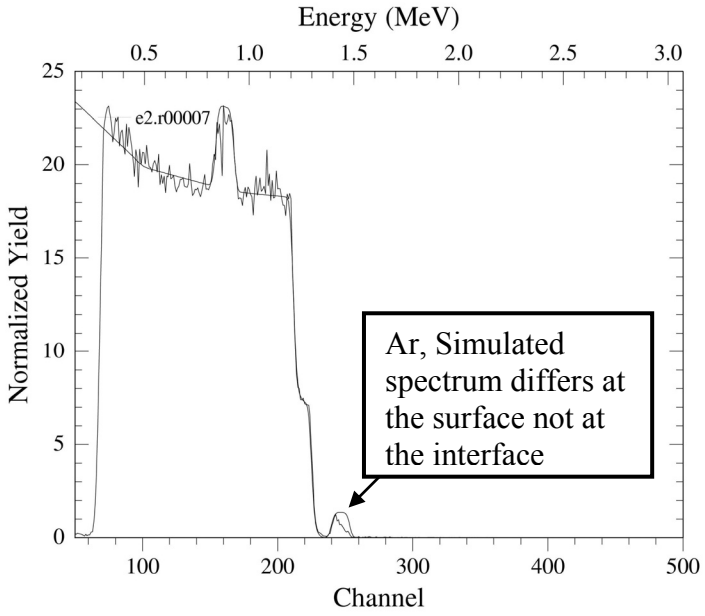

Figure 6.6 A simulated rump spectrum containing a constant amount of argon throughout the film compared to a real spectrum for a film with x-value near 2, deposited on a silicon substrate.

As can be seen in Fig. 6.4 we find by varying the cathode height, a variation of the resulting x-value as in the series alike a variation found when we varied the oxygen partial pressure, Fig.6.2. Strikingly, at high x-values (larger that 1.5), the argon is not present in a constant concentration throughout the film. A non-homogenous concentration profile of argon is found. An example of such a profile is depicted in Fig. 6.6. It is seen that the argon concentration is low at the film surface and increases towards the interface with the substrate. Such a non-uniform depth profile is observed in samples with x-values larger than 1.5.

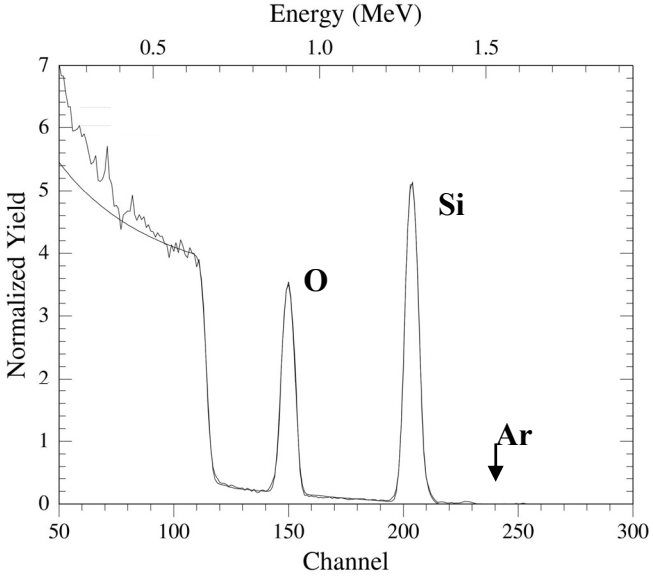

Figure 6.7 A RBS spectrum of deposited SiO_2 film on carbon. No argon is observed in the deposited film. Deposition details are given in the text.

It is shown, in Fig. 6.7, that a film with measured x-value of 2.006 ± 0.0013 does not contain any argon at all. This nearly perfect pure deposition of silicon and oxygen for x = 2 is remarkable in itself. The sample is deposited at 175 W, oxygen partial pressure of 1.2·10-3 Pa, total pressure of 0.66 Pa with the plasma at 10 cm height (see also Fig. 6.7).

6.2.4 An overview of the argon incorporation into the deposited films.

When the film is deposited for given constant experimental conditions (partial pressures and power), but varying substrate temperature, the resulting x-value of the deposited films also varies. The x-value decreases with increasing temperature (chapter 5). Also, the argon concentration decreases at increasing substrate temperature during deposition. As previously shown in chapter 5 in these experiments the temperature ranged between room temperature and 350 °C. The argon-concentration of the heated samples is given in figure 6.8, as a separate series. It is concluded that there is not only an influence of the temperature, but also an influence of the changing x-value.

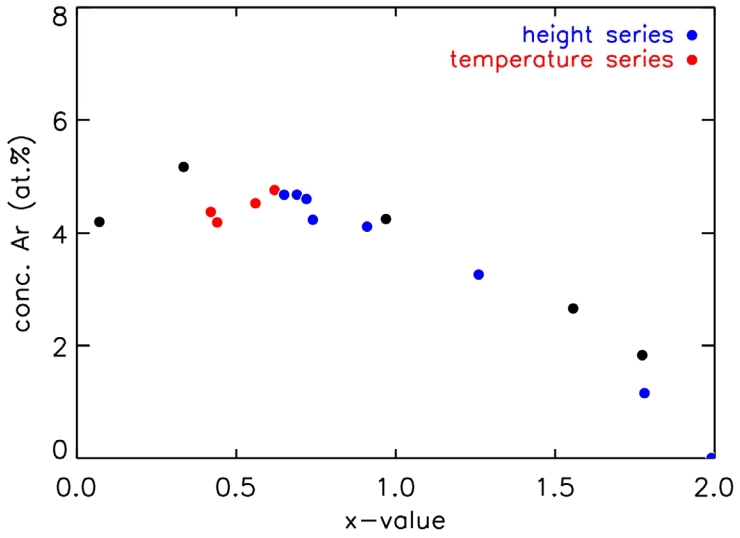

Figure 6.8 Comparison between the argon content as a function of x-value (black) for films deposited on substrates with elevated temperatures (red, from right to left: room temperature, 100, 250 and 350 ºC), and at different substrate heights (blue).

6.3 Discussion

The surface binding energy of argon on silicon amounts to only ~ 0.02 eV [3]. Therefore it can be excluded that the argon incorporation proceeds through adsorption of neutral argon on the growing film and subsequently imbedding, at least at room temperature or higher. The only other possible source of argon in the bulk is implantation of argon ions, ionized in the plasma and accelerated towards the deposition surface. These ions have a kinetic energy equal to the plasma potential, which typically amounts to 30-50 eV,
Indeed, the stability of implanted in silicon appears to be such that desorption takes place at temperatures above 500°C [2]. In line with this literature result, we have found that for

substrate temperatures during growth up to 400 °C, the argon concentration in the growing films is not substantially less.
The projected range of argon ions with the considered kinetic energy is in the range 1-2 nm. With a growth rate of the order of 0.3 nm/s and an ion flux of $10^{16}/cm^2.s$ (see chapter 4), the surface layer of the growing film experiences a total ion fluence of $(3\text{-}7)\cdot10^{16}/cm^2$ before it is buried and has become unreachable for the ions. The measured concentration of argon in silicon amounts to about 4 atomic percent, so the corresponding areal density of argon in the 1-2 nm top layer amounts to $(2\text{-}4)\cdot10^{14}/cm^2$. This crude analysis indicates that the incorporation probability of impinging argon ion is very low, in the order of 0.01. This low value is in agreement with the results of the study of argon implantation in silicon at similar low kinetic energies [2]. This same study indicates that at the argon areal density of the order of $10^{14}/cm^2$ the system is in a quasi-saturation, tentatively ascribed to an equilibrium between implantation and release, both under the influence of the same ion impingement. The release is supposed to be efficient due to the action of collision cascades and defect interactions [2]. This quasi-saturation explains nicely why the incorporated argon concentration is independent of the power or growth rate (Fig. 6.1). Indeed, the argon ion flux on the deposition surface and argon ion energy hardly depends on the RF power injected into the plasma, but on the other hand the growth rate depends strongly on the injected power (Fig. 6.1, see also chapter 4).

The concentration of incorporated argon increases slightly as a function of x up to $x\approx0.4$ and then, for higher x-values, decreases steadily down to 2 at.% for an x-value near 2. The amount of argon ion bombardment (see chapter 4) and the value of the growth rate do not vary substantially with the x-value (see chapter 5), and it is therefore not expected that the small variations in the ion fluence per deposited layer, when changing the x-value, gives rise to a shift in fluence where the quasi-saturation occurs. The difference in argon concentration for different values of x in SiO_x is more likely due to a shift in the equilibrium between implantation and desorption. It is conceivable that the SiO_2-type of network offers fast diffusion paths for argon resulting in a more readily desorption of subsurface implanted argon, resulting in a lower built-in argon concentration. Another explanation is the possible participation of silicon rich regions in the stabilization of the implanted argon, and suggested by recent theoretical work on SiBCN materials: there is simply no possibility for having silicon rich regions for x=2 [4]. Both explanations can explain the observation that for $x > 1.5$ films, the argon concentration declines towards the surface of the film. This can be ascribed to a post-deposition desorption, limited by the diffusion rate of argon inside the material. This implies that the diffusion of argon over relatively long distances is only possible in SiO_2-type of films.
The lower concentration at higher deposition temperature (Fig. 6.8) at the same x-value might also be conceived within the description of equilibrium between implantation and desorption from the surface layer, assuming that the latter occurs to a larger extent at higher temperature. So the measurements seem to indicate that the x-value is the main parameter by which the argon concentration can be varied, and a second order variation can be imposed by varying the deposition temperature.
In this light it is possible to interpret the measurements in which the location of the plasma with respect to the growth surface has been varied. It appeared that when the growth surface approaches the edge of the plasma, the ion flux strongly decreases, accompanied by a less pronounced decrease of the growth rate (Fig. 6.4), resulting in a strong decrease of the

relative ion bombardment during growth (Fig. 6.4). In contrast to this strong decrease, the argon concentration in the films deposited at this height increases, but only slightly. In view of the decreased ion flux per deposited atom this increase seems surprising. However, the increase can be readily understood within the context of the other observations, taking into the account that the lower growth rate at the edge of the plasma is expected to give rise to a larger incorporation of oxygen from the background gas, and taking into account that the temperature of the substrate is expected to be lower at the edge of the plasma.

6.4 Conclusion

Argon is found in deposited RF magnetron sputter deposited SiO_x films in an amount of a few atomic percent. The amount of argon is mainly dependent on the composition of the material which is deposited although also the value of the substrate temperature is of influence. The experimental data are discussed in a model in which the argon incorporation is a result of simultaneous implantation in the subsurface and ion beam induced desorption from the subsurface layers. The drop in the argon implementation degree for higher x-values can be explained either by a larger diffusion length in SiO_2 or the stabilization of the implanted argon by silicon rich regions.

6.5 References

[1] J.J. van Hapert, A.M. Vredenberg, E.E. van Faassen, N. Tomozeiu, W.M. Arnoldbik, and F.H.P.M. Habraken, Phys. Rev. B **69** (2004), 245202.

[2] W.M. Lau, I. Bello, L.J. Huang, X. Feng, M. Vos and I.V. Mitchell, J. Appl. Phys. **74** (1993), 7101.

[3] G.N.A. van Veen, F.H.M. Sanders, J. Dieleman, A. van Veen, D.J. Oostra and A.E. de Vries, Phys. Rev. Lett. **57** (1986), 739.

[4] J. Houska, O. Warschkow, M. M. M. Bilek, D. R. McKenzie, J. Vlcek and S. Potocky, J. Phys.: Condens. Matter **18** (2006), 2337.

Summary

In this thesis we have presented results related to the RF plasma deposition and characterization of thin layers of silicon sub-oxides, SiO_x, under various conditions and for x-values varying between 0 and 2. The present work has been inspired and stimulated by the use of SiO_x in the so-called direct inductive printing (DIP) technology, where the silicon sub-oxide layer is used as the charge retention layer on the drums for copying and printing devices. For this purpose it is important to be able to tune the mechanical, thermal and electronic properties of the final SiO_x layer to have the right combination for a durable product.

The experimental setup is centred around a so-called radio-frequency (RF) magnetron plasma sputter deposition system to grow SiO_x layers. This setup, the instruments and techniques to monitor the layers have been described in Chapter 2. It is demonstrated that our experimental setup allows for adjustment of the externally controllable parameters that ultimately determines the characteristics of the deposited layers. Special attention is being paid to two experimental techniques: Rutherford Backscattering Spectroscopy (RBS) and Elastic Recoil Spectroscopy (ERD). These techniques allow for a detailed quantitative analysis of the grown layers, and can in the case of ERD even be used as an *in-situ real-time* technique while the layers are being grown.

In Chapter 3 the *in-situ* ERD technique is described in more detail and we show how the details of the applied ions and the surface composition are critical for the correct interpretation of the ERD *real-time* measurements. It appears that most of the artefacts of the *real-time* measurements are understood and can be accounted for. The *real-time* measurements are exemplified by results which show that using the O_2 flow to characterise the density of the oxygen in the system gives wrong results concerning the rate of oxygen incorporation. The oxygen partial pressure must be monitored despite the associated experimental difficulties.

Chapter 4 describes a nearly complete characterization of the plasma, i.e., a spatially resolved determination of the ion density, electron temperature and the quasi-electrostatic potential using a Langmuir probe. In addition we describe the extent of ion bombardment on the growth surface as measured with an energy resolving mass spectrometer located in the plane of the deposition surface. It is found that the plasma potential has a maximum about 2 cm from the cathode erosion area, and that it strongly decreases (more than 200 V typically) towards the floating sputter cathode. The potential decreases slightly in the direction towards the growth surface and the positive ions created in the large volume of the plasma closest to the deposition surface will to be accelerated in the direction of the growth surface. These ions which gain a few eV of kinetic energy in the plasma and around 30-40 eV in the so-called anode sheath, are also the ions observed by the mass spectrometer. The majority of ions in the plasma are argon ions, and the flux of ions hitting the growth surface is rather independent of the injected power. This means, that increasing the injected power does not strongly increase the ion bombardment of the deposition surface. On the contrary, since the growth rate is strongly increasing with increasing injected power, the ion bombardment per deposited atom, which is typically about 10-20 ions per deposited atom, decreases strongly.

This is one of the most important conclusions of the present work. It is also found, that the hypothesis that the microstructure of the grown material depends on the ion bombardment is not supported by the experimental data, as deduced from infra-red absorption transmission spectroscopy analysis.

The measurements and discussion of the oxygen incorporation experiments during the deposition are described in chapter 5. The incorporated oxygen originates for ~80 % from molecular oxygen and about 16 % from atomic oxygen produced in the plasma. A minority contribution in our deposition system is from SiO sputtered from the cathode erosion area. From a detailed analysis it is concluded that the oxygen coverage in the erosion area on the cathode is low for all oxygen partial pressures leading to x-values less than two. This explains the observed independency of the silicon growth rate on the deposition surface on the oxygen partial pressure in the range where $x < 2$ is grown. It is discussed how this observation relates to the specific details of the RF plasma deposition setup, and in particular the influence of the magnitude of the racetrack in relation to the dimensions of the setup.

Throughout our work we have found that the grown layers, for x-values less than 2, contain between 2 and 5 atomic percent argon and that the concentration is constant over the full depth of the grown layers. This is reported and discussed in chapter 6: the amount of argon in the film is due to an equilibrium between desorption and implantation in a quasi-saturation regime, which makes this concentration independent of the growth rate. Intriguing, however, is the non-uniform distribution of argon in layers grown under condition leading to SiO_2.

The present work has contributed to the understanding and controllability of the important parameters in the deposition process of SiO_x

Samenvatting

Met SiO_x bedoelen we in dit proefschrift een klasse van materialen, waarvan de grenzen worden gegeven door x=0, puur silicium, en x= 2, silicium dioxide. Met een variatie in de waarde van x van 0 naar 2 varieert het materiaal van een halfgeleider naar een isolator. Dit materiaal is onder andere interessant omdat de elektrische weerstand van het materiaal over een groot gebied kan worden ingesteld door een bepaalde waarde van x te kiezen. Wanneer dit materiaal niet bij hoge temperatuur (boven ~ 650 ºC) verhit is geweest, is het amorf en heeft dus een wanordelijke structuur. Een interessant aspect van dit materiaal is dat bij verhitting, of bij andere manieren van toevoer van energie aan de atomen van het materiaal, er een fasescheiding optreedt. Als deze volledig is, bestaat het materiaal alleen nog uit gebiedjes van silicium en gebiedjes van SiO_2, waarbij de gemiddelde x-waarde voor het materiaal gelijk blijft. Als deze fasescheiding bij voldoende hoge temperatuur gebeurt, dan komt het silicium in een geordende toestand. Op deze manier verkrijgen wij een materiaal dat bestaat uit silicium (nano)kristallen in een SiO_2 matrix. Dit materiaal heeft erg interessante eigenschappen voor (opto) elektronische toepassingen.
Het onderzoek, beschreven in dit proefschrift, is gestimuleerd en gemotiveerd door de toepassing van dunne lagen van dit materiaal op de drums in de geavanceerde kleurenkopieermachine van het Nederlandse bedrijf Océ B.V. Daarbij worden een aantal eisen aan de dunne lagen gesteld, o.a. dat deze bij lage temperatuur op de kopieerdrum worden gedeponeerd. Een goede methode daarvoor is reactieve radio frequente magnetron plasma sputterdepositie. Het doel van het onderzoek beschreven in dit proefschrift is om deze methode van deponeren van SiO_x zoveel mogelijk te begrijpen en daarmee een zo groot mogelijke beheersing van het proces te bereiken. In dit proces van deponeren van materiaal wordt door middel van een radio frequent veld met een bepaald vermogen een ontlading (het plasma) gegenereerd in een lage druk argon gas. De elektronen in de ontlading kunnen het snelle wisselveld volgen en sommige daarvan worden ingevangen door de oppervlakken die in het vacuümsysteem aanwezig zijn. Een van die oppervlakken is een siliciumplaat, die niet geaard is, en die fungeert als kathode. Deze siliciumplaat wordt dus door de elektronen negatief opgeladen. De andere oppervlakken in het systeem zijn geaard. De positieve argonionen in de ontlading zijn veel zwaarder dan de elektronen en kunnen het elektrische wisselveld niet volgen. Zij vormen een positieve ruimtelading. Er ontstaat dus een spanningsverschil tussen de ontlading zelf en de kathode. Het gevolg is dat de positieve ionen worden versneld in de richting van de kathode. Zij bombarderen het silicium oppervlak waarbij silicium atomen vrijkomen (kathodeverstuiving of, zoals men tegenwoordig zegt, sputteren). Deze siliciumatomen bewegen door de ontlading, en slaan neer op een tegenover de kathode geplaatst substraat. Op dit substraat blijven de siliciumatomen plakken, en er groeit dus een laag. Door nu kleine hoeveelheden zuurstof aan het gas toe te voegen, kan zuurstof aan de groeiende laag worden toegevoegd. De zuurstof reageert immers met silicium op het oppervlak van de groeiende laag. En door de partiële druk van zuurstof in het gas te variëren kan de waarde van x worden gevarieerd. Hieruit volgt dat de waarde van x wordt bepaald door de verhouding van de aangroeisnelheden van zuurstof en van silicium. Dus, om de totstandkoming van een bepaalde x-waarde te begrijpen, dienen de aangroeisnelheden van silicium en zuurstof te worden begrepen en tevens hoe deze afhangen van een aantal experimentele parameters zoals druk en het vermogen in het plasma, de zuurstof partiële druk, de temperatuur van het substraat e.d.

Voor het onderzoek was het nodig om veel aan het systeem te meten: het aantal atomen silicium en zuurstof op het substraat, de plasma-eigenschappen zoals de ionendichtheid, de elektrische potentiaal in het plasma als functie van de plaats, en de energie van de elektronen in het plasma, ofwel de elektronentemperatuur. Aangezien het substraat geaard is maar het plasma positief wordt het substraat ook gebombardeerd door argonionen uit het plasma, maar de energie daarvan is kleiner dan de energie van de ionen die op de kathode vallen. Dit argon-ionenbombardement op het substraat kan van invloed zijn op de groeisnelheden van silicium en zuurstof en op de nanostructuur van het gegroeide materiaal: zij kunnen het oppervlak tijdens het groeien opwarmen. Tevens worden deze ionen blijvend in het materiaal geschoten: er blijft argon in de laag achter. In de hoofdstukken 2 en 3 van dit proefschrift wordt beschreven hoe met een aantal technieken deze parameters kunnen worden bepaald. Hierbij wordt gebruikgemaakt van de hoog-energetische ionen uit twee beschikbare van de Graaff versnellers. Daartoe was de groeiopstelling direct gekoppeld aan een van de bundellijnen van een tandemversneller, zodat het mogelijk was tijdens het groeien de hoeveelheid silicium en zuurstof op het substraat te bepalen. Verder werd gebruikgemaakt van een Langmuir probe voor de bepaling van de genoemde parameters in het plasma, en een energie-oplossende massaspectrometer, waarmee bepaald kon worden welke soorten ionen, uit het plasma, en hoeveel ionen van elke soort op het groeioppervlak vallen en met welke energie ze dat doen. Dat waren natuurlijk vooral argonionen, maar ook zuurstofionen en geïoniseerde zuurstofmoleculen, en verder siliciumionen die van de kathode vandaan komen. Daarbij moeten we wel in de gaten houden dat maar een zeer klein deel van alle aanwezige deeltjes in het plasma positief geladen is. Het overgrote deel daarvan is neutraal en reageert dus niet op de elektrische velden.
De afstand tussen de kathode en ons groeioppervlak bedraagt 8,5 cm. Het blijkt dat wij het plasma grofweg in twee gebieden kunnen onderverdelen: op een afstand van 2 cm van het kathode oppervlak is de elektrische potentiaal in het plasma het hoogst. Alle ionen die in het radiofrequente veld worden gegenereerd in het gebied tussen dit maximum en de kathode worden versneld in de richting van de kathode en dragen bij aan het sputteren van de siliciumatomen. In de rest van het plasma wijst het elektrische veld in de richting van de geaarde oppervlakken, dus in een bepaald gebied ook naar het groeioppervlak. Alle ionen die daar worden gevormd, worden versneld naar het groeioppervlak. Het blijkt dat de grootte van de argon-ionenstroom op het groeioppervlak en de energie van deze ionen niet erg afhangen van het vermogen in het plasma. Daarentegen nemen de ionenstroom en ionenenergie op de silicium-kathode wel toe met het toenemend vermogen in het plasma, zodat de hoeveelheid vrijgemaakte siliciumatomen, en dus de groeisnelheid op het substraat, sterk toeneemt met het vermogen in het plasma. Hieruit volgt dat op het substraat de mate van ionenbombardement per gedeponeerd siliciumatoom afneemt naarmate het vermogen groter wordt. Dit is het omgekeerde van wat men intuïtief zou verwachten, en is een van de belangrijke conclusies uit dit onderzoek. Het blijkt echter ook dat een variatie van het ionenbombardement niet resulteert in een significante variatie van de nanostructuur van de gegroeide laag. Dit alles staat beschreven in hoofdstuk 4.

In hoofdstuk 4 staat ook beschreven, dat de ionenstroom en de siliciumgroeisnelheid nauwelijks van de argon totaaldruk afhangen, behalve dan bij de hogere drukken waarbij de versnelde ionen en de versputterde silicium atomen een grotere kans hebben om te botsen met argonatomen in het gas, en daarmee hun energie en hun richting verliezen. Bij de hogere drukken nemen beide grootheden dan ook af.

Hoofdstuk 5 handelt vooral over de zuurstof inbouw in de gedeponeerde laag. Dit kan bijna worden beschreven als een onafhankelijk proces, waarbij ieder zuurstofmolecuul bij botsing met het groeioppervlak een kans van 14% blijkt te hebben om te reageren met een van de siliciumatomen op het oppervlak. Deze inbouwkans blijkt onafhankelijk te zijn van de x-waarde, hetgeen een opmerkelijke resultaat is. Botsingen van zuurstofmoleculen met het oppervlak zijn verantwoordelijk voor ongeveer driekwart van alle ingebouwde zuurstof. Verder blijkt ongeveer 16 % van alle ingebouwde zuurstof afkomstig te zijn van zuurstofatomen, die ontstaan zijn door dissociatie van moleculaire zuurstof in het plasma. Uit het onderzoek blijkt dat de bijdrage van atomaire zuurstof groter is als het substraat tijdens het groeien verhit wordt.
Zuurstof uit het gas en atomaire zuurstofatomen uit het plasma reageren natuurlijk ook met het kathode–oppervlak, waar het vervolgens ook weer vanaf wordt gesputterd. Dit blijkt te gebeuren in de vorm van SiO moleculen. In hoofdstuk 5 wordt uitgelegd hoe het komt dat deze SiO moleculen nauwelijks bijdragen aan de groeisnelheid van silicium en zuurstof. Er komt naar voren dat voor een goede beheersing van de zuurstofgroeisnelheid, en dus van de x-waarde, het noodzakelijk is om de zuurstof partiële druk en de temperatuur van het substraat nauwkeurig te beheersen.
Ten slotte beschrijft hoofdstuk 6 metingen van de hoeveelheid ingebouwde argon voor de verschillende depositieparameters. De argonconcentratie in de gegroeide laag varieert tussen 0 en ongeveer 6 at. %. Het blijkt in eerste orde dat de argon-inbouw voornamelijk afhangt van de x-waarde, en in tweede orde ook van de temperatuur van het substraat tijdens het groeien. Er is een model opgesteld waarin naar voren komt dat de resulterende argonconcentratie het gevolg is van implantatie en daaropvolgend incompleet verdampen van geïmplanteerd argon.

List of publications

A.Palmero, E.D. van Hattum, H.Rudolph and F.H.P.M. Habraken, *Characterization of a low-pressure argon plasma using optical emission spectroscopy and a global model,* submitted

A.Palmero, E.D.van Hattum, H.Rudolph and F.H.P.M. Habraken, *Characterization of the ion cathode fall region in relation to the growth rate in plasma sputter deposition*
European phys. J. D, accepted for publication

W. M. Arnoldbik, E. D. van Hattum, and F. H. P. M. Habraken, *Analysis of silicon suboxide films using MeV/amu heavy ions*, Izvestiya RAN, Ser. fizich., **70** (2006), 834

E.D. van Hattum, W.M. Arnoldbik, A. Palmero and F.H.P.M. Habraken, *On-line characterisation of radiofrequency magnetron sputter deposition of SiOx using elastic recoil detection*, Thin Solid Films, **494** (2006), 13.

A. Palmero, E.D. van Hattum, H. Rudolph and F.H.P.M. Habraken, *Characterization of an Ar/O2 magnetron sputtering plasma using a Langmuir probe and an energy resolved mass spectrometer*, Thin Solid Films, **494** (2006), 18.

W. M. Arnoldbik, N. Tomozeiu, E. D. van Hattum, R. W. Lof, A. M. Vredenberg, and F. H. P. M. Habraken *High-energy ion-beam-induced phase separation in SiO_x films*
Phys. Rev. B **71** (2005), 125329.

J.-P.R.Wells, E.D. van Hattum, R.E.I. Schropp, P.J. Phillips. D.A. Garder, F.H.P.M. Habraken and J.I. Dijkhuis, *Ultrafast spectroscopy of localised vibrational modes in amorphous silicon using a free electron laser,* Phys.Stat.Sol. (b) **241** (2004), 3474.

H.C. Swart, E.D. van Hattum, W.M. Arnoldbik, and F.H.P.M. Habraken, *Comparison of SiOx structure in RF sputtered samples,* Phys.Stat.Sol. (c) **1** (2004), 2286.

J.P.R. Wells, E.D. van Hattum, P.J. Phillips, D.A. Carder, F.H.P.M. Habraken and J.I. Dijkhuis, *Degenerate four wave mixing spectroscopy of oxygen vibrations in amorphous silicon*, J. Lumin. **108** (2004), 173.

A. Palmero, E.D. van Hattum, W.M. Arnoldbik, A.M. Vredenberg and F.H.P.M. Habraken, *Characterization of the plasma in a RF magnetron sputtering system,* J.Appl.Phys. **95** (2004), 7611.

E.D. van Hattum, A. Palmero, W.M. Arnoldbik and F.H.P.M. Habraken, *Experimental characterization of the deposition of silicon suboxide films in a radiofrequency magnetron reactive sputtering system,* Surf. Coat. Technol. **188** (2004), 399.

A. Palmero, E.D. van Hattum, W.M. Arnoldbik, F.H.P.M. Habraken, *Argon plasma modelling in a RF magnetron sputtering system*, Surf. Coat. Technol. **188** (2004), 392.

Dankwoord

Na een opsomming van alle resultaten is het natuurlijk van belang om al degenen te bedanken die de totstandkoming van dit boekje mede mogelijk hebben gemaakt, al is het een illusie om te denken dat ik niemand vergeet hier te noemen.

Allereerst wil ik mijn promotoren Frans Habraken en Henrik Rudolph bedanken. Frans die vanaf het begin bij het project betrokken is heeft menigmaal een positieve draai weten te geven aan discussies. De mogelijkheden tot in-situ metingen zouden zonder jouw steun wellicht niet zo uitgebreid zijn als nu het geval is. Ook zou dit boekje zonder jouw input volledig anders zijn.
Henrik die pas later bij het project betrokken is geraakt en veel tijd heeft gestoken in, in het bijzonder OES en de ionisatiemechanismen van de deeltjes in het plasma: ook jouw invloed op het boekje is niet te onderschatten.
Wim Arnold Bik wil ik bedanken, niet alleen als co-promotor, maar ook bij het opbouwen van de opstelling. Ondanks de standaard opmerking, “ik heb nu even geen tijd”, is er toch veel tijd gaan zitten in met name, het ERD systeem en de analyse van de meetresultaten. Daarbij komt ook nog de installatie en ingebruikneming van nieuwe (MS, LP), en soms minder nieuwe apparatuur (RGA).
Bij praktische problemen, vrijwel altijd een tekort aan handen, is het altijd Theo Klinkhamer geweest die hielp bij het openmaken van de vacuümopstelling, reparatie van een onderdeel, het ontwerp en installatie van nog weer een extra component etc. De inzet die jij hebt laten zien bij het operationeel houden van de ZEESTER is toch zeker een bedankje waard.
I’d also like to thank Alberto Palmero for the work we did together and for the patience he showed during our discussions about the plasma and the deposited SiO_x films, although we did not always agree on things, the discussions we had led the way to good results.

Aan het begin van mijn aanstelling heb ik samen mogen werken met prof. Hendrik Swart (Universiteit van die Vrystaat, ZA) die enige maanden bij ons op bezoek is geweest. Hoewel de resultaten van de XPS metingen aan verhitte monsters niet terug te vinden zijn in dit boekje, speelde de verhitting van SiO_x lagen aan het eind van mijn onderzoeksperiode toch weer op.

De studenten die bij mijn onderzoek betrokken zijn geweest wil ik bedanken voor de inzet die zij getoond hebben. Joep Jongen, Maaike Ouwerkerk en Mohamed Mahi, jullie bijdragen zijn niet altijd even zichtbare binnen dit boekje maar hebben toch een richting gegeven aan de onderzoekslijn.

Ondersteuning wat betreft de experimentele optische technieken is mede afkomstig van Ruurd Lof, en voor de interpretatie daarvan moet ik juist Ernst van Faassen weer bedanken. Helaas hebben we niet op tijd de resultaten uit de reflectiemetingen op orde kunnen verkrijgen. Ook de versnellertechnici, Henk Kersenmaekers, Gerard van Gelder, Philip van der Vliet, Ruud

Stappershoef en Remko van Hal wil ik bedanken voor het aanleveren van de vele (verschillende) bundels die er voor mij gemaakt zijn.
Zoals ook voor in dit boekje staat is er samengewerkt met een projectgroep vanuit Océ: Jo Geraerds, Rob Koper, Marijn van de Bogaard, Jan de Putter (overleden in 2004), Jan Slaats, Tom Huijgen, Peter Derks, Jacob Valk, Lei Roodbeen, Nicolae Tomozeiu en Marcel Slot wil ik bedanken voor de samenwerking op het gebied van de SiO_x lagen.

Mijn collega-promovendi binnen FM wil ik ook bedanken, Bas Feddes, Elmuez Dawi, Edwin van der Wal, Govert Kruijtzer, Marijn van Veghel, Marites Violanda, Mirela Georgescu en Timon van Wijngaarden. Ondanks dat de overlap tussen de verscheidene onderzoeken niet altijd zichtbaar is, is het toch mogelijk geweest om op verschillende manieren te samenwerken.
Ook Riny de Haas wil ik bedanken, vooral voor de steun tijdens de wat moeilijkere perioden in de schrijftijd. Altijd was er de mogelijkheid om even langs te lopen met een kop koffie en zodoende de gedachten even ergens anders heen te brengen.
Buiten de FM-groep wil ik de medewerkers van de zonnecelgroep bedanken. Zowel de gezamenlijke koffiepauzes als lunchpauzes zullen niet worden vergeten.

Als laatste wil ik mijn ouders bedanken, die van onschatbare waarde zijn geweest, zowel tijdens mijn studie als tijdens deze promotieperiode. Hoewel ik vaak onbegrijpelijke antwoorden gaf, zijn jullie de interesse in mijn onderzoek nooit verloren.

Curriculum vitae

De auteur van dit proefschrift werd geboren op 10 september 1976 te Soest. Na Mavo, MBO-Fotonica en een HBO-natuurkunde propedeuse begon hij met de opleiding tot natuurkundig ingenieur aan de Technische Universiteit van Delft, welke hij in 2002 afsloot met een onderzoek in de vakgroep nano-fysica. Het afstudeeronderzoek draagt de naam: *The resistive properties of a superconducting aluminum microbridge in a magnetic field*. In december 2002 is hij in dienst getreden van de Universiteit Utrecht bij het onderzoeksprogramma Surfaces, Interfaces and Devices. Hier werd het onderzoek verricht dat beschreven is in dit proefschrift. Gedurende de promotietijd begeleidde hij, in het kader van zijn onderwijstaak, werkcolleges in de onderwerpen vaste stof Fysica en Natuurkunde voor NWI studenten, en heeft bij 2 bachelor studenten en een HBO studente begeleid bij hun afstudeeronderzoek.